Computational Stress Analysis Using Finite Volume Methods

Nosrat Allah Fallah

Centre for Numerical Modelling and Process Analysis

School of Computing and Mathematical Sciences

University of Greenwich

London, UK

A thesis submitted in partial fulfilment of the requirements of the University of Greenwich for the Degree of Doctor of Philosophy

November 2000

Dedications

To My Wife, Mahsima

and

My Daughters, Mona and Maryam

Acknowledgements

I would like to express my profound gratitude to my supervisors Dr. Christopher Bailey and Prof. Mark Cross for their guidance, encouragement and constant availability for discussions throughout this research.

I would also like to express my thanks to friends and colleagues at Greenwich particularly to Dr. Gary Taylor and Dr. Nick Croft for their useful advice and discussions.

I would also like to acknowledge the financial support of the University of Greenwich for funding my research.

Finally I wish to acknowledge the affection and support of my family, especially my wife who was patient and supportive throughout this period.

Abstract

There is a growing interest in applying finite volume methods to model solid mechanics problems and multi-physics phenomena. During the last ten years an increasing amount of activity has taken place in this area. Unlike the finite element formulation, which generally involves volume integrals, the finite volume formulation transfers volume integrals to surface integrals using the divergence theorem. This transformation for convection and diffusion terms in the governing equations, ensures conservation at the local element level. This is seen as a major attraction for finite volume methods.

The research presented in this thesis details the development of a cell vertex based finite volume formulation for complex analysis like geometrically nonlinear modelling and plate analysis. For both geometrically nonlinear and plate analysis a series of simulation results are presented and are compared with conventional finite element results.

Further research has been carried out to solve stress problems in multi-physics phenomena using a Computational Fluid Dynamics(CFD) frame-work. This approach has the advantage in that it uses the similarities between fluid and solid momentum equations to introduce some modifications in a CFD code that allows a complete CFD solution procedure to be used for the simultaneous calculation of the velocity, temperature and displacement variables. The results of this integrated approach are compared with results obtained by using techniques which solve the problem by

using two solvers (one for solid regions, one for fluid regions).

In summary, the novelty of the research detailed in this thesis is:

- Finite volume formulation for elastic large strain analysis. Comparison of this approach with traditional finite element techniques:
  - Cell-vertex finite volume method is as accurate as finite element approach but slower in solution time.
- Finite volume formulation for structural plate analysis. Comparison with traditional finite element method:
  - Novel finite volume approach is as accurate as finite element approach.
  - Does not display locking problems (observed with finite element methods) and is comparable in solution times.
- Formulation of an integrated CFD solver for coupled flow, heat transfer and stress calculations. Comparison with a 2-solver approach:
  - Integrated approach is much faster and substantially less memory intensive than 2-solver approach.

Comparisons between the new formulation and traditional approaches are made in terms of accuracy and solution speed.

Contents

List of Figures

List of Tables

Nomenclature

$\mathbf{F}$	Deformation gradient tensor
$\mathbf{E}$	Green-Lagrange strain tensor
$\mathbf{E}^*$	Amansi strain tensor
$\mathbf{C}$	Green deformation tensor
$\mathbf{B}^{-1}$	Cauchy deformation tensor
$\boldsymbol{\sigma}$	Cauchy stress tensor
$\mathbf{T}^o$	First Piola-Kirchhoff stress tensor
$\tilde{\boldsymbol{\sigma}}$	Second Piola-Kirchhoff stress tensor
$\mathbf{b}_o$	Body force per unit initial volume
$\mathbf{b}$	Body force per unit current volume
V_o	Initial volume
V	Current volume
S_o	Initial area
S	Current area
ρ_o	Initial density

ρ	Current density
J	Deformation gradient determinant
$\mathbf{n}$	Unit outward normal
$\mathbf{u}$	Displacement vector
G	Shear Modulus
$\mathbf{D}$	Elasticity coefficient matrix
$\mathbf{B}_o$	Linear strain displacement matrix
$\mathbf{B}$	Nonlinear strain displacement matrix
$\mathbf{G}$	Shape function gradient matrix
$\mathbf{T}$	Outward normal operator
$\mathbf{L}$	Linear differential operator
$\mathbf{K}_t$	Stiffness matrix
t	Plate thickness
k	Lateral shear correction factor
$\mathbf{M}$	Bending moment
$\mathbf{Q}$	Lateral shear force
γ	Lateral shear strain
ν	Poisson's ration
$\mathbf{v}$	Velocity vector
p	Pressure

μ	Dynamic viscosity
T	Temperature
T_r	Reference temperature
α	Thermal expansion coefficient
Γ	Diffusion coefficient
S_C	Constant coefficient of linearised source term
S_P	Linear coefficient of linearised source term

Chapter 1

Introduction

The Finite Difference Method(FDM) was widely used in continuum physics before the advent of computers. Using a finite difference approach, the problems are discretized in conjunction with a Taylor series approximation. The diagonal dominant system of algebraic equations thus formed is solved by suitable numerical solvers. This early technique had limited success for solving Computational Solid Mechanics(CSM) problems compared with other methods such as the Finite Element Method(FEM). The most important reason, was the difficulty of applying these techniques to irregular geometries in a simple manner [1, 2]. The finite element method has firmly established itself as the pioneering approach for the CSM problems. The Finite Element(FE) discretization approach is well suited to unstructured meshes for modelling of problems involving irregular geometries. The FDM received a renewed interest when associated with a control volume. This was a ground breaking step in discretization methods, as the method originally had the appearance of a FDM but employed some of the typical conventions of a FEM. This was the initial step in the creation of a new concept of discretization under the heading of Finite Volume Methods(FVM). The Finite Volume(FV) technique enforces conservation of the governing physics over the designed control volume as described by Patankar [3] and Hirsch [4]. Today, the FVM is the most common discretization technique used within the Computational Fluid Dynamics(CFD) community. The FVM applica-

tion for CSM problems is in its early stage of developments[2, 5, 6, 7, 8] and for many solid mechanics applications it is still under the development as indicated by the research presented in this thesis.

The research undertaken in this project consists of three applications of the FVM for the CSM problems. The following sections describe these applications with particular regard to the above mentioned numerical techniques.

1.1 Geometrically nonlinear(GNL) problems

With the introduction of stronger, light weight and more flexible synthetic materials, geometrically nonlinear analysis of civil, structural and mechanical engineering applications and industrial components has become essential. In small deformation based analysis (geometrically linear analysis), the equilibrium equations are formulated with respect to the undeformed known configuration where the deformed shape and undeformed shape are assumed the same in setting up the governing equilibrium equations. In some practical situations such assumptions fail and the difference between undeformed shape and deformed shape is significant and must be taken into account. In this situation the load deflection characteristics are affected by geometry changes caused by the loading. When deformation is dependent on the unknown deformed geometry, it means the structural response is nonlinear whether or not the material behaviour is linear. In other words, if an applied load, $\mathbf{P}$, causes a displacement response, $\mathbf{u}$, the displacement response corresponding to load $\alpha\mathbf{P}$, where α is a constant, is no longer $\alpha\mathbf{u}$. This type of nonlinearity is called geometrical nonlinearity.

The GNL analysis may be formulated in either a Total Lagrangian or an Eulerian coordinate system, the former is in terms of the initial configuration and the latter is in terms of the final deformed configuration. Computationally, an Eulerian formulation

is strictly an Updated Lagrangian approach [9], where the reference configuration becomes the current equilibrium state prior to some incremental change. The Total Lagrangian approach offers advantages since the initial configuration remains as a constant reference configuration which simplifies formulation and computation.

While the GNL analysis by the finite element method, as mentioned above, started in the 1960's [10, 11], the literature on applications of the finite volume technique to these problems is very limited. Currently Maneeratana *et al.* [12] and Wenke *et al.* [13] have adopted Cell-Centred Finite Volume(CC-FV) approach to analyse these problems. The method discussed here differs from previous reported works as it uses the Cell Vertex based Finite Volume(CV-FV) method as discussed by Fallah *et al.* [14, 15].

1.2 Small deformation of plate

The subject of bending of plates and indeed its extension to shells was one of the first to which the finite element method was applied. At that time various difficulties that were to be encountered were not fully appreciated and for this reason the topic remains one in which research is active to the present day. Plates and shells are a particular form of a three dimensional solid, the treatment of which presents no theoretical difficulties, at least in the case of elasticity. However, the thickness of such structures is very small when compared with the other dimensions and complete three dimensional numerical treatment is expensive. To ease the solution of such problems, even long before numerical approaches became possible, several classical assumptions regarding the behaviour of such structures were introduced as follows:

- The normal stress through the thickness (i.e. perpendicular to the mid-surface) of the plate is zero.
- Material particles that are originally on a straight line perpendicular to the

mid-surface of the plate remain on a straight line during deformation.

In thin plate theory, which is based on assumptions formulated by Kirshhoff in 1850 [16], shear deformations are neglected and the straight line remains perpendicular to the mid-surface during deformation. In the Reissner/Mindlin plate theory [17, 18] shear deformations are included and, therefore the line originally normal to the mid-surface in general does not remain perpendicular to the mid-surface during the deformations.

Figure 1.1 illustrates deformation of a cross section of a plate with or without shear effects. In both theories the direct stresses in the normal direction of mid-plane are small and hence direct strains in that direction can be neglected. In the thin plate theory it is possible to represent the state of deformation by the lateral displacement w of the mid-plane of the plate. To ensure that the plate remains continuous and does not kink at nodes on element interfaces, it will always be necessary to use both the values w and its slopes to impose continuity. The first finite element procedure developed to model thin plates in bending was based on the Kirshhoff plate theory [19]. The difficulties in these approaches are that the elements must satisfy the convergence requirements and be relatively effective in their applications. A great deal of research was spent on the development of such elements [20, 21, 22]; however, it was recognized that more effective elements can frequently be formulated using the Mindlin/Reissner plate theory [23, 24, 25, 26].

The early work of applying finite volume to plate analysis was published by Demirdzic *et al.* [27]. In that work the authors applied 8-noded brick elements for discretization. Work by Wheel [28] is based on the Mindlin/Reissner plate theory, he showed the non locking behaviour of the finite volume formulation for thin plate analysis. The work presented in this thesis differs from that previously undertaken as again it uses the vertex based finite volume method. It also compares this approach with the traditional finite element method.

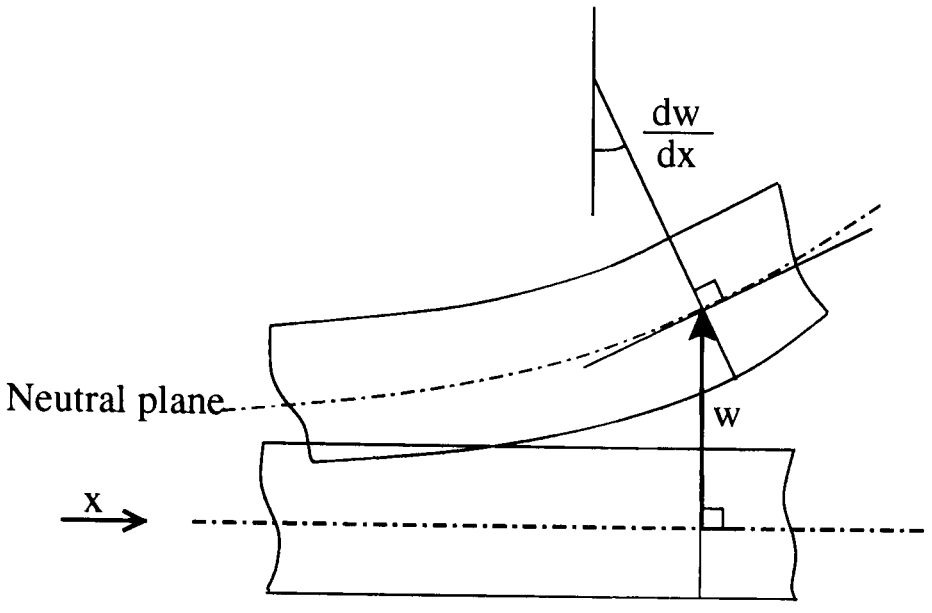

(a) Deformations excluding shear effect (Kirshhoff plate theory)

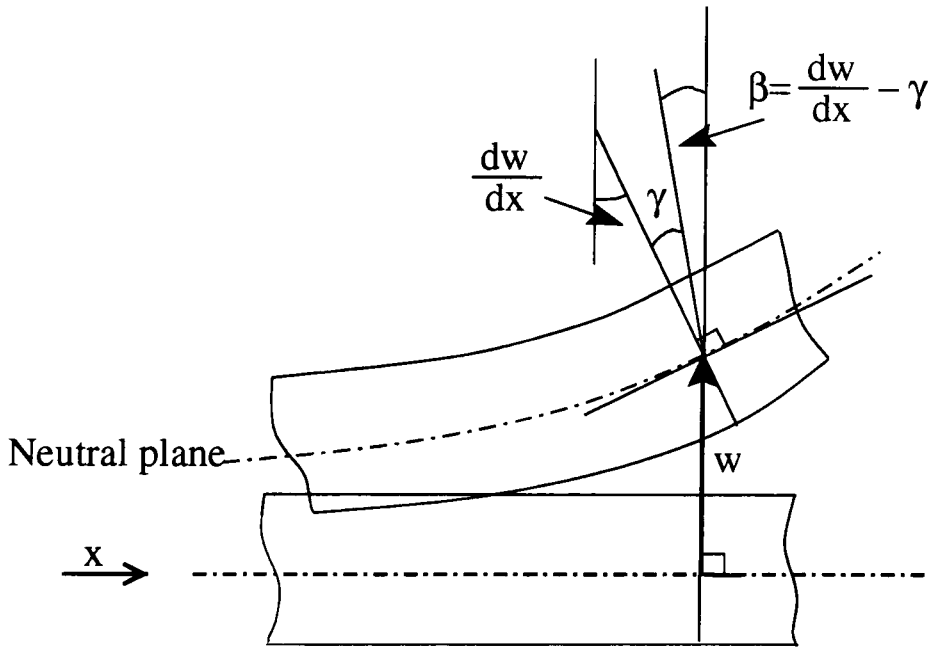

(b) Deformations including shear effect (Mindlin plate theory)

Figure 1.1: Shear effects assumptions.

1.3 Coupled problems

Frequently two or more physical systems interact with each other where the independent solution of any one system cannot be made without the simultaneous solution of the other. Such systems are known as coupled systems. A definition of coupled systems may be generalized to include a wide range of problems and their numerical discretization as [29]:

> "Coupled systems and formulations are those applicable to multiple domains and dependent variables which usually, but not always, describe different physical phenomena and in which:
>
> (a) Neither domain can be solved while separated from the others;
> (b) Neither set of dependent variables can be explicitly eliminated at the differential equation level."

In some problems coupling occurs on domain interfaces via the boundary conditions imposed there. Generally each domain describes different physical situations. Fluid-structure interaction is an example of this type [30]. In other types of problems coupling occurs through the differential governing equations describing different physical phenomena. Metal extrusion can be an example of this type of coupling where the plastic flow is strongly coupled with the temperature field while the same time the latter is influenced by the heat generated in the plastic flow.

The general approach to solving coupled systems, especially those involving both fluids and solids is to use two solvers, one for fluids (based on CFD(FV) methods), the other for solids (based on FE methods). This involves integrating results from two codes which is very time consuming and prone to errors.

Demirdzic *et al.*[31] have developed a cell centred finite volume based formulation for solving coupled problems. In their approach they assembled and solved equations of different part of the model turn by turn by passing information accross interfaces as boundary conditions. Spalding [32] has developed an approach where the solid region in the model can be analysed simultaneously with the fluid part of the model in a single CFD framework. This idea is based on the existence of similarities between the Navier-Stokes equations for flow and the solid momentum equations. While the idea is novel and simple, its implementation depends on the features of the CFD code being used.

The research described in this thesis (chapter 6) has essentially extended this single CFD framework for solving fluid flow, heat transfer and stress using an unstructured mesh solver within the PHYSICA [33] modelling framework. This is different from work previously reported in this area.

1.4 Scope of the thesis

The main aim of this research is to provide novel developments of cell vertex based finite volume modelling technique in solid mechanics analysis. The novelty of this work is:

- Application of finite volume technique to GNL analysis.
- Application of finite volume technique to small deformation of plate analysis .
- Simultaneous analysis of coupled problems in a CFD framework.

A novel finite volume continuum mechanics based approach is developed for the GNL formulation where Total Lagrangian reference frame is adopted. In this method, there is no restriction on magnitude of the deformation quantities. The stress and strain relation is assumed linear and the formulation is applicable for two and three

dimensional modelling. Constant strain triangular elements and bilinear quadrilateral elements are used for the two dimensional analysis and trilinear hexahedral or brick elements is used for three dimensional modelling. Plane strain and plain stress assumptions are both considered in the formulations.

To provide an in-house resource as a need for comparing the results with the finite element predictions a finite element code was also been developed with the same capabilities of finite volume code in solving GNL problems. Some bench-mark test cases are presented which demonstrate the behaviour and the accuracy of two and three dimensional elements for the GNL applications using both FV and FE procedures.

Finite volume based formulation for plate structures is another goal of this work. The plate deformation is assumed small enough, which allows us to apply the small deformation theory of plates. Mindlin/Reissner plate theory is applied in the formulation because, as in the finite element formulation [23], it provides simplicity in element formulation using the cell vertex based finite volume method. Bilinear quadrilateral elements are used in the discretization. As with the GNL analysis, a finite element code has also developed in parallel with the finite volume code. Since the finite element code with quadrilateral elements "locks" in thin plate analysis, a mixed interpolation technique [23] is used in the finite element code for enriching the finite element code capabilities in thin plate analysis situations. The results of some test cases demonstrate the finite volume capabilities in plate analysis. Using a finite volume procedure, the nonlocking behaviour in thin plate analysis is demonstrated. The finite element method displays locking for these examples and requires mixed interpolation technique to overcome this.

The third goal of this research is the analysis of coupled problems using a CFD frame work without making major changes to the structure of the CFD code. The

coupled problem of interest in this thesis is illustrated in Figure 1.2. This type of problem involves stress-flow-thermal effects simultaneously in a multiphysics manner. This type of example is typical of a chip on a printed circuit board where heat is generated in the solid part of the model (chip) because of its performance and the temperature distribution becomes stationary by cooling from the surrounding air flow. The traditional way for solving this type of problem is based on calculating the temperature and air flow distribution over the whole field using a CFD code and thereafter using an appropriate stress solver for calculating stress in the solid part of the model. This method treats the problem in a decoupled manner. In this research we are interested in solving the whole domain simultaneously by using a single CFD solver to predict the velocity field in the fluid region, temperature throughout the whole domain and displacement field in the solid region at the same time. As mentioned before, the idea is based on the similarities between the fluid and solid momentum equations. This idea has been implemented in this thesis. The PHYSICA multiphysics package has been used and some necessary modifications for imposing the solid equations has been made. The simulation results show this technique is very cost effective in terms of memory usage and CPU time, compared to the method where different solvers are used for the fluid and the solid parts.

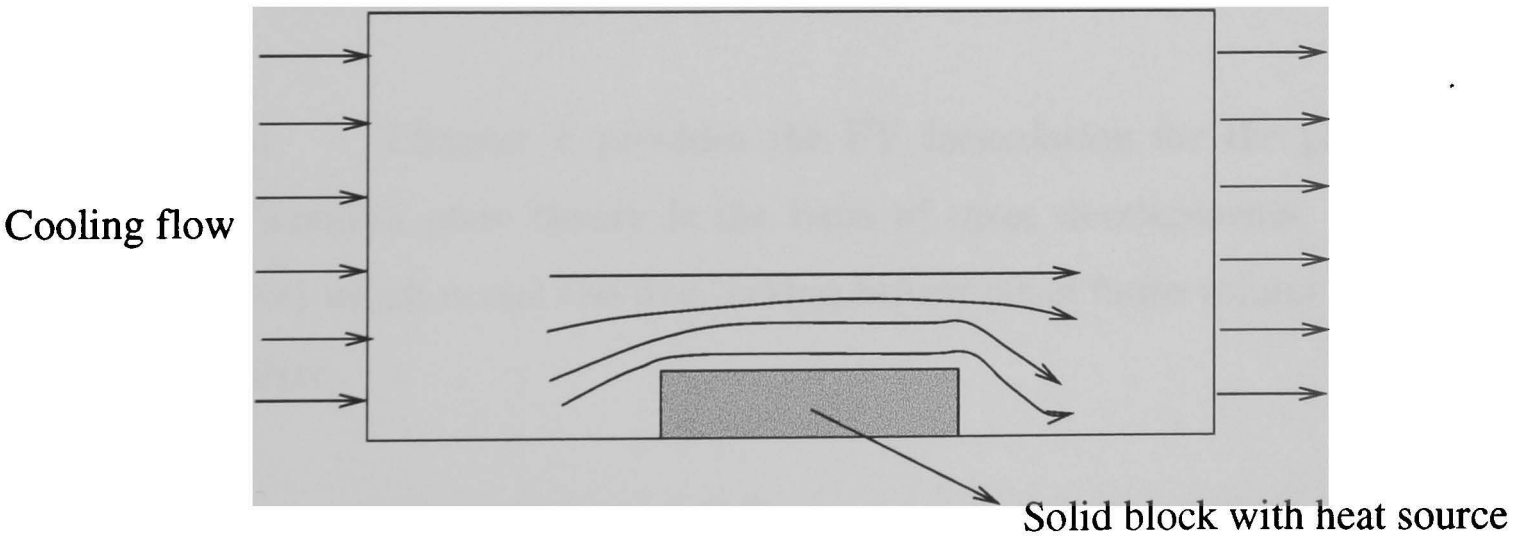

Figure 1.2: Heated solid block with cooling flow

1.5 Layout of the thesis

Chapter 2: Chapter two provides the foundation for the developments presented in chapter four, five and six. In this chapter the governing equations for the large deformation are described. Different definitions related to the large strain concept are explained. When deformation breaks through the small strain barrier (5%) the body is deformed and displaced considerably, so careful attention should be taken in the stress definition. This chapter also includes different stress definitions in both the Eulerian and Lagrangian frame works.

Chapter 3: Chapter three discusses different discretization techniques for the finite volume approach and includes properties of elements applied in the thesis.

Chapter 4: Chapter four provides a comprehensive discussions of geometrically nonlinear problems. The generic formulation for analysis of this type of nonlinearity is presented and will show the fundamental difference between Bubnov-Galerkin finite element method and finite volume method. Based on the provided formulations some standard elastic test cases in static situations are analysed by both FEM and FVM.

Chapter 5: Chapter 5 provides the FV formulation for the plate analysis. Reissner/Mindlin plate theory is the basis of these developments. Some test cases are studied which reveal the free locking behaviour of finite volume method in thin plate analysis.

Chapter 6: This chapter includes a new scope of finite volume application for solid mechanics problems. This chapter presents discussions for enhancing the capability of a CFD code for analysis of stress-flow-thermal coupled problems. Some test cases involving pure solid problems and multiphysics problems are analysed.

Chapter 7: Finally chapter 7 provides the conclusions and suggestions for future research.

Chapter 2

Mechanics of Solids

A review of some of the basic concepts of continuum mechanics which are required in the formulation and numerical analysis presented in subsequent chapters is necessary. The fundamental issues related to the kinematics, stress and equilibrium equations for solid materials are briefly addressed. This chapter consists of three main sections. In the first section the motion of a continuum body and the expressions for different strain and deformation measures are presented. The second section details different stress measures in terms of the initial and current configurations of the body. Finally the third section deals with the equilibrium equations using the principle of momentum .

2.1 Kinematics

Describing the motion of a deformable body requires knowledge of "where it is" and "where it was" (Figure 2.1). The description used depends on initial configuration at time $t = 0$ or current configuration at time t. There are two main classes for describing the motion of a continuum.

- **Lagrangian or Material description**

  In this method all behaviour is described in terms of the initial particle coordinates $\mathbf{X}$ at time $t = 0$. Then "where the particle is" is given in terms of

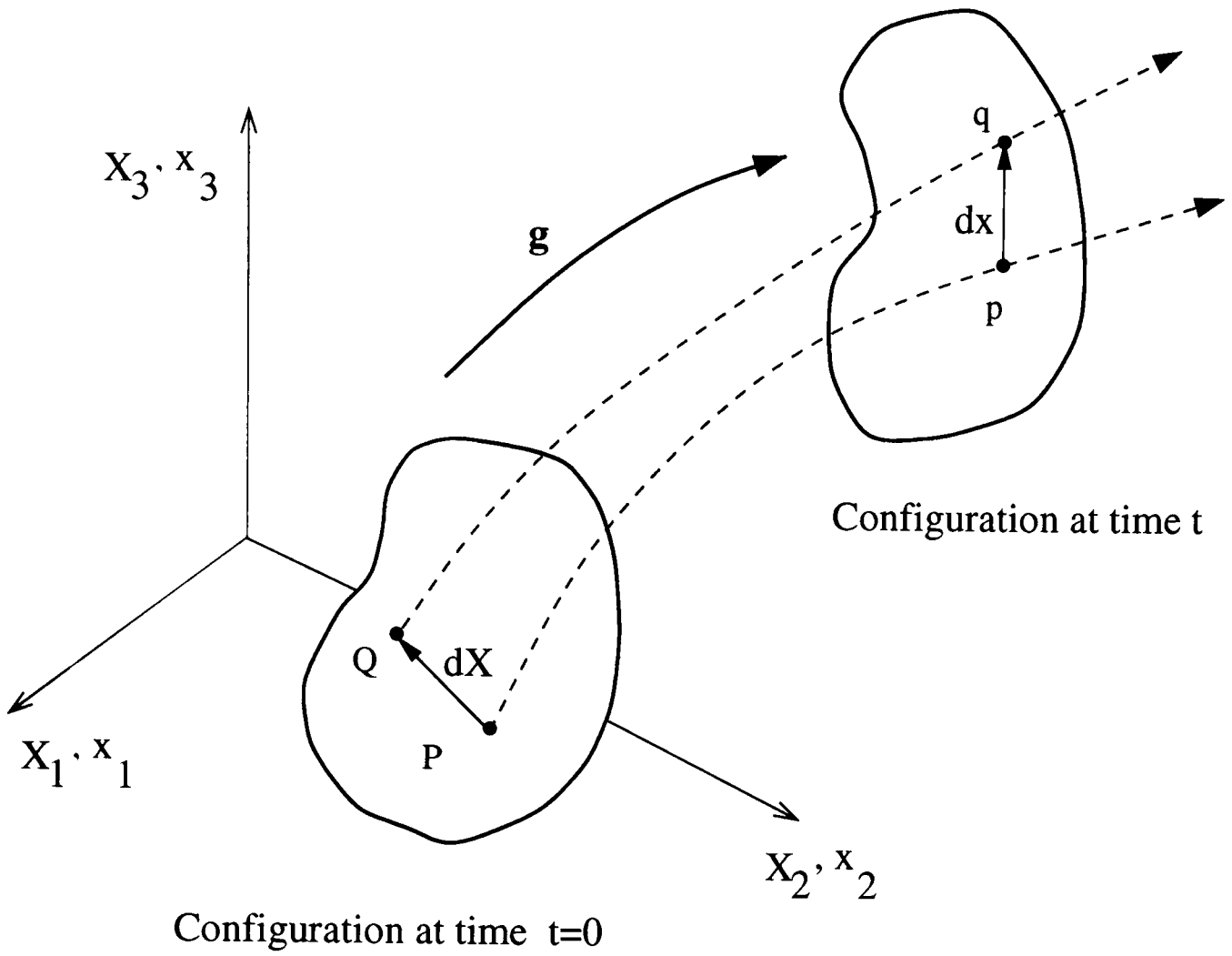

Figure 2.1: Motion of a deformable body

"where it was" as:

$$\mathbf{x} = g(\mathbf{X}, t) \tag{2.1}$$

Where $\mathbf{X}$ and $\mathbf{x}$ are the position vectors of a particle in the initial and the current configurations respectively.

- **Eulerian description**

  In this method all behaviour is presented in terms of the current position of a particle at time t, hence "where the particle was" is given in terms of "where it is" as:

$$\mathbf{X} = G(\mathbf{x}, t) \tag{2.2}$$

The Lagrangian description seems to be the more suitable one in elastic solids [34] where there is usually a natural undeformed state to which the body would return

when it is unloaded. But the equations of motion, or equilibrium equations, must be satisfied in the deformed or contemporary configuration and stress is therefore defined in the deformed configuration. The Lagrangian approach is not generally used in fluid mechanics as it leads to more cumbersome equations [35]. This is avoided by using the Eulerian approach for fluids. For solids, the Lagrangian approach is usually adopted especially in small strain analysis.

2.1.1 Finite Deformation and Finite Strain

In finite deformation analysis based upon the different description methods of deformation, various measures for the deformation and strain are possible. Since the deformaton gradient tensor, $\mathbf{F}$, is the key variable for the description of the deformation and strain measures, before going ahead, this tensor is presented first.

2.1.2 Deformation gradient tensor

The deformation gradient tensor is defined as the derivative of the mapping $\mathbf{g}$ as:

$$\mathbf{F} = \frac{\partial \mathbf{x}}{\partial \mathbf{X}} \tag{2.3}$$

It enables an elemental vector of $d\mathbf{x}$, see Figure 2.1, to be obtained in terms of initial vector of $d\mathbf{X}$ as:

$$d\mathbf{x} = \mathbf{F} \cdot d\mathbf{X} \tag{2.4}$$

Or inversely:

$$d\mathbf{X} = \mathbf{F}^{-1} \cdot d\mathbf{x} \tag{2.5}$$

The cartesian components of $\mathbf{F}$ would be:

$$F_{ij} = \frac{\partial x_i}{\partial X_j} \tag{2.6}$$

Where in the three dimensional case can be presented in a matrix form by:

$$\mathbf{F} = \begin{bmatrix} \frac{\partial x_1}{\partial X_1} & \frac{\partial x_1}{\partial X_2} & \frac{\partial x_1}{\partial X_3} \\ \frac{\partial x_2}{\partial X_1} & \frac{\partial x_2}{\partial X_2} & \frac{\partial x_2}{\partial X_3} \\ \frac{\partial x_3}{\partial X_1} & \frac{\partial x_3}{\partial X_2} & \frac{\partial x_3}{\partial X_3} \end{bmatrix} \tag{2.7}$$

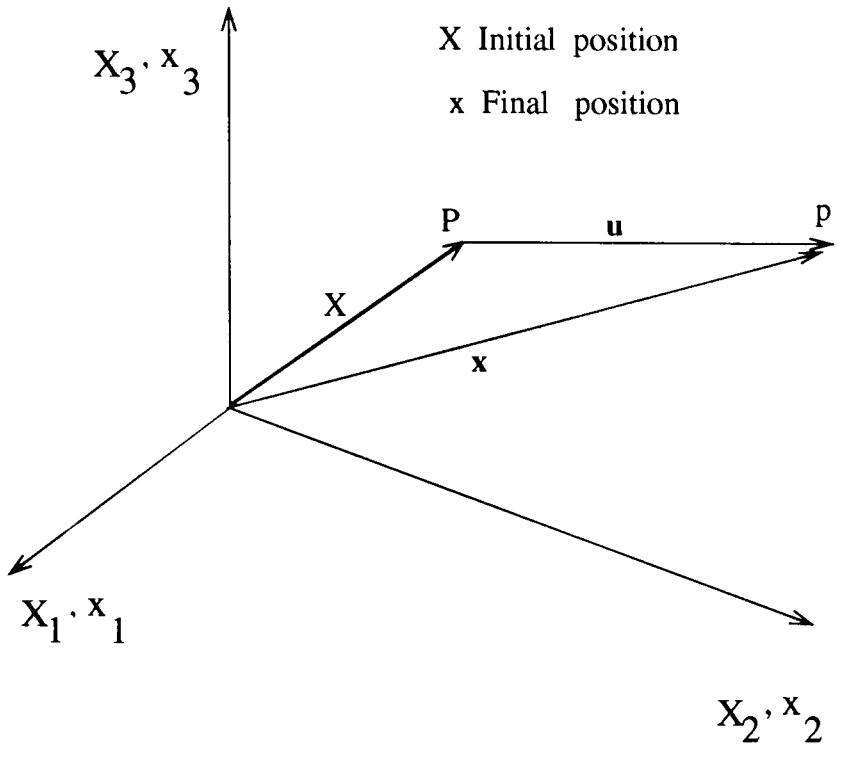

Figure 2.2: Initial and current position of particle P

With regards to relation of $\mathbf{x}$ and $\mathbf{X}$ from Figure 2.2:

$$\mathbf{x} = \mathbf{X} + \mathbf{u}(X_1, X_2, X_3, t) \tag{2.8}$$

tensor $\mathbf{F}$ can be expressed in terms of derivative of displacement components $\mathbf{u}$ as:

$$\mathbf{F} = \begin{bmatrix} \frac{\partial u_1}{\partial X_1} + 1 & \frac{\partial u_1}{\partial X_2} & \frac{\partial u_1}{\partial X_3} \\ \frac{\partial u_2}{\partial X_1} & \frac{\partial u_2}{\partial X_2} + 1 & \frac{\partial u_2}{\partial X_3} \\ \frac{\partial u_3}{\partial X_1} & \frac{\partial u_3}{\partial X_2} & \frac{\partial u_3}{\partial X_3} + 1 \end{bmatrix} = \begin{bmatrix} \frac{\partial u_1}{\partial X_1} & \frac{\partial u_1}{\partial X_2} & \frac{\partial u_1}{\partial X_3} \\ \frac{\partial u_2}{\partial X_1} & \frac{\partial u_2}{\partial X_2} & \frac{\partial u_2}{\partial X_3} \\ \frac{\partial u_3}{\partial X_1} & \frac{\partial u_3}{\partial X_2} & \frac{\partial u_3}{\partial X_3} \end{bmatrix} + \begin{bmatrix} 1 & 0 & 0 \\ 0 & 1 & 0 \\ 0 & 0 & 1 \end{bmatrix} = \mathbf{H} + \mathbf{I} \tag{2.9}$$

Where $\mathbf{H}$ is displacement derivative matrix and $\mathbf{I}$ is identity matrix. The deformation gradient matrix $\mathbf{F}$ contains information about the:

- Volume change,
- Rotation,
- Shape change due to straining,

which will be explained in detail later and hence can lead us to strain measures.

2.1.3 Green-Lagrange and Almansi strain tensors

If the material vector $d\mathbf{X}$ with length of dL is deformed to associated vector $d\mathbf{x}$ with length of dl, the strain tensors are defined so that they give the change in the squared length of the material vector $\mathbf{dX}$. Green-Lagrange strain tensor $\mathbf{E}$ is defined [36] as:

$$(dl)^2 - (dL)^2 = 2d\mathbf{X} \cdot \mathbf{E} \cdot d\mathbf{X} \tag{2.10}$$

The Almansi strain tensor $\mathbf{E}^*$, also called the Eulerian strain tensor, is defined [36] as:

$$(dl)^2 - (dL)^2 = 2d\mathbf{x} \cdot \mathbf{E}^* \cdot d\mathbf{x} \tag{2.11}$$

Where:

$$(dl)^2 = d\mathbf{x} \cdot d\mathbf{x} \tag{2.12}$$

$$(dL)^2 = d\mathbf{X} \cdot d\mathbf{X} \tag{2.13}$$

by substituting of equations (2.4),(2.5) into two latter equations:

$$(dl)^2 = d\mathbf{X} \cdot \mathbf{F^T} \cdot \mathbf{F} \cdot d\mathbf{X} = d\mathbf{X} \cdot (\mathbf{F}^T \cdot \mathbf{F}) \cdot d\mathbf{X} \tag{2.14}$$

$$(dL)^2 = d\mathbf{x} \cdot (\mathbf{F}^{-1})^T \cdot \mathbf{F}^{-1} \cdot d\mathbf{x} = d\mathbf{x} \cdot [(\mathbf{F}^{-1})^T \cdot \mathbf{F}^{-1}] \cdot d\mathbf{x} \tag{2.15}$$

The quantities, $(dl)^2$ and $(dL)^2$, can be calculated by use of tensor $\mathbf{C}$, the Green deformation tensor [34], and $\mathbf{B}^{-1}$, the Cauchy deformation tensor [34], which are defined as:

$$(dl)^2 = d\mathbf{X} \cdot \mathbf{C} \cdot d\mathbf{X} \tag{2.16}$$

$$(dL)^2 = d\mathbf{x} \cdot \mathbf{B}^{-1} \cdot d\mathbf{x} \tag{2.17}$$

By comparing equations (2.10),(2.11) and (2.16),(2.17) we obtain the following relationship between the deformation tensors and strain tensors:

$$2\mathbf{E} = \mathbf{C} - \mathbf{I} \tag{2.18}$$

$$2\mathbf{E}^* = \mathbf{I} - \mathbf{B}^{-1} \tag{2.19}$$

Where $\mathbf{I}$ is the identity tensor. Comparing equations (2.14),(2.15) and equations (2.16),(2.17) gives that:

$$\mathbf{C} = \mathbf{F}^T \cdot \mathbf{F} \tag{2.20}$$

$$\mathbf{B}^{-1} = (\mathbf{F}^{-1})^T \cdot \mathbf{F}^{-1} \tag{2.21}$$

So strain tensors can be rewritten as follows:

$$\mathbf{E} = \frac{1}{2}[\mathbf{F}^T \cdot \mathbf{F} - \mathbf{I}] \tag{2.22}$$

$$\mathbf{E}^* = \frac{1}{2}[\mathbf{I} - (\mathbf{F}^{-1})^T \cdot \mathbf{F}^{-1}] \tag{2.23}$$

For comparison with the small strain tensor, by using equations (2.7) and (2.8), the Green-Lagrange strain tensor $\mathbf{E}$ is expressed in terms of the displacement derivatives as follows (in the initial configuration):

$$\mathbf{E} = \begin{bmatrix} \epsilon_{11} \\ \epsilon_{22} \\ \epsilon_{33} \\ \epsilon_{12} \\ \epsilon_{13} \\ \epsilon_{23} \end{bmatrix} = \begin{bmatrix} \frac{\partial u_1}{\partial X_1} \\ \frac{\partial u_2}{\partial X_2} \\ \frac{\partial u_3}{\partial X_3} \\ \frac{1}{2}[\frac{\partial u_1}{\partial X_2} + \frac{\partial u_2}{\partial X_1}] \\ \frac{1}{2}[\frac{\partial u_1}{\partial X_3} + \frac{\partial u_3}{\partial X_1}] \\ \frac{1}{2}[\frac{\partial u_2}{\partial X_3} + \frac{\partial u_3}{\partial X_2}] \end{bmatrix} + \begin{bmatrix} \frac{1}{2}((\frac{\partial u_1}{\partial X_1})^2 + (\frac{\partial u_2}{\partial X_1})^2 + (\frac{\partial u_3}{\partial X_1})^2) \\ \frac{1}{2}((\frac{\partial u_1}{\partial X_2})^2 + (\frac{\partial u_2}{\partial X_2})^2 + (\frac{\partial u_3}{\partial X_2})^2) \\ \frac{1}{2}((\frac{\partial u_1}{\partial X_3})^2 + (\frac{\partial u_2}{\partial X_3})^2 + (\frac{\partial u_3}{\partial X_3})^2) \\ \frac{1}{2}[(\frac{\partial u_1}{\partial X_1})(\frac{\partial u_1}{\partial X_2}) + (\frac{\partial u_2}{\partial X_1})(\frac{\partial u_2}{\partial X_2}) + (\frac{\partial u_3}{\partial X_1})(\frac{\partial u_3}{\partial X_2})] \\ \frac{1}{2}[(\frac{\partial u_1}{\partial X_1})(\frac{\partial u_1}{\partial X_3}) + (\frac{\partial u_2}{\partial X_1})(\frac{\partial u_2}{\partial X_3}) + (\frac{\partial u_3}{\partial X_1})(\frac{\partial u_3}{\partial X_3})] \\ \frac{1}{2}[(\frac{\partial u_1}{\partial X_2})(\frac{\partial u_1}{\partial X_3}) + (\frac{\partial u_2}{\partial X_2})(\frac{\partial u_2}{\partial X_3}) + (\frac{\partial u_3}{\partial X_2})(\frac{\partial u_3}{\partial X_3})] \end{bmatrix} \tag{2.24}$$

Or in index form:

$$E_{ij} = \frac{1}{2}[\frac{\partial u_i}{\partial X_j} + \frac{\partial u_j}{\partial X_i}] + \frac{1}{2}\frac{\partial u_k}{\partial X_i}\frac{\partial u_k}{\partial X_j} \tag{2.25}$$

By use of equation (2.7) and the following equation:

$$\mathbf{X} = \mathbf{x} - \mathbf{u}(x_1, x_2, x_3, t) \tag{2.26}$$

The Almansi strain tensor $\mathbf{E}^*$ can also be expressed in terms of the displacement gradients as follows (in the current configuration):

$$\mathbf{E}^* = \begin{bmatrix} \epsilon_{11}^* \\ \epsilon_{22}^* \\ \epsilon_{33}^* \\ \epsilon_{12}^* \\ \epsilon_{13}^* \\ \epsilon_{23}^* \end{bmatrix} = \begin{bmatrix} \frac{\partial u_1}{\partial x_1} \\ \frac{\partial u_2}{\partial x_2} \\ \frac{\partial u_3}{\partial x_3} \\ \frac{1}{2}[\frac{\partial u_1}{\partial x_2} + \frac{\partial u_2}{\partial x_1}] \\ \frac{1}{2}[\frac{\partial u_1}{\partial x_3} + \frac{\partial u_3}{\partial x_1}] \\ \frac{1}{2}[\frac{\partial u_2}{\partial x_3} + \frac{\partial u_3}{\partial x_2}] \end{bmatrix} - \begin{bmatrix} \frac{1}{2}((\frac{\partial u_1}{\partial x_1})^2 + (\frac{\partial u_2}{\partial x_1})^2 + (\frac{\partial u_3}{\partial x_1})^2) \\ \frac{1}{2}((\frac{\partial u_1}{\partial x_2})^2 + (\frac{\partial u_2}{\partial x_2})^2 + (\frac{\partial u_3}{\partial x_2})^2) \\ \frac{1}{2}((\frac{\partial u_1}{\partial x_3})^2 + (\frac{\partial u_2}{\partial x_3})^2 + (\frac{\partial u_3}{\partial x_3})^2) \\ \frac{1}{2}[(\frac{\partial u_1}{\partial x_1})(\frac{\partial u_1}{\partial x_2}) + (\frac{\partial u_2}{\partial x_1})(\frac{\partial u_2}{\partial x_2}) + (\frac{\partial u_3}{\partial x_1})(\frac{\partial u_3}{\partial x_2})] \\ \frac{1}{2}[(\frac{\partial u_1}{\partial x_1})(\frac{\partial u_1}{\partial x_3}) + (\frac{\partial u_2}{\partial x_1})(\frac{\partial u_2}{\partial x_3}) + (\frac{\partial u_3}{\partial x_1})(\frac{\partial u_3}{\partial x_3})] \\ \frac{1}{2}[(\frac{\partial u_1}{\partial x_2})(\frac{\partial u_1}{\partial x_3}) + (\frac{\partial u_2}{\partial x_2})(\frac{\partial u_2}{\partial x_3}) + (\frac{\partial u_3}{\partial x_2})(\frac{\partial u_3}{\partial x_3})] \end{bmatrix} \tag{2.27}$$

Or in index form:

$$E_{ij}^* = \frac{1}{2}[\frac{\partial u_i}{\partial x_j} + \frac{\partial u_j}{\partial x_i}] - \frac{1}{2}\frac{\partial u_k}{\partial x_i}\frac{\partial u_k}{\partial x_j} \tag{2.28}$$

It is noticeable in equations (2.24), (2.27) the first bracket is a linear function of the displacement derivatives and shows the small strain vector and the second bracket, which contains squared displacement derivatives, appears only in large deformation analysis and is negligible in small strain problems.

2.1.4 Stretch and Angle change

Stretch or stretch ratio is denoted as $\frac{dl}{dL}$ where dL is length of element $d\mathbf{X}$ in undeformed configuration and dl is length of element dx in deformed configuration. We denote the stretch of the element whose initial direction is $\mathbf{N}$ by $\Lambda_{(N)}$ and the stretch of the element whose current direction is $\mathbf{n}$ by $\lambda_{(n)}$. By dividing equation (2.16) and (2.17) by $(dL)^2$ and $(dl)^2$ respectively, we obtain:

$$\Lambda_{(N)}{}^2 = \mathbf{N} \cdot \mathbf{C} \cdot \mathbf{N} \qquad \text{where} \qquad \mathbf{N} = \frac{d\mathbf{X}}{dL} \tag{2.29}$$

$$\frac{1}{\lambda_{(n)}{}^2} = \mathbf{n} \cdot \mathbf{B}^{-1} \cdot \mathbf{n} \qquad \text{where} \qquad \mathbf{n} = \frac{d\mathbf{x}}{dl} \tag{2.30}$$

It is obvious that the stretch of the element initially parallel to the axis of X_1 for which $\mathbf{N}$ has components (1,0,0) is denoted by $\Lambda_{(1)}$ is given by:

$$\Lambda_{(1)}{}^2 = \mathbf{C}_{11} = 1 + 2\mathbf{E}_{11} \tag{2.31}$$

While the stretch of the element currently parallel to the axis x_1 denoted by $\lambda_{(1)}$ is given by

$$\frac{1}{{\lambda_{(1)}}^2} = \mathbf{B}_{11}^{-1} = 1 - 2\mathbf{E}_{11}^{*} \tag{2.32}$$

Equations (2.31) and (2.32) show that diagonal components of tensor $\mathbf{C}$ and tensor $\mathbf{B}^{-1}$ in the rectangular cartesian are positive and the diagonal elements of $\mathbf{E}$ must be greater than $\frac{-1}{2}$ and those for $\mathbf{E}^{*}$ must be less than $\frac{1}{2}$.

If $\cos(\mathbf{n_1}, \mathbf{n_2})$ denotes the cosine of the angle between elements $d\mathbf{x}_1$ and $d\mathbf{x}_2$ correspond to two material elements $d\mathbf{X}_1$ and $d\mathbf{X}_2$ respectively in the undeformed configuration, then:

$$cos(\mathbf{n_1}, \mathbf{n_2}) = \mathbf{n_1} \cdot \mathbf{n_2} = \frac{d\mathbf{x}_1 \cdot d\mathbf{x}_2}{|d\mathbf{x}_1||d\mathbf{x}_2|} =$$

$$\frac{[d\mathbf{X}_1 \cdot \mathbf{F}^T] \cdot [\mathbf{F} \cdot d\mathbf{X}_2]}{\sqrt{d\mathbf{X_1} \cdot \mathbf{C} \cdot d\mathbf{X_1}}\sqrt{d\mathbf{X_2} \cdot \mathbf{C} \cdot d\mathbf{X_2}}} = \tag{2.33}$$

$$\frac{d\mathbf{X_1} \cdot (\mathbf{F}^T \cdot \mathbf{F}) \cdot d\mathbf{X_2}}{|d\mathbf{X_1}|\sqrt{\mathbf{N_1} \cdot \mathbf{C} \cdot \mathbf{N_1}}|d\mathbf{X_2}|\sqrt{\mathbf{N_2} \cdot \mathbf{C} \cdot \mathbf{N_2}}} = \frac{\mathbf{N_1} \cdot \mathbf{C} \cdot \mathbf{N_2}}{\Lambda_{(N_1)} \cdot \Lambda_{(N_2)}}$$

Let θ_{12} denote the angle between the deformed elements which were initially parallel to the $\mathbf{X}_1$ and $\mathbf{X}_2$ cartesian axes. Then $\mathbf{N}_1$ has components (1,0,0), $\mathbf{N}_2$ has components (0.1,0) and

$$cos\theta_{12} = \frac{2\mathbf{E}_{12}}{\sqrt{(1 + 2\mathbf{E}_{11})(1 + 2\mathbf{E}_{22})}} \tag{2.34}$$

This equation indicates in general the angle change (shear deformation) not only depends on the shear components of the finite strain tensor but also depends on the stretches of the elements involved, thus different to the small strain case.

2.1.5 Surface change and volume change

Referring to Figure 2.3 an initial surface dS_o with sides of $d\mathbf{X}_a, d\mathbf{X}_b$ being moved to a deformed surface ds with sides of $d\mathbf{x}_a, d\mathbf{x}_b$, we have:

$$d\mathbf{A}_o = dS_o\mathbf{N} = d\mathbf{X}_a \times d\mathbf{X}_b =$$

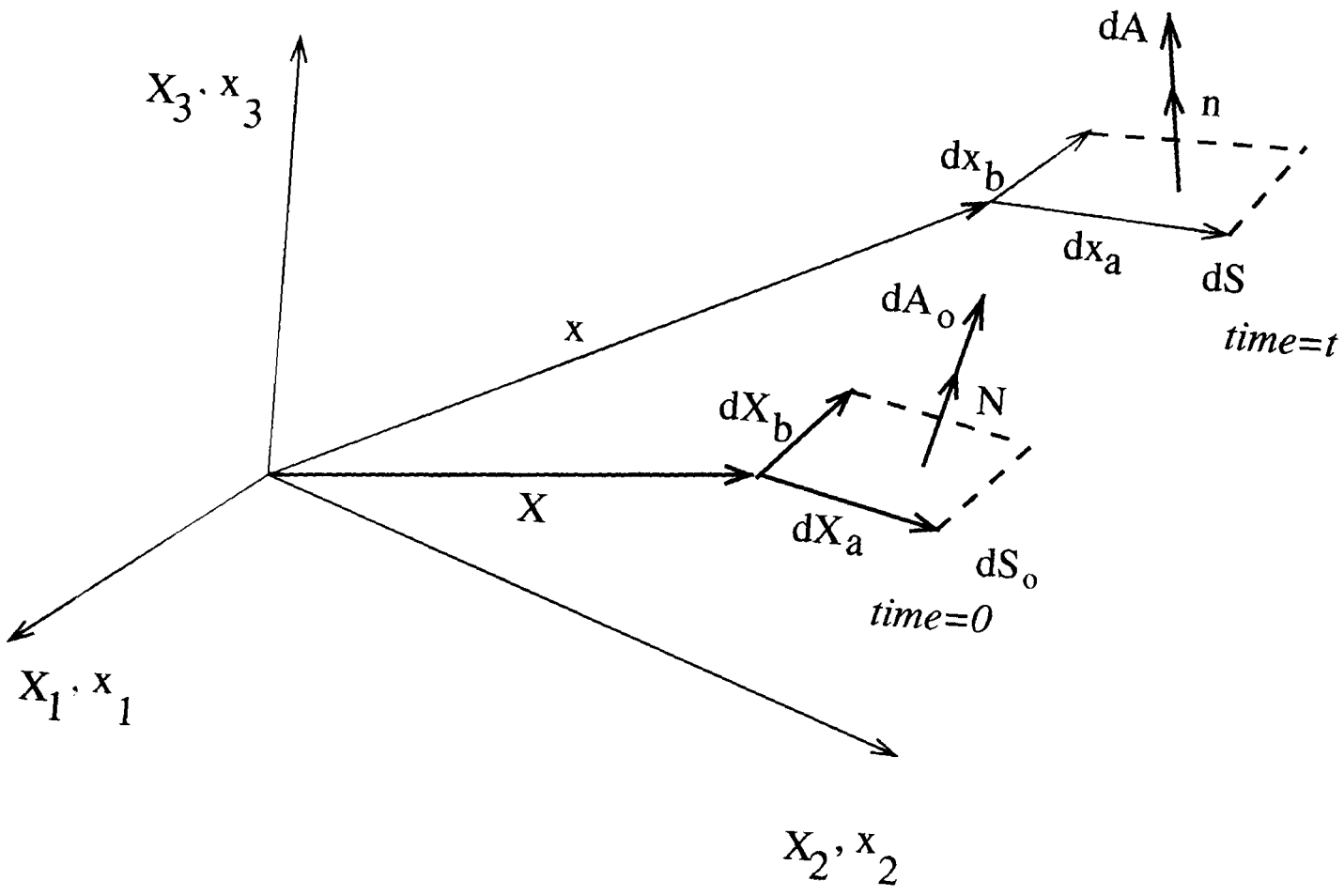

Figure 2.3: Change of area during the deformation

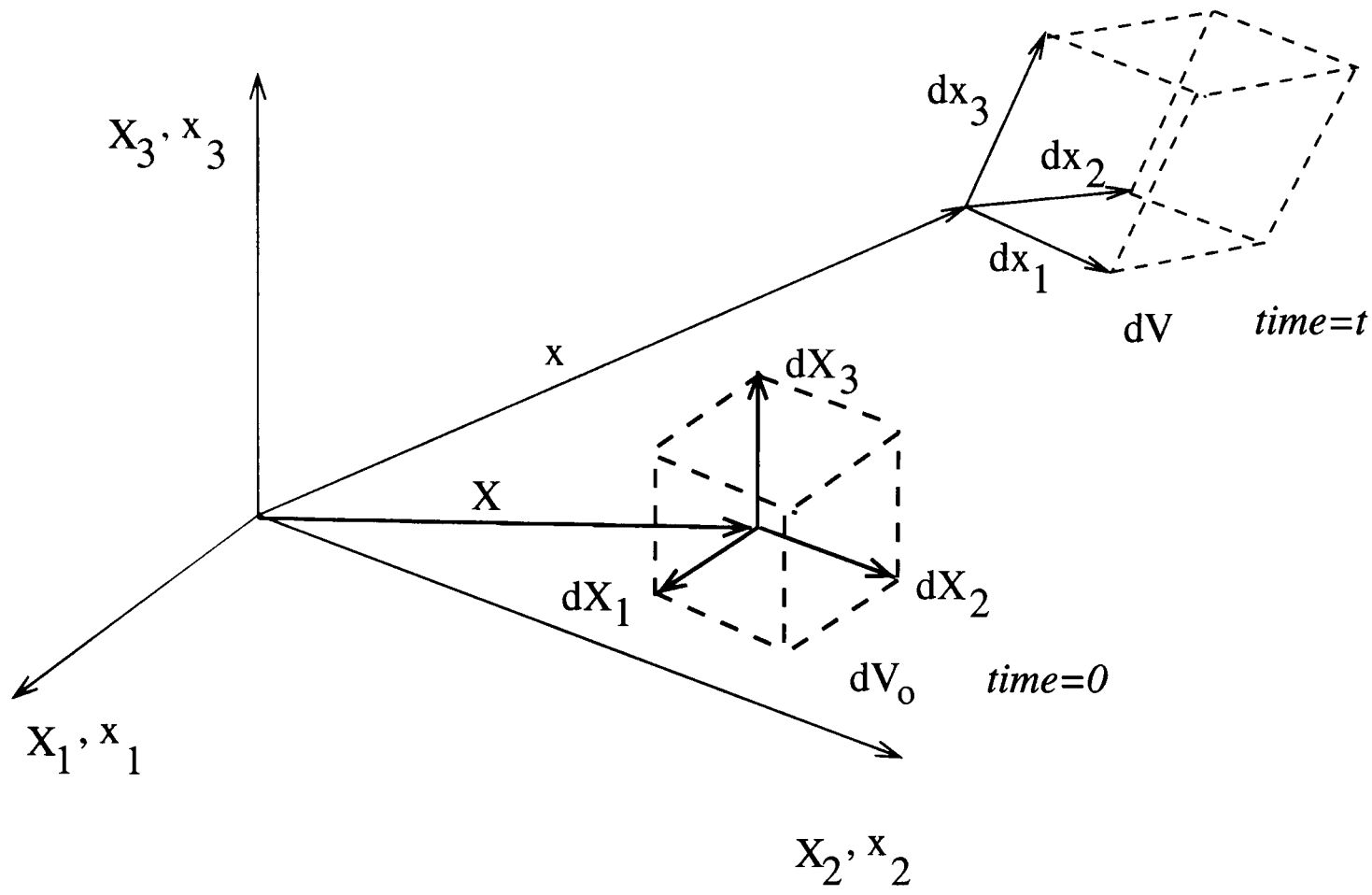

Figure 2.4: Change of volume during the deformation

$$\mathbf{F}^{-1} \cdot d\mathbf{x}_a \times \mathbf{F}^{-1} \cdot d\mathbf{x}_b = \frac{1}{J}\mathbf{F}^T \cdot (d\mathbf{x}_a \times d\mathbf{x}_b) =$$

$$\frac{1}{J}\mathbf{F}^T \mathbf{n} dS = \frac{1}{J}\mathbf{F}^T \cdot d\mathbf{A} \tag{2.35}$$

Where J is determinant of the deformation gradient $\mathbf{F}$. Equation (2.35) is known as Nanson's formula. Figure (2.4) shows an infinitesimal volume element in the undeformed configuration with sides parallel to the cartesian axes given by $d\mathbf{X}_1, d\mathbf{X}_2$ and $d\mathbf{X}_3$. The elemental material volume dV_o is given as:

$$dV_o = dX_1 dX_2 dX_3 \tag{2.36}$$

In order to calculate the corresponding deformed volume dV in the spatial configuration, the corresponding deformed sides are:

$$d\mathbf{x}_1 = \mathbf{F} \cdot d\mathbf{X}_1 = \frac{\partial \mathbf{x}}{\partial X_1} d\mathbf{X_1} \tag{2.37}$$

$$d\mathbf{x}_2 = \mathbf{F} \cdot d\mathbf{X}_2 = \frac{\partial \mathbf{x}}{\partial X_2} d\mathbf{X_2} \tag{2.38}$$

$$d\mathbf{x}_3 = \mathbf{F} \cdot d\mathbf{X}_3 = \frac{\partial \mathbf{x}}{\partial X_3} d\mathbf{X_3} \tag{2.39}$$

The triple product of these vectors gives the deformed volume dV as:

$$dV = d\mathbf{x}_1 \cdot (d\mathbf{x}_2 \times d\mathbf{x}_3) = \frac{\partial \mathbf{x}}{\partial X_1} \cdot (\frac{\partial \mathbf{x}}{\partial X_2} \times \frac{\partial \mathbf{x}}{\partial X_3}) dX_1 dX_2 dX_3 \tag{2.40}$$

The above triple product is the determinant of $\mathbf{F}$ so equation (2.40) gives the deformed volume in terms of the Jacobian J as:

$$dV = J dV_o \quad ; \quad J = det[\mathbf{F}] \tag{2.41}$$

With regards to above discussion the mass element can be expressed in terms of the initial and current parameters as:

$$dm = \rho_o dV_o = \rho dV \tag{2.42}$$

Where ρ_o and ρ are initial and current density respectively. Substitution of equation (2.41) into above equation, gives:

$$\rho_o = \rho J \tag{2.43}$$

The equation (2.43) is referred to as the conservation of mass or continuity equation.

2.2 Stress

The stress definition can be affected by significant changes in initial configuration caused by finite (large) deformation . There are some stress definitions which can be transformed to each other. The main difference between them is that some of them refer to the initial configuration and the others refer to the current deformed configuration. In this section the following stress definitions will be presented:

- Cauchy stress.
- The first Piola-Kirchhoff stress.

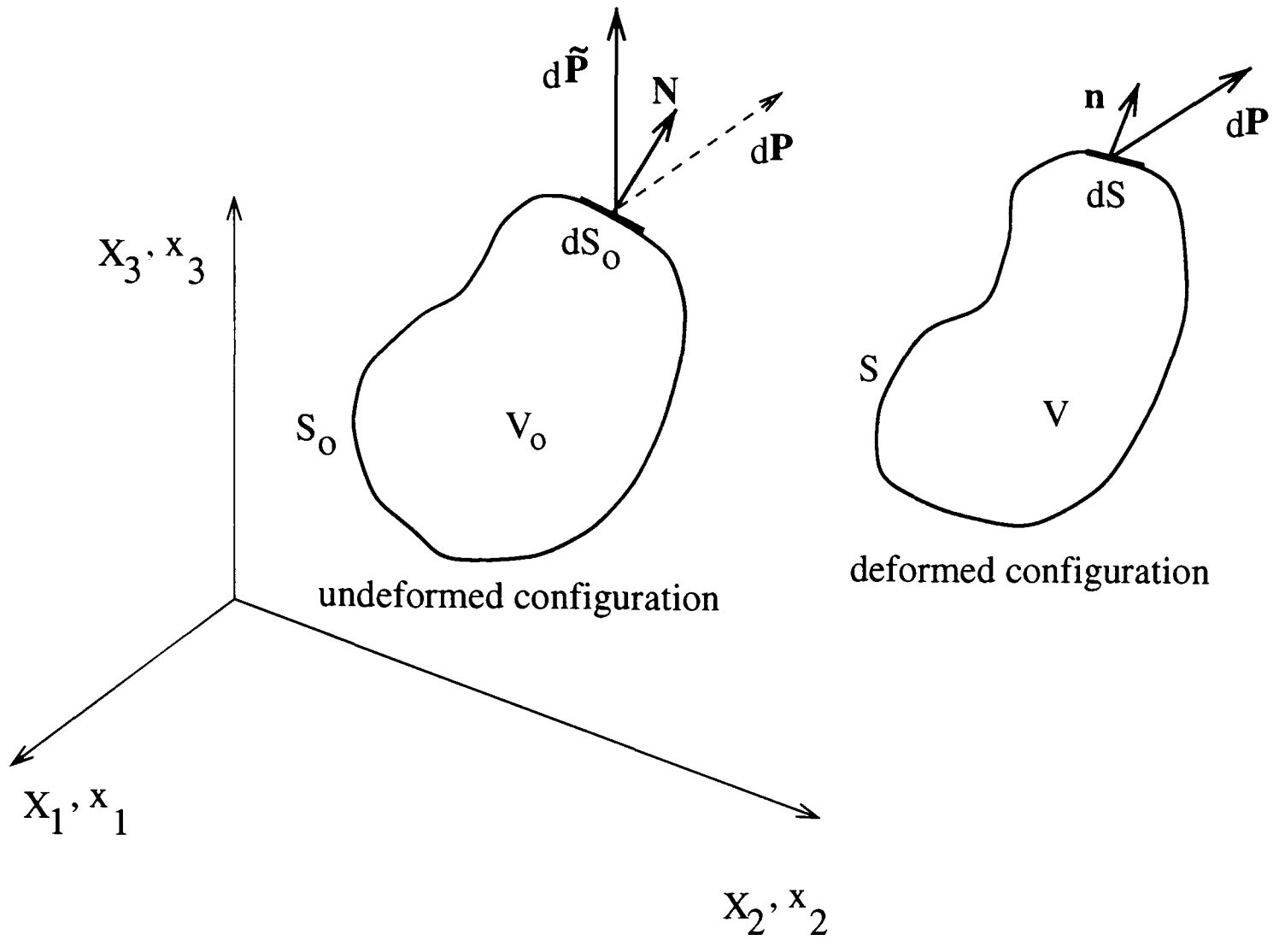

Figure 2.5: Undeformed/deformed configurations and acting forces

- The second Piola-Kirchhoff stress.

Because the internal energy (or deformation energy) corresponding to a deformed body is independent of the type of stress measure that is used in the calculation, each stress definition conjugates to the associated strain measure. This relation between stress and strain is called work conjugacy [37]. The Cauchy stress tensor, $\boldsymbol{\sigma}$, is defined as a function of the spatial coordinate $\mathbf{x}$ and is a symmetric tensor. When we use material coordinate system for strain definition (i.e. Green-Lagrange strain) we also need to express the associated stress as a function of $\mathbf{X}$. The first and the second Piola-Kirchhoff stress tensors both refer to the initial configuration. The first Piola-Kirchhoff stress tensor $\mathbf{T}^o$ gives the actual force $\mathrm{d}\mathbf{P}$ which acts on the deformed area dS but it is measured per unit of the undeformed area dS_o at $\mathbf{X}$.

With reference to Figure 2.5 the force vector $d\mathbf{P}$ can be calculated as:

$$(\mathbf{N} \cdot \mathbf{T}^o) dS_o = d\mathbf{P} = (\mathbf{n} \cdot \boldsymbol{\sigma}) dS \tag{2.44}$$

The second Piola-Kirchhoff stress tensor $\tilde{\boldsymbol{\sigma}}$ is formulated somehow differently. Instead of the actual force $\mathrm{d}\mathbf{P}$ on dS it gives a force $d\tilde{\mathbf{P}}$ related to the force $\mathrm{d}\mathbf{P}$ in the same way that a material vector $\mathrm{d}\mathbf{X}$ at $\mathbf{X}$ is related to the corresponding spatial vector $\mathrm{d}\mathbf{x}$ at $\mathbf{x}$. That is :

$$d\tilde{\mathbf{P}} = \mathbf{F}^{-1} \cdot d\mathbf{P} \qquad \text{the same as} \qquad d\mathbf{X} = \mathbf{F}^{-1} \cdot d\mathbf{x} \tag{2.45}$$

Where $\mathbf{F} = \frac{\partial \mathbf{x}}{\partial \mathbf{X}}$ and:

$$(\mathbf{N} \cdot \tilde{\boldsymbol{\sigma}}) dS_o = d\tilde{\mathbf{P}} = \mathbf{F}^{-1} \cdot d\mathbf{P} = \mathbf{F}^{-1} \cdot (\mathbf{n} \cdot \boldsymbol{\sigma}) dS = (\mathbf{n} \cdot \boldsymbol{\sigma}) \cdot (\mathbf{F}^{-1})^T dS \tag{2.46}$$

The Piola-Kirchhoff stress tensors are sometimes considered as pseudo-stress tensors and we can define pseudo-traction vector $\mathbf{t}^o$ and $\tilde{\mathbf{t}}$ such that:

$$\mathbf{t}^o dS_o = d\mathbf{P} = \mathrm{t} dS \tag{2.47}$$

$$\tilde{\mathbf{t}} dS_o = d\tilde{\mathbf{P}} = \mathbf{F}^{-1} \cdot d\mathbf{P} = \mathbf{F}^{-1} \cdot \mathbf{t}^o dS_o = \mathbf{F}^{-1} \cdot \mathrm{t} dS \tag{2.48}$$

$\mathbf{t}^o$ is the force acting on the deformed area per unit undeformed area, while $\tilde{t}$ is the dot product of F^{-1} into the force acting on the deformed area per unit of the undeformed area. Substituting Nanson's formula, equation (2.35), into equation (2.44) gives:

$$(\mathbf{N} \cdot \mathbf{T}^o) dS_o = J\mathbf{N} \cdot \mathbf{F}^{-1} dS_o \cdot \boldsymbol{\sigma} = [\mathbf{N} \cdot (J\mathbf{F}^{-1} \cdot \tilde{\boldsymbol{\sigma}})] dS_o \tag{2.49}$$

$\mathbf{N}$ is arbitrary unit normal vector so:

$$\mathbf{T}^o = J\mathbf{F}^{-1} \cdot \boldsymbol{\sigma} \tag{2.50}$$

Relation between the second Piola-Kirchhoff stress tensor and the other stress tensors can be established. Starting from equation (2.46) and using the Nanson's formula gives:

$$(\mathbf{N} \cdot \tilde{\boldsymbol{\sigma}}) dS_o = [\mathbf{N} \cdot J\mathbf{F}^{-1} \cdot \boldsymbol{\sigma} \cdot (\mathbf{F}^{-1})^T] dS_o \tag{2.51}$$

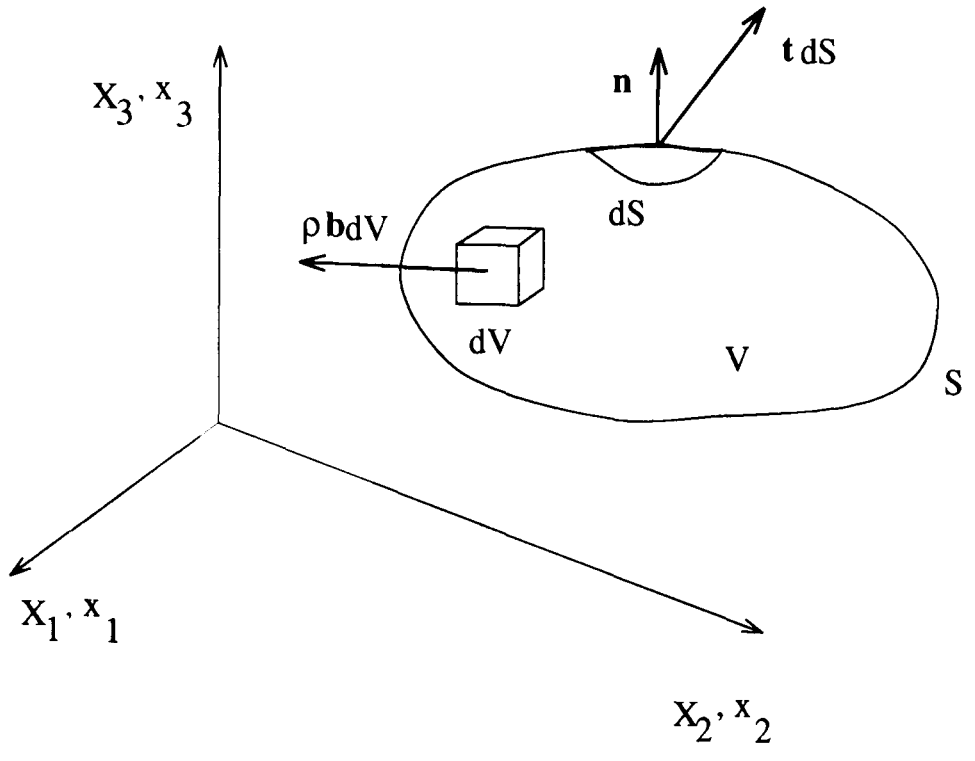

Figure 2.6: Contemporary position of a body with acting forces

This equation is valid for arbitrary unit vector **N** so:

$$\tilde{\boldsymbol{\sigma}} = J\mathbf{F}^{-1} \cdot \boldsymbol{\sigma} \cdot \left(\mathbf{F}^{-1}\right)^{T} \tag{2.52}$$

or by use of equation (2.50):

$$\tilde{\boldsymbol{\sigma}} = \mathbf{T}^{o} \cdot \left(\mathbf{F}^{-1}\right)^{T} \tag{2.53}$$

While $\boldsymbol{\sigma}$ and $\tilde{\boldsymbol{\sigma}}$ are symmetric tensors, $\mathbf{T}^{o}$ is asymmetric tensor [37].

2.3 Governing equations of motion

2.3.1 Eulerian formulation

A given mass of the medium, occupying a volume V, bounded by surface S and acted upon by surface traction **t** and body force **b** per unit mass is shown in Figure 2.6. By applying Newton's second law to a differential mass *dm* with volume dV, we have:

$$\int_{S} \mathbf{t} dS + \int_{V} \rho \mathbf{b} dV = \frac{D}{Dt} \int_{V} \rho \mathbf{v} dV \tag{2.54}$$

Or in rectangular coordinates:

$$\int_S t_i dS + \int_V \rho b_i dV = \frac{D}{Dt} \int_V \rho v_i dV \tag{2.55}$$

Where operator $\frac{D}{Dt}$ denotes material or substantial derivative, $\mathbf{v}$ is the velocity vector and $\mathbf{n}$ is outward unit normal to boundary surface S. The external traction $\mathbf{t}$ can be related to the Cauchy stress tensor $\boldsymbol{\sigma}$ as:

$$t_i = \sigma_{ji} n_j \tag{2.56}$$

By using equation (2.56) the first term of equation (2.55) can be transformed into a volume integral by using the divergence theorem:

$$\int_S t_i dS = \int_S \sigma_{ji} n_j dS = \int_V \frac{\partial \sigma_{ji}}{\partial x_j} dV \tag{2.57}$$

Hence the momentum balance takes the form:

$$\int_V [\frac{\partial \sigma_{ji}}{\partial x_j} + \rho b_i - \frac{D(\rho v_i)}{Dt}] dV = 0 \tag{2.58}$$

Because the volume V is arbitrary, at each point of continuum we have :

$$\frac{\partial \sigma_{ji}}{\partial x_j} + \rho b_i - \frac{D(\rho v_i)}{Dt} = 0 \tag{2.59}$$

Or:

$$\frac{D(\rho v_i)}{Dt} = \frac{\partial \sigma_{ji}}{\partial x_j} + \rho b_i \tag{2.60}$$

Equation (2.60) is called Cauchy's first law of motion. In the case of static equilibrium, as is very common in solid mechanics analysis, the inertia force $\frac{D(\rho v)}{Dt}$ is zero and equation(2.60) reduces to :

$$\frac{\partial \sigma_{ji}}{\partial x_j} + \rho b_i = 0 \tag{2.61}$$

Or:

$$\nabla \cdot \boldsymbol{\sigma} + \mathbf{f} = 0 \tag{2.62}$$

Where $\mathbf{f}$ is body force per unit volume.

2.3.2 Lagrangian formulation

The Lagrangian form of equations of motion derives when initial configuration of body is used as reference configuration. The instantaneous given volume V initially occupied volume V_o bounded by initial surface S_o is considered. By applying the principle of momentum balance for acting forces upon current volume but are measured per initial surface and initial volume, we have:

$$\int_{s_o} \mathbf{N} \cdot \mathbf{T}^o dS_o + \int_{V_o} \rho_o \mathbf{b}_o dV_o = \int_{V_o} \rho_o \frac{d^2\mathbf{x}}{dt^2} dV_o \tag{2.63}$$

Where $\mathbf{N}$ is outward unit normal on initial boundary surface S_o (Figure 2.5) and $\mathbf{T}^o$ is the first Piola-Kirchhoff stress tensor. Transformation of the surface integral to a volume integral by the divergence theorem and the validity of equation for any arbitrary volume V_o, leads to the equation of motion as:

$$\frac{\partial T^o_{ji}}{\partial X_j} + \rho_o b^o_i = \rho_o \frac{d^2 x_i}{dt^2} \tag{2.64}$$

In the static situation the acceleration is zero, then the equilibrium equations are:

$$\frac{\partial T^o_{ji}}{\partial X_j} + \rho_o b^o_i = 0 \tag{2.65}$$

Or:

$$\nabla \cdot \mathbf{T}^o + \mathbf{f}_o = 0 \tag{2.66}$$

2.4 Closure

In the past sections different stress and strain measures were presented. Some of them are defined in terms of initial undeformed configuration and the others are defined in terms of current deformed configuration. Eulerian and Lagrangian equation of motion were also presented. For the GNL analysis (chapter 4) the Lagrangian equation of motion will be used. The second Piola-Kirshhoff and its conjugate strain measure, i.e. Green-Lagrange strain, will be used in the formulation.

In chapter 6, a CFD Eulerian frame-work will be used for both solid and coupled problem analysis. Small strain will be assumed for solid and analysis will be performed for steady state situations. It should be pointed out, equations (2.62) and (2.66) are the same for small strain analysis since no distinction can be made between deformed and undeformed configurations.

Chapter 3

Finite Volume Method

An important step in solving the equations of motion is the discretization technique used to represent space, time and approximate the governing equations. Replacing the continuous field by a finite number of computational points of a numerical grid is the space discretization. Equation discretization involves replacement of individual terms in the governing equations by algebraic expressions connecting nodal values on a finite grid. This transformation of the governing equations into an algebraic system of equations involving the values of the unknowns at the mesh points, is the basis of all numerical methods.

The FVM takes full advantage of an arbitrary mesh, therefore a large number of possibilities are available for the definition of the Control Volumes (CV) used to discretize the domain of interest. Since the spatial variation of dependent variables is unknown, an assumption of their spatial variation should be made. For a discretization method which is numerically convergent [38], the error caused by those assumptions is dependent on the size of the considered volume. By applying a finer grid the result should converge to the exact solution. The accuracy of the numerical solutions, the stability and the rate of convergence of the solution procedure depend on the particular properties of the computational grid. Some desirable properties of the grid are:

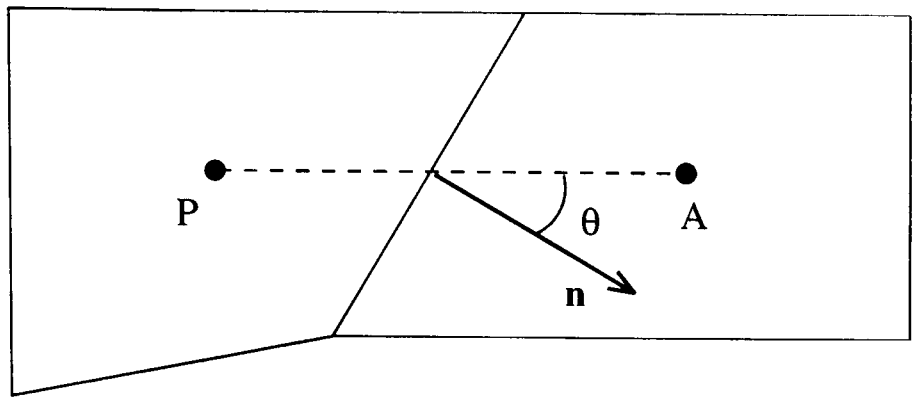

Figure 3.1: Adjacent control volume

- The angle between the line connecting the centre of two adjacent control volumes and normal vector of common face, the angle θ in Figure 3.1, should be as small as possible. Because by approaching to the orthogonal case, diffusive fluxes in the direction normal to the connecting line(PA) reduces and this improves the convergence and stability of the numerical solution.

- The concentration of control volumes should increase in regions where the spatial variation of the dependent variables are higher.

Direct discretization of the integral form of the conservation laws ensures that basic quantities like momentum and energy will remain conserved at the discrete level. For the FVM there is a number of possibilities for the control volume definition on a given structured or unstructured grid. Usually these are divided into the two main categories, called cell centred and cell vertex FVM. In the next section the cell centred CV will be presented then in the section 3.2 the cell vertex CV will be discussed.

3.1 Cell-centred finite volume method

The cell-centred FVM is very popular in CFD applications. In this case the dependent variables, which are averaged values over the control volume, are stored at the centre of CV. This type of CV can be employed on both structured and unstructured meshes which are explained in the following sections.

3.1.1 CFD type cell centred control volume structured mesh

Figure 3.2-a shows a two dimensional cell centred control volume over a structured mesh where the control volume $C_{i,j}$ is designated over mesh cell ABCD. This type of control volume is common in CFD modelling. To avoid the checkerboard problem [3], the same control volume is used for all scalar variables, such as pressure, density, temperature etc., but each velocity component has its own control volume, see Figure 3.2-b. Spalding used this type of cell centred control volume for the simulation of multiphysics problems [32].

3.1.2 CFD type cell centred control volume unstructured mesh

Figure 3.3 shows a two dimensional cell centred control volume over an unstructured mesh where for example, the control volume C_1 is described over the mesh cell AOB. This type of control volume is used in PHYSICA [33] where all dependent variables are collocated at the centre of control volume [39]. The checkerboard problem is avoided by adopting the Rhie-Chow [40] interpolation technique. The work presented in chapter 6 is based on using this type of control volume.

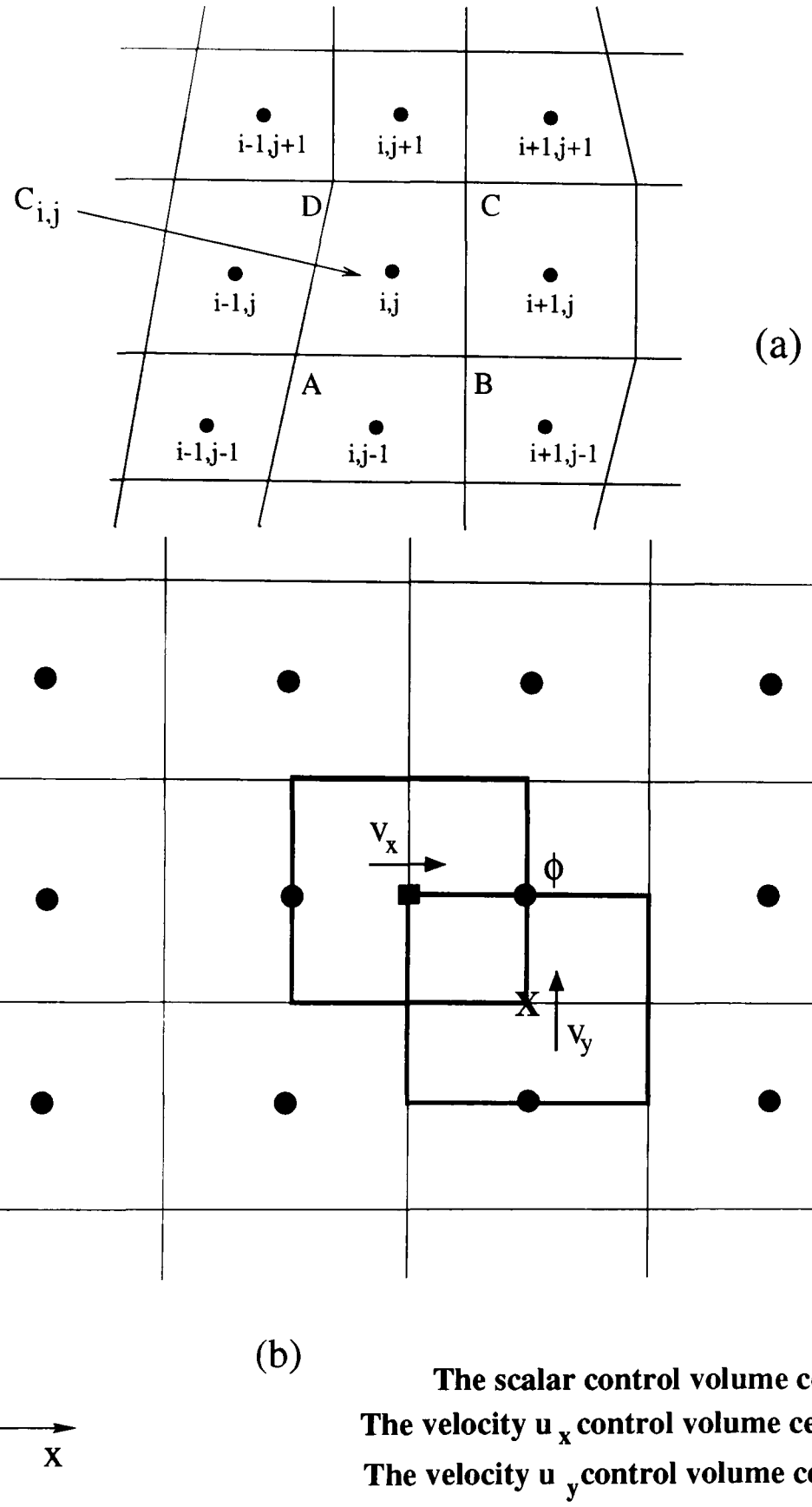

Figure 3.2: Two dimensional cell centred control volume: (a) Control volume over structured mesh; (b) Staggered control volumes .

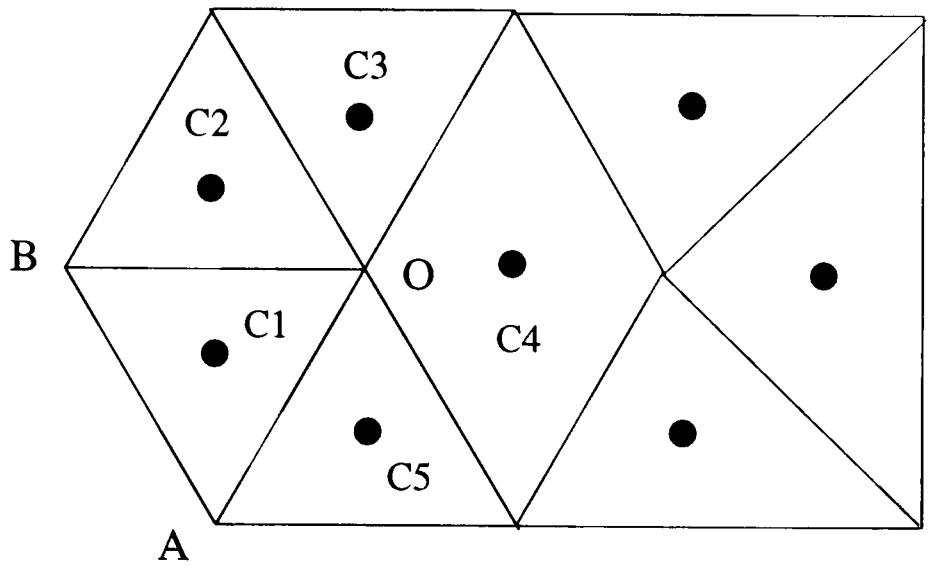

Figure 3.3: Two dimensional cell centred control volume over unstructured mesh

3.1.3 Cell centred control volume for structural analysis, structured mesh

Demirdzic *et al.* [6] used this type of control volume for thermo-elastic-plastic stress analysis. The solution domain is divided into a finite number of contiguous control volumes and all dependent variables, i.e. displacement components and temperature, are stored at the centre of control volumes. For the specification of boundary conditions, boundary nodes are considered at the centre of boundary cell-faces, see Figure 3.4-a. The variation of dependent variables is assumed linear between the centre of neighbouring cells. The central difference scheme, which is second order accurate on uniform grid, is used to express the cell-face fluxes of dependent variables in terms of the neighbouring cell values.

Boundary conditions can be incorporated by including the known values of traction or displacements into the equilibrium equations of cells that have faces lying on the boundary. Boundary conditions can be either of Dirichlet type (displacement boundary condition) or Neumann type (traction boundary condition). In the case of Dirichlet boundary conditions, Figures 3.4-b and 3.4-c, the displacement components or temperature at node B in the discretized governing equations are replaced

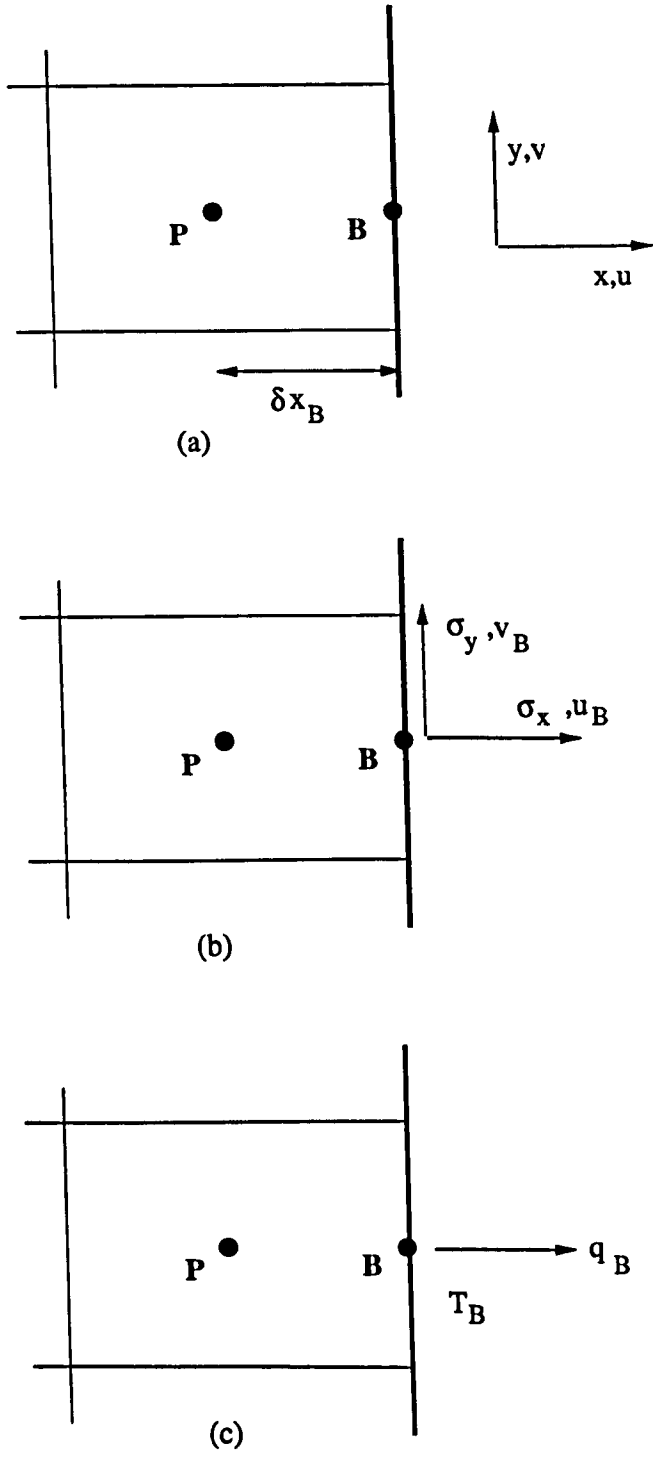

Figure 3.4: (a) Control volume with face on the boundary; (b) Displacement or traction boundary condition; (c) Temperature or heat flux boundary condition

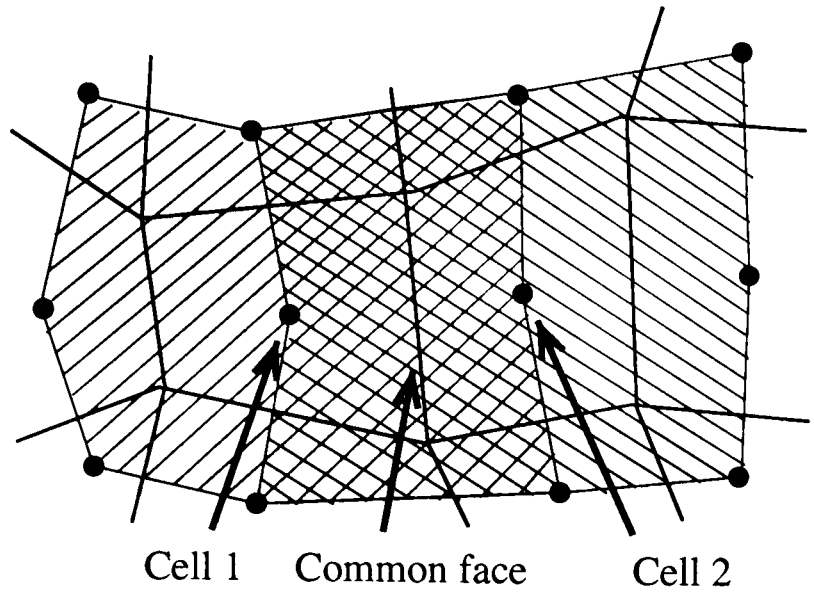

Figure 3.5: Region in which displacement is assumed to vary linearly.

directly with the u_B, v_B or T_B and in case of Neumann boundary condition, Figures 3.4-b and 3.4-c. the induced traction or heat flux on the boundary cell-face is used in equations which express the equilibrium equations of cell, P. In this case, due to the need of the displacement components at **B**, it is obtained by linear extrapolation from the interior of the solution domain.

3.1.4 Cell centred control volume for structural analysis, unstructured mesh

The unstructured cell centred control volume is also used in the solid stress analysis. Demirdzic *et al.* [7, 31, 41] and Ivankovic *et al.* [8, 42, 43, 44] used this control volume in their work for modelling of structures with complex geometries. As indicated in reference [41] a linear displacement distribution function, which is second order accurate, is assumed across a cell and its surrounding neighbours, see Figure 3.5. For solid mechanics problems, they calculated strains on the common face of two adjacent cells by averaging derivatives of the overlapping displacement distributions of the two cells. Mathematically it can be expressed as:

$$\psi_j = \frac{1}{2}(\psi_{P_o} + \psi_{P_j}) + \frac{1}{2}[(grad\psi)_{P_o} \cdot (\mathbf{r}_j - \mathbf{r}_{P_o}) + (grad\psi)_{P_j} \cdot (\mathbf{r}_j - \mathbf{r}_{P_j})] \qquad (3.1)$$

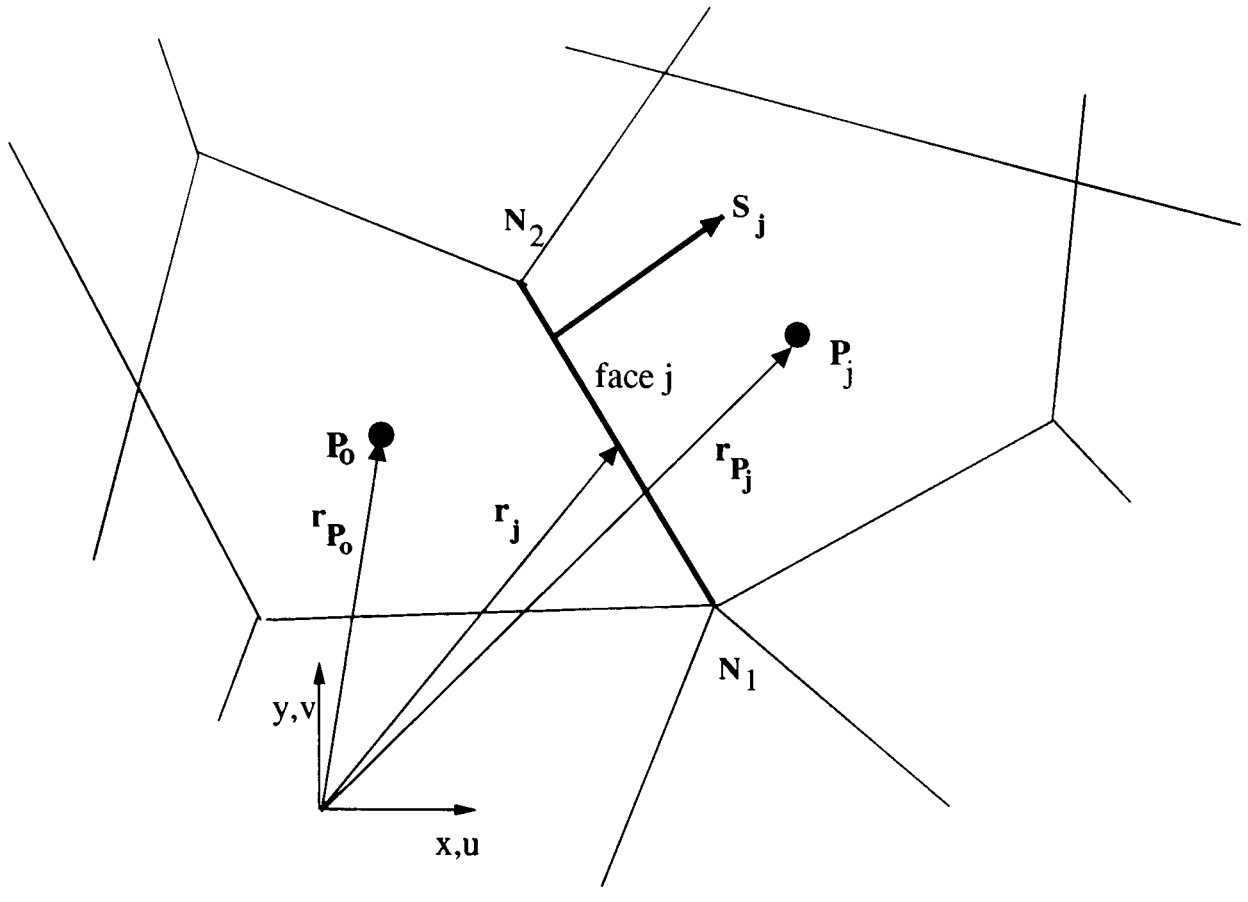

Figure 3.6: A two dimensional control volume and the notation used.

Where ψ_j stands for dependent variables or their gradient at the cell-face centre and $\mathbf{r}_j$ is the position vector of the cell-face centre, see Figure 3.6. The gradient vector at a given control volume centre is approximated by ensuring a fit to a set of sampling points consisting of centre of nearest neighbours of given control volume as:

$$\psi_{P_j} = \psi_{P_o} + grad\psi_{P_o} \cdot \mathbf{d}_j \qquad (j = 1, ..., n) \tag{3.2}$$

Where $\mathbf{d}_j = \mathbf{r}_{P_j} - \mathbf{r}_{P_o}$. By using the least square method equation (3.2) can be solved as:

$$grad\psi_{P_o} = D^{-1} f \tag{3.3}$$

Where:

$$D = \sum_{j=1}^{n} \mathbf{d}_j^T \mathbf{d}_j \qquad \text{and} \qquad f = \sum_{j=1}^{n} \mathbf{d}_j^T (\psi_{P_j} - \psi_{P_o}) \tag{3.4}$$

Wheel [45, 46] also used unstructured cell centred control volume in solid mechanics analysis. In this approach the variation of displacement was assumed linear across each cell face, see Figure 3.7. The strain on typical face j in Figure 3.8-a, is

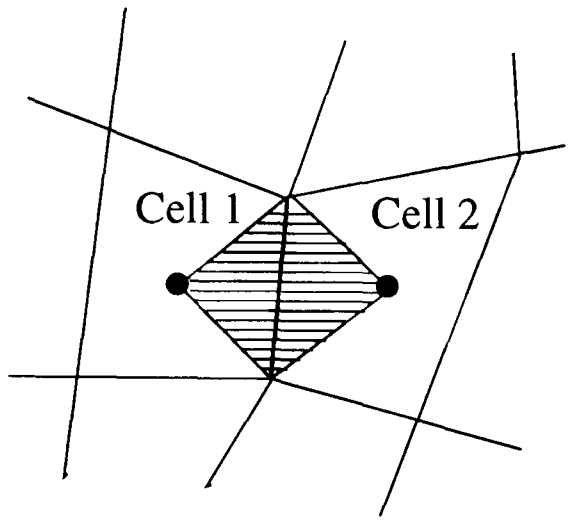

Figure 3.7: Region in which displacement is assumed to vary linearly.

approximated as:

$$(\frac{\partial u}{\partial x})_j = \frac{u_{P_j} - u_{P_o}}{d_j} \frac{\cos \alpha_j}{\cos (\alpha_j - \beta_j)} - \frac{u_{N2} - u_{N1}}{S_j} \frac{\sin \beta_j}{\cos (\alpha_j - \beta_j)} \tag{3.5}$$

In equation (3.5) the displacement at vertices should be defined. For a given vertex, a linear distribution of displacement throughout the region surrounding the given vertex and centre of cells that meet at that vertex was assumed. Consequently the vertex displacements in equation (3.5) can be eliminated and represented by a combination of the central displacements of the surrounding cells.

For representing the boundary conditions, boundary nodes are considered at the centre of boundary cell-faces, see Figure 3.8-b. But instead of introducing the boundary conditions directly into the equations associated with the cells which have faces on the boundary he adopted an approach which employs special line cell on boundary nodes, cell **B** in Figure 3.8-b. This approach introduces additional degrees of freedom into the analysis, but automatic calculation of displacement at the boundary nodes, on edge which external traction are applied, through the solution procedure can be considered to have positive effect. When displacement is applied to the boundary, Figure 3.8-b, the displacement at **B** in the global coordinate axes, u_B

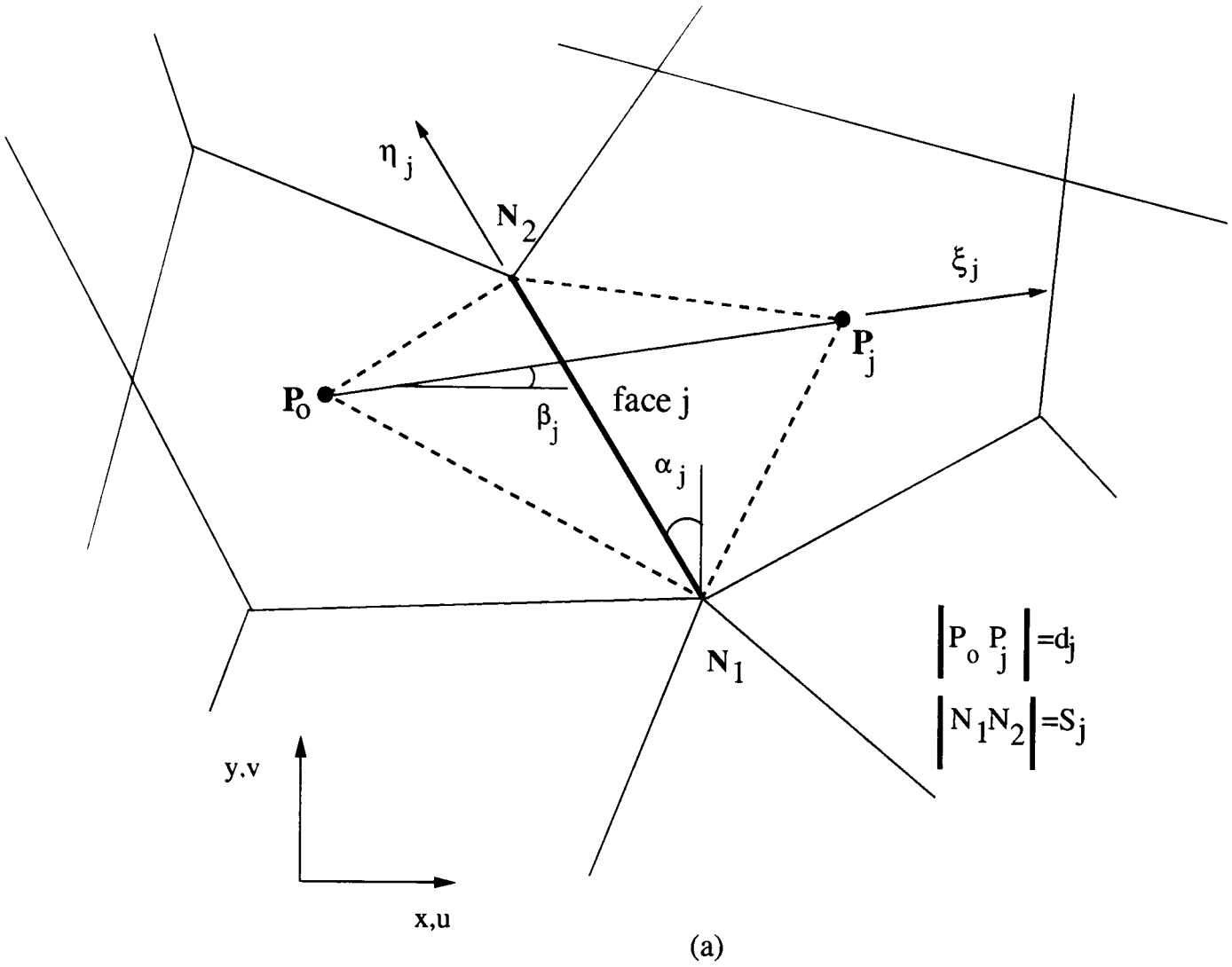

(a)

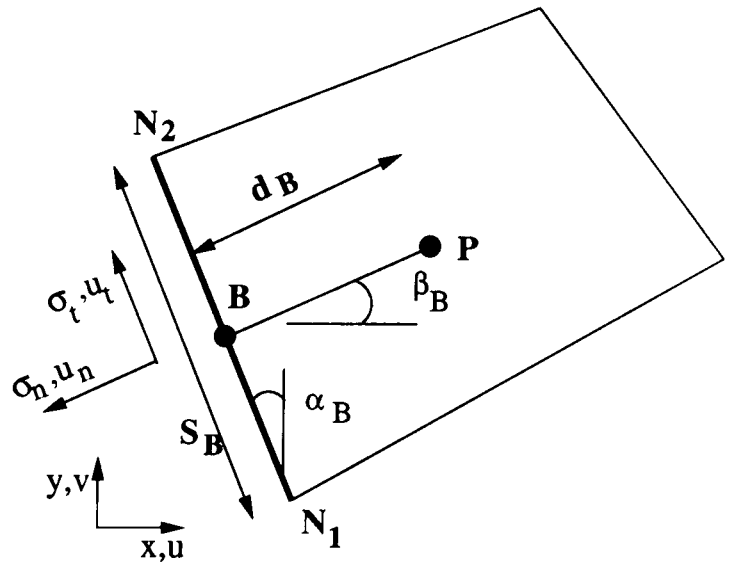

(b)

Figure 3.8: (a) A typical internal control volume; (b) A typical control volume with face on the boundary.

and v_B, can be given as:

$$u_B = -u_t \sin\alpha_B - u_n \cos\alpha_B \tag{3.6}$$

$$v_B = u_t \cos\alpha_B - u_n \sin\alpha_B \tag{3.7}$$

When traction is applied to the boundary, Figure 3.8-b, we also need to construct two additional equations for u_B and v_B. The stress components at **B** in the global coordinate axes can be related to the normal and tangential components of applied traction as:

$$\sigma_n = \sigma_{xxB} \cos^2\alpha_B + \sigma_{yyB} \sin^2\alpha_B + 2\sigma_{xyB} \sin\alpha_B \cos\alpha_B \tag{3.8}$$

$$\sigma_t = -\sigma_{xxB} \sin\alpha_B \cos\alpha_B + \sigma_{yyB} \sin\alpha_B \cos\alpha_B + \sigma_{xyB}(\cos^2\alpha_B - sin^2\alpha_B) \tag{3.9}$$

By using the constitutive equations and approximations for the displacement derivatives, the stress components in equations (3.8) and (3.9) are represented in terms of central displacements of the internal cells and line boundary cell of **B**. However, in case of displacement boundary condition, equations (3.6) and (3.7), and in case of traction boundary condition, equations (3.8) and (3.9) form two equations corresponding to each typical line boundary cell of **B** which conforms to the general pattern of equations of the internal cells. When mixed boundary conditions are applied then a proper selection of equations (3.6)-(3.9) must be chosen.

This approach was applied for the two and three dimensional analysis [46] and also applied for the small and large strain incompressible solid stress analysis [47, 13].

3.2 Control Volume-Unstructured Mesh(CV-UM) vertex based finite volume method

In this approach a non-overlapping CV is overlaid on the mesh of the solution domain. The CV is formed about each of the vertices (or nodes) by connecting the

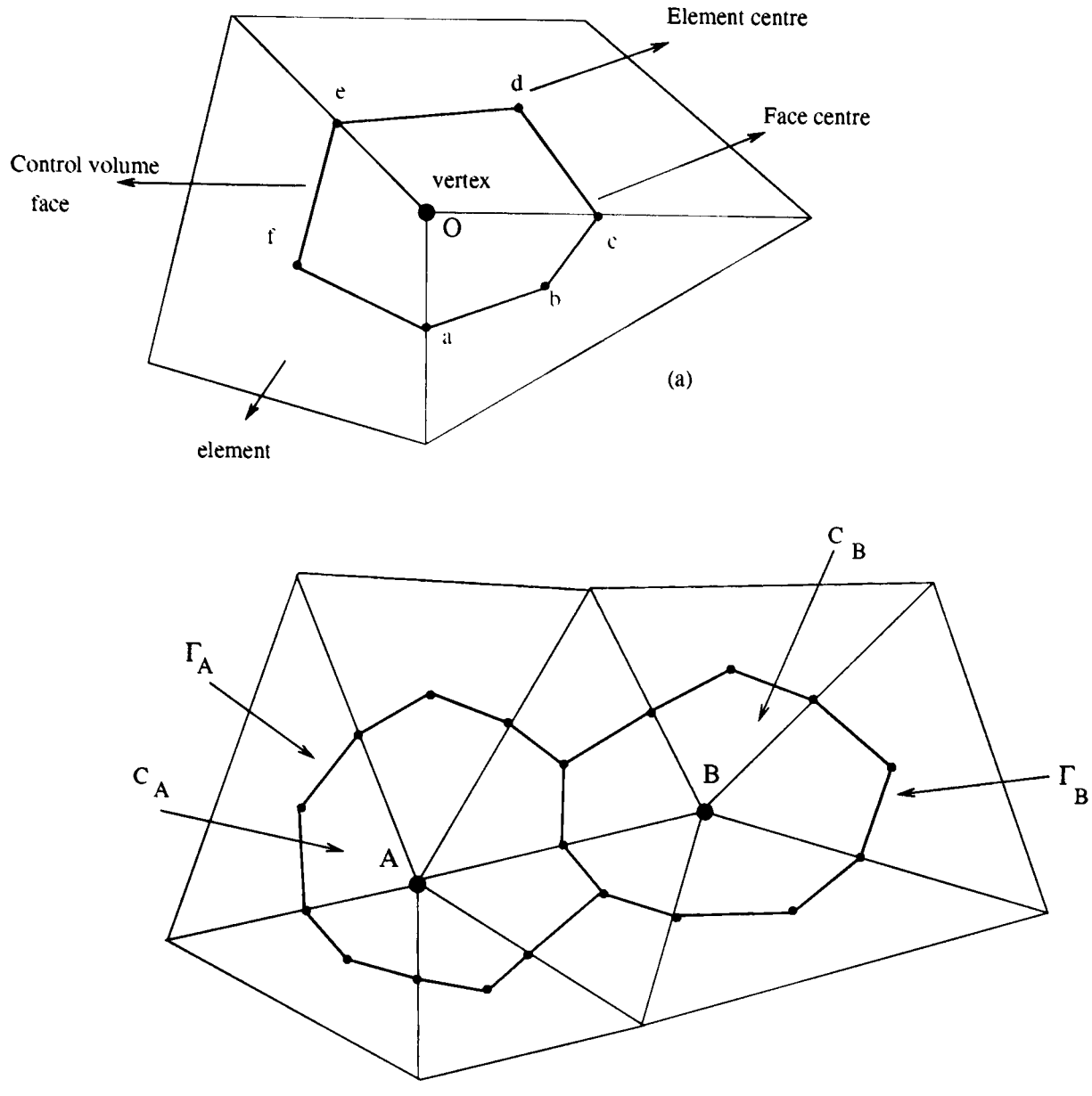

Figure 3.9: (a) CV-UM vertex based control volume; (b) non-overlapping control volume

midpoints of the mesh cell faces and the centres of the mesh cells. Shape functions are used to describe the variation of a variable within an element. The solution domain can be discretized by any element type for which its shape function exist. Figure 3.9 illustrates a two dimensional mesh where control volumes are constructed on it. The complete control volume over which the conservation principle is applied is the polygon *abcdef* (Figure 3.9-a). This type of CV has also been named as cell centred [48], node-centred [49], and control volume based-finite element method [39]. This method of construction of the control volume is general and applicable to two and three dimensional structured or unstructured mesh. This type of CV was used

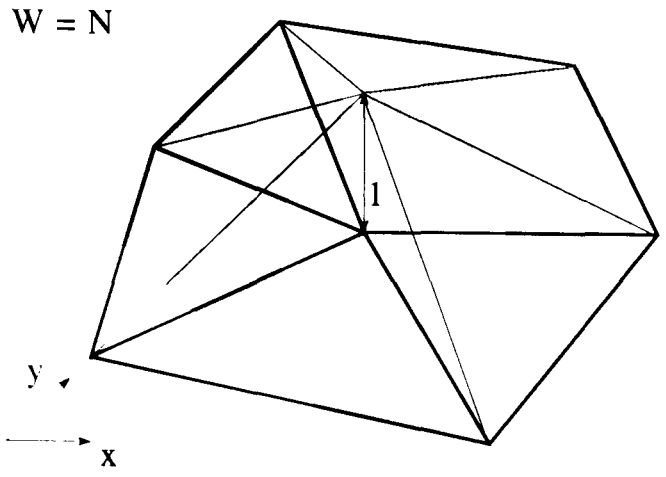

(a)

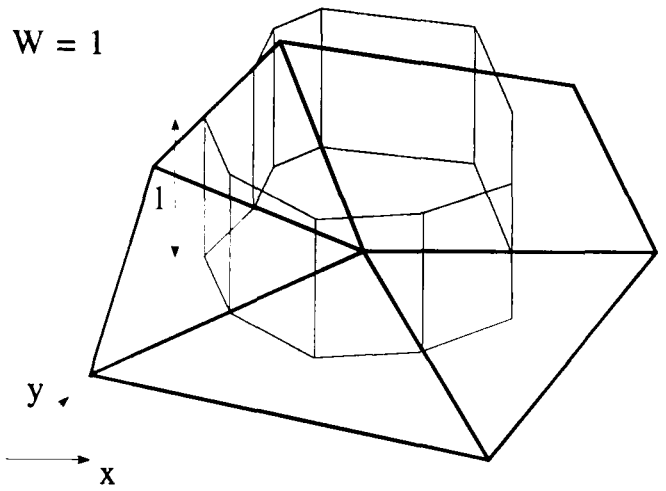

(b)

Figure 3.10: Weighting function W: (a) Bubnov-Galerkin FEM; (b) CV-UM vertex based FVM.

by Winslow [50] to solve magneto-static problems. The method was also applied to the solution of hydrodynamic and heat transfer problems [51], aerodynamics [52] and solidification [53].

As will be discussed later in chapter 4, the main fundamental difference between the FVM and Bubnov-Galerkin FEM is the associated weighting function W. The weighting functions for CV-UM vertex based FVM and Bubnov-Galerkin FEM are illustrated in Figure 3.10. The results presented by Oñate *et al.* [48] indicate the FVM based on the CV-UM control volume, provides naturally diagonally dominant matrices. Also, the complete equivalence of the CV-UM based FVM and

the Bubnov-Galerkin FEM for one dimensional problems and also for two dimensional problems discretized by Constant Strain Triangular(CST) elements in static elastic analysis have been indicated. Fryer *et al.* [2, 54] have compared the Bubnov-Galerkin FEM and CV-UM based FVM for a number of standard two dimensional linear elastic problems consisting of 4-noded Bilinear Quadrilateral(BLQ) elements. Bailey and Cross [55] have extended this work to three dimensional using 8-noded Trilinear Hexahedral(TLH) elements.

Since the research in this thesis provides developments of the finite volume method based on the CV-UM control volume, the following sections present more details of the spatial discretization in two and three dimensional analysis.

3.3 Space discretization based on the CV-UM finite volume method

As mentioned in section (3.2) the solution domain is discretized over non-overlapping CV's which are overlaid on the finite element mesh. Similar to Bubnov-Galerkin method, shape functions are used to describe the variation of any dependent variables over an element. As in the finite element context, it is computationally convenient to use reference elements for the derivation of the discretized equations. These reference elements represent the mesh elements in a local coordinate systems regardless of how distorted any element may be in terms of global coordinates. The mapping from local coordinates to global coordinates is performed via shape functions using the standard FE techniques [56]. By applying isoparametric elements the shape functions utilized for both coordinate transformation and variable approximation.

In FEM the governing equations involve the volume integral where they are ap-

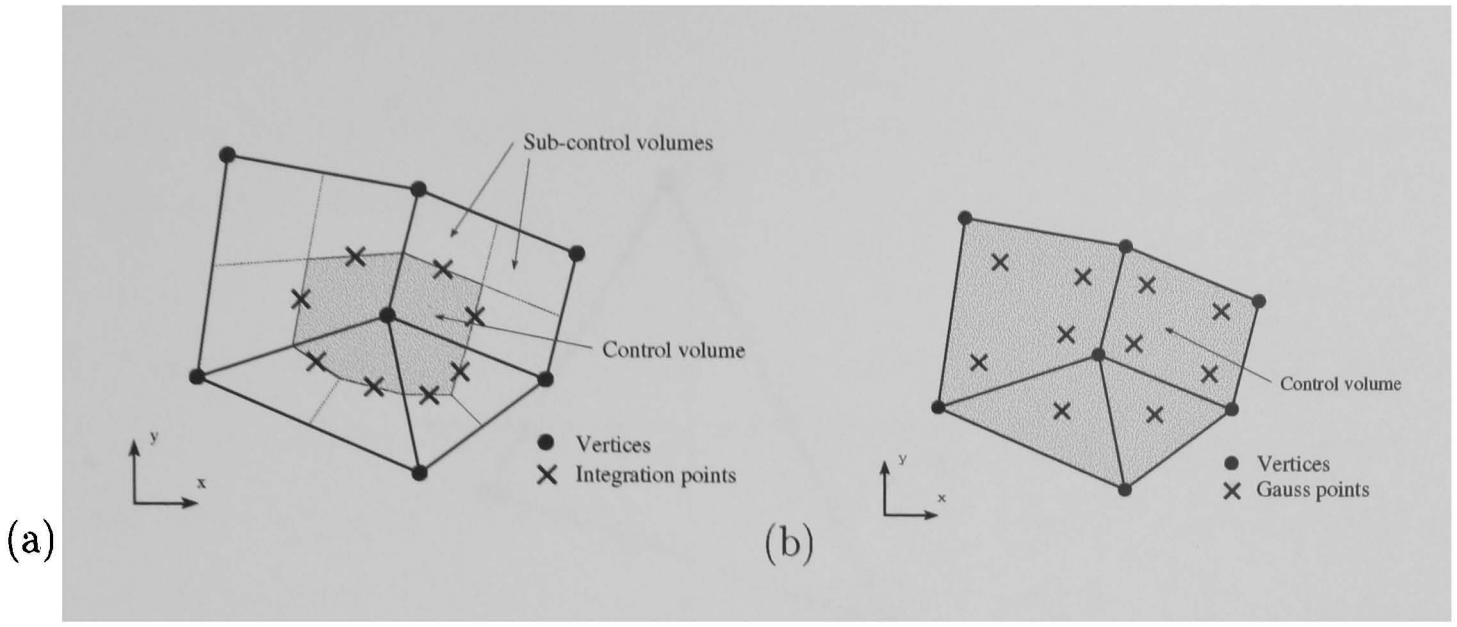

Figure 3.11: Two dimensional integration points: (a) FVM; (b) FEM.

proximated by using Gauss quadrature [35] technique to evaluate the variables at Gauss points of the elements. In the FVM the governing equations involve surface integrals which are evaluated by midpoint technique at integration points. Figure 3.11 illustrates the Gauss points and integration points associated with the elemental contributions in two dimensional analysis for the FEM and FVM respectively. In this work for the two dimensional analysis the CST and BLQ elements, for the three dimensional analysis the TLH (brick) elements were used for space discretization in both FEM and FVM. These elements are introduced in more detail in the next sections.

3.3.1 Two dimensional finite volume discretization

The CST and BLQ elements in local coordinates are illustrated for both of the FEM and the FVM in Figures 3.12 and 3.13. Both are representatives of an arbitrary deformed CST and BLQ element in global coordinates. For CST element, in the FEM case the element involves one Gauss point while in the FVM case three integration points are associated with each element. However,because of constant strain assumption within each individual CST element, approximation of integrals in the governing equations corresponding to an element can be performed at the centre of element rather than the three different integration points. With regard to

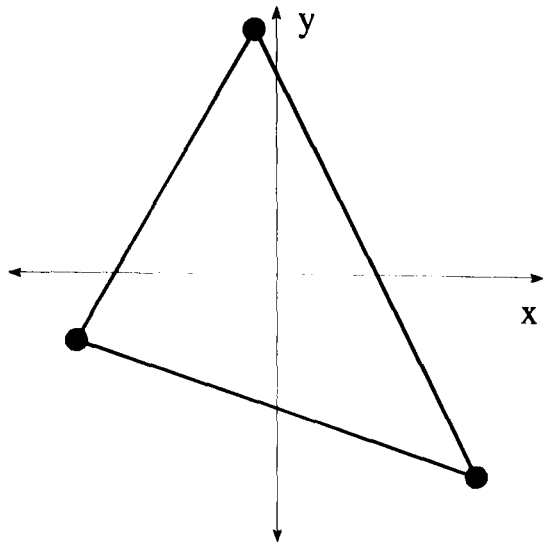

(a)

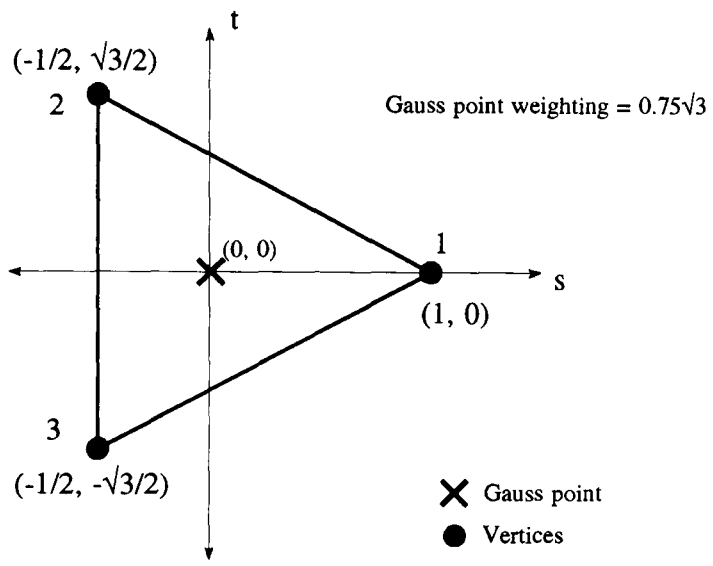

(b)

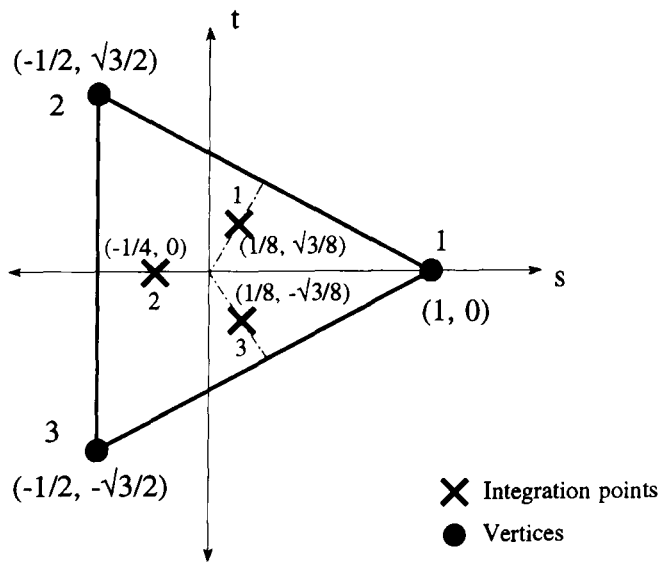

(c)

Figure 3.12: CST element: (a) Global coordinates; (b) FEM local coordinates; (c) FVM local coordinates.

this point in both FEM and FVM one integration point is enough at the element centre for a CST element.

It has been shown by Oñate [48] that, in small deformation cases, for the linear elastic problems involving CST elements the element stiffness matrix coincide exactly for the FEM and FVM cases. Further more for problems involving material nonlinearity which are discretized with CST elements, it is shown by Taylor [57] that the internal force terms generated by the visco-plastic strains are identical for both FEM and FVM. More studies about this coincidence for the geometrically nonlinear problems will be presented in chapter four of this thesis.

The BLQ element in local coordinates is illustrated for both FEM and FVM in Figure 3.13. The associated element in global coordinates is illustrated in Figure 3.13-a. For the FEM analysis the BLQ element involves four Gauss points and similarly for the FVM case it also involves four integration points. While the element stiffness matrix in FEM case for the BLQ element is always symmetric, in FVM case it is asymmetric for the nonorthogonal mesh.

3.3.2 Three dimensional finite volume discretization

The TLH elements were used for the three dimensional analysis in this research. The global to local mapping of the elements again allows an arbitrary deformed TLH element to be treated identically in computational terms for both FEM and FVM cases. The construction of three dimensional sub-control volumes for the FVM is a relatively straight forward extension of the two dimensional approach. In the three dimensional approach the control volumes are formed by surfaces passing the elemental centroid and the centre of face of the mesh elements. Figure 3.14 shows this approach for the eight arbitrary elements contributing to a vertex based control volume. The location of the Gauss points for the FEM and the integration points

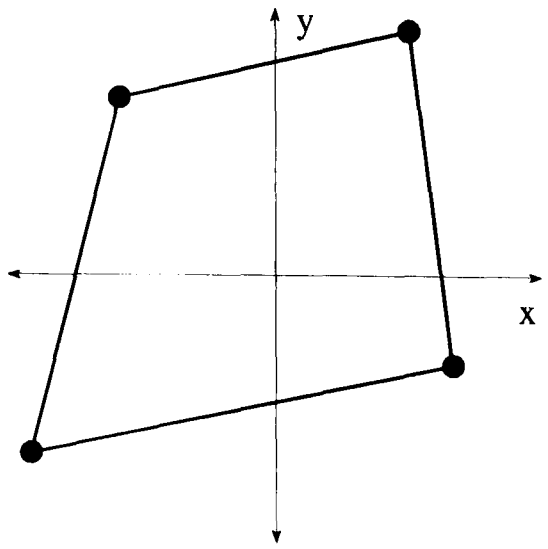

(a)

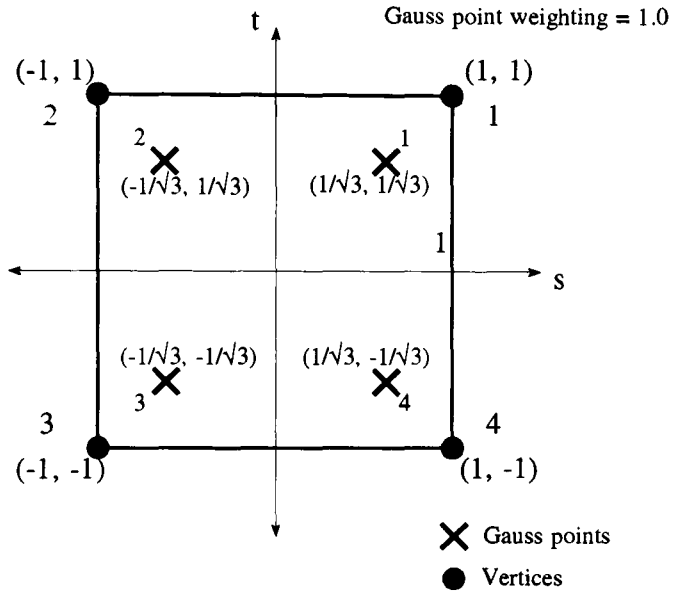

(b)

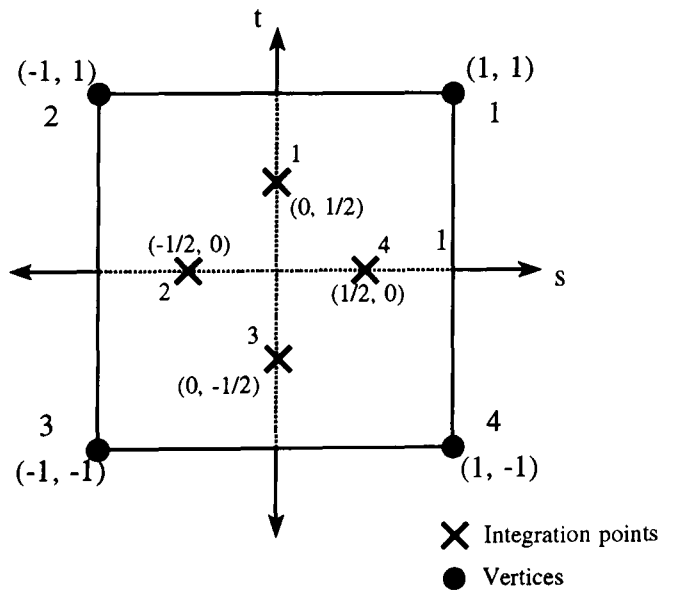

(c)

Figure 3.13: BLQ element: (a) Global coordinates; (b) FEM local coordinates; (c) FVM local coordinates.

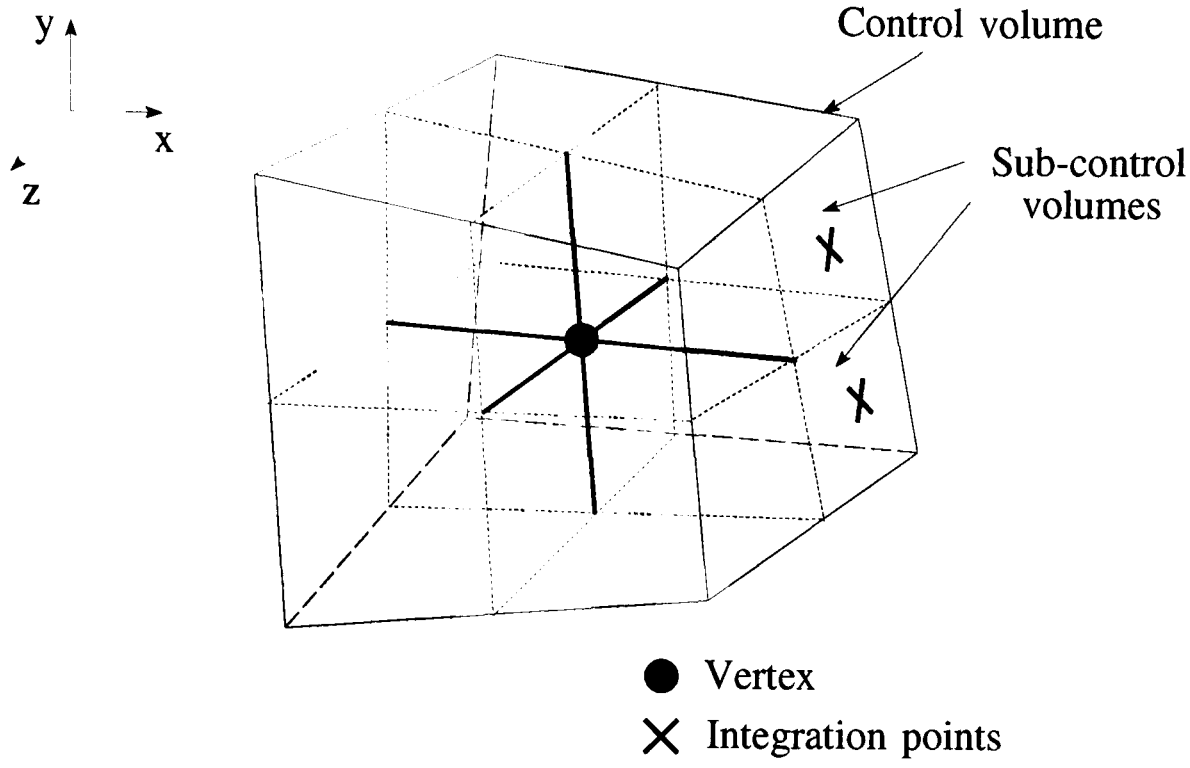

Figure 3.14: Three dimensional vertex based control volume.

for the FVM are different. For the FEM analysis the TLH element involves eight Gauss points and for the FVM analysis twelve integration points are within an element. Figure 3.15 and Figure 3.16 shows Gauss point locations and integration point locations respectively. The elemental stiffness matrix of the TLH element for the FEM is symmetric while for the FVM is unsymmetric in the nonorthogonal mesh elements.

3.4 Closure

In this chapter attempts have been made to explain the different formats of the finite volume methodology in computational mechanics. It is of interest to investigate the aspects of the different type of finite volume techniques for solid mechanics problems. Thus, in chapter 4 and 5, the CV-UM cell vertex based control volume will be used and in chapter 6, potential of a cell centred finite volume based CFD code for analysis of coupled problems will be investigated.

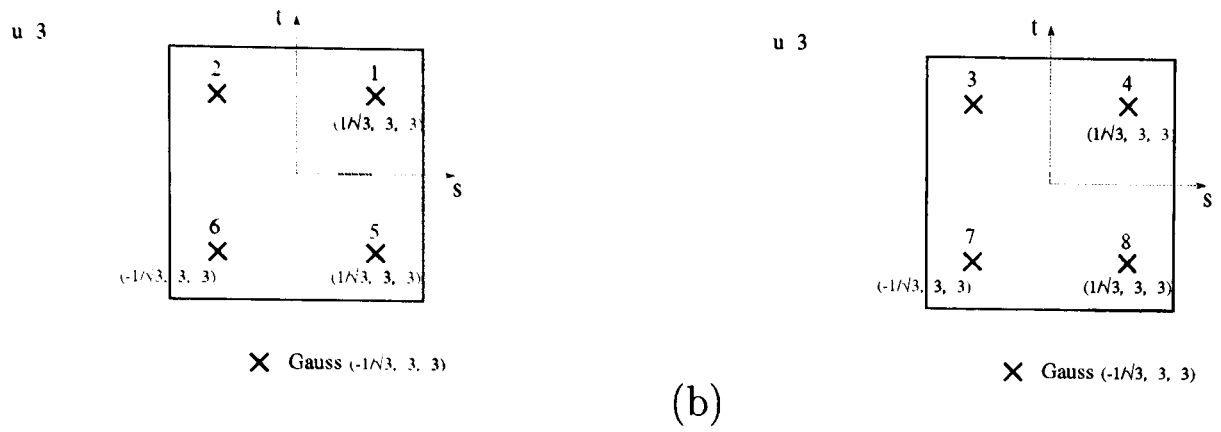

Figure 3.15: TLH element's Gauss points in local coordinates: (a) $u = 1/\sqrt{3}$; (b) $u = -1/\sqrt{3}$.

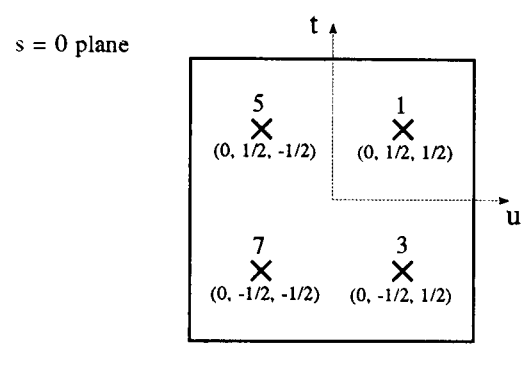

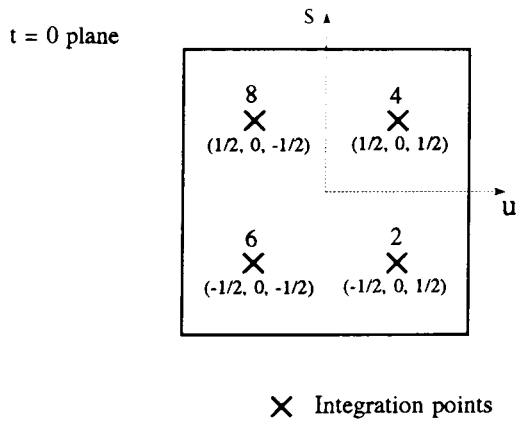

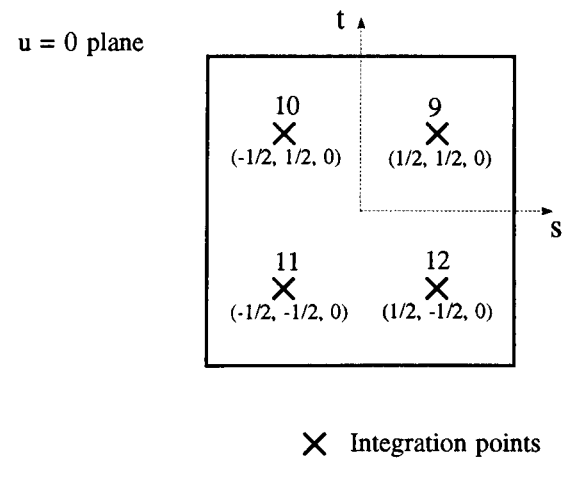

Figure 3.16: TLH element's integration points in local coordinates: (a) u plane;(b) s plane;(c) t plane.

Chapter 4

Vertex Based Finite Volume Discretization for Geometrically Nonlinear Problems

Although FVM for CSM problems began ten years ago, there was no publication on the geometrically nonlinear problem analysis by the FVM until recently when Fallah *et al.* [14, 15], Maneeratana *et al.* [12] and Wenke *et al.* [13] presented the FVM application for analysis of GNL problems. In this chapter a full description of the three dimensional vertex based finite volume procedure for the analysis of GNL problems is presented. In the first section the GNL problem is explained and categorised where the material behaviour is assumed linear elastic. In section two, the cell vertex based FV procedure for GNL formulation is presented. During the formulation the similarity and differences of FV method and Bubnov-Galerkin FE method are shown. As a result, the FV method can be considered as a particular form of weighted residual method with a unit weighting function, where in the FE Bubnov-Galerkin method the shape functions are the weighting function. The stiffness matrix of the FV method is developed and then the solution procedure is explained. A fortran code has been developed based on the finite volume cell ver-

tex formulation. The formulation is tested on a number of geometrically nonlinear problems. In comparison with FE, the results reveal that FV can reach the FE results with a higher mesh density. The following novel contributions are made in this chapter:

- Novel three dimensional vertex based finite volume formulation for GNL analysis.
- Comparison of the FV and the FE results in terms of accuracy and CPU time.

4.1 Types of GNL analysis

4.1.1 Large displacement, large rotation, small strain analysis

The following examples illustrate this type of behaviour. Consider a cantilever rigid link with linear elastic torsion spring as part of end support as shown in Figure 4.1. The equilibrium state is satisfied when :

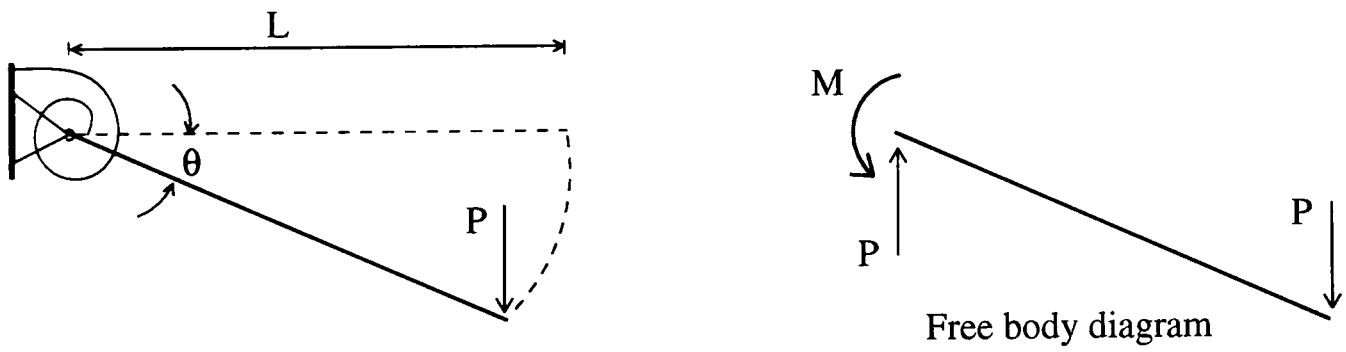

Figure 4.1: Large displacement, large rotation, small strain behaviour

$$PL\cos\theta = M \tag{4.1}$$

Where the moment, M, can be related to rotation, θ, as:

$$M = K\theta \tag{4.2}$$

Where K is the torsional stiffness of the spring.

Substituting equation (4.2) into equation (4.1) gives:

$$P = \frac{K\theta}{L\cos\theta} \tag{4.3}$$

This equation clearly shows the nonlinear relation between response θ and applied load P. Obvious when the rotation is small, $\cos\theta$ can be replaced by one so $P = \frac{K\theta}{L}$; this shows linear relation between load P and rotation θ. Figure 4.2 shows the linear and nonlinear relation between load P and rotation θ. frame undergoes large rigid body displacements and rotations.

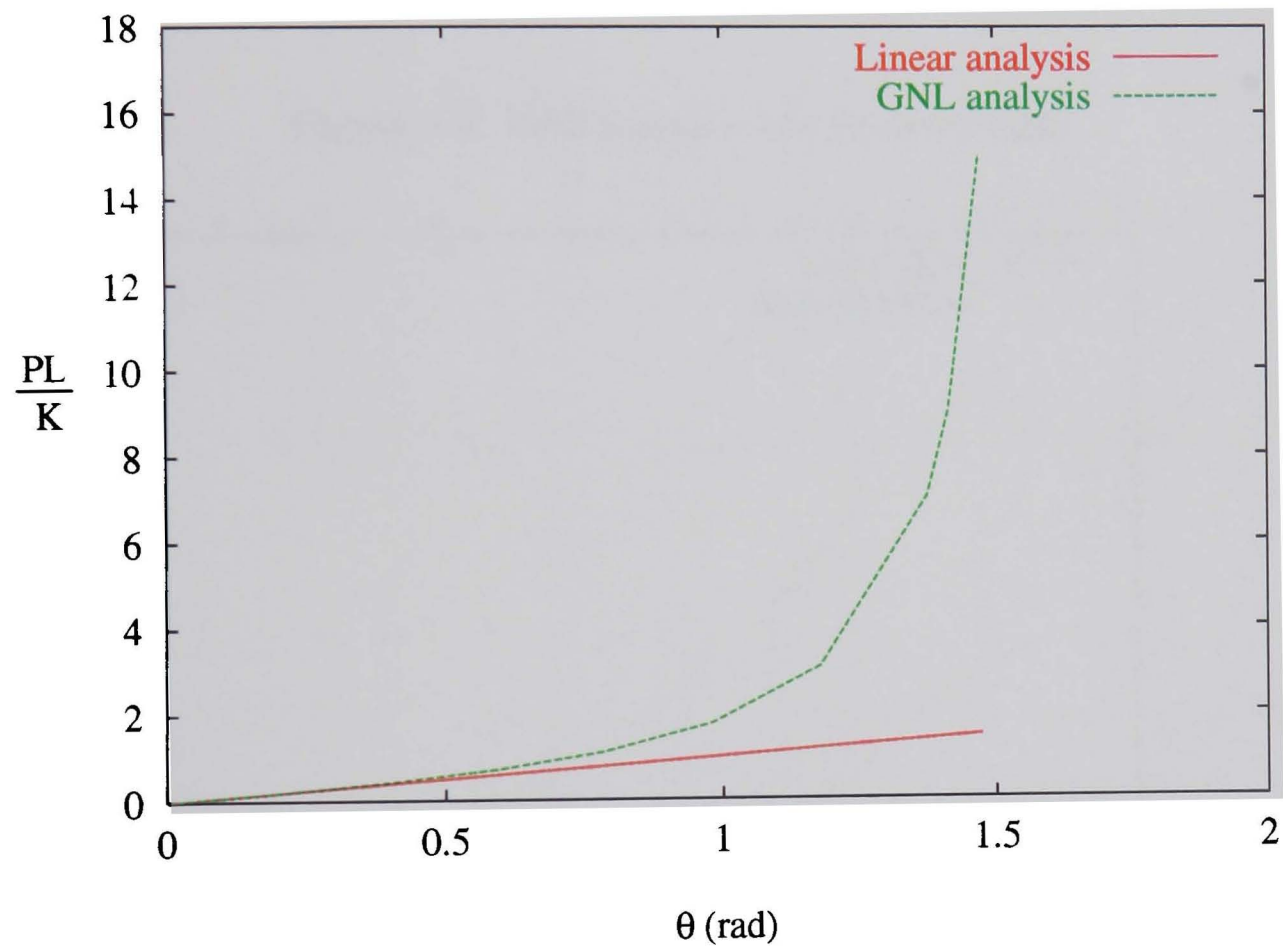

Figure 4.2: Linear and nonlinear relation between load and rotation

4.1.2 Large displacement, small rotation, small strain analysis

Analysis of a tensioned cable is an example of this category, see Figure 4.3. The

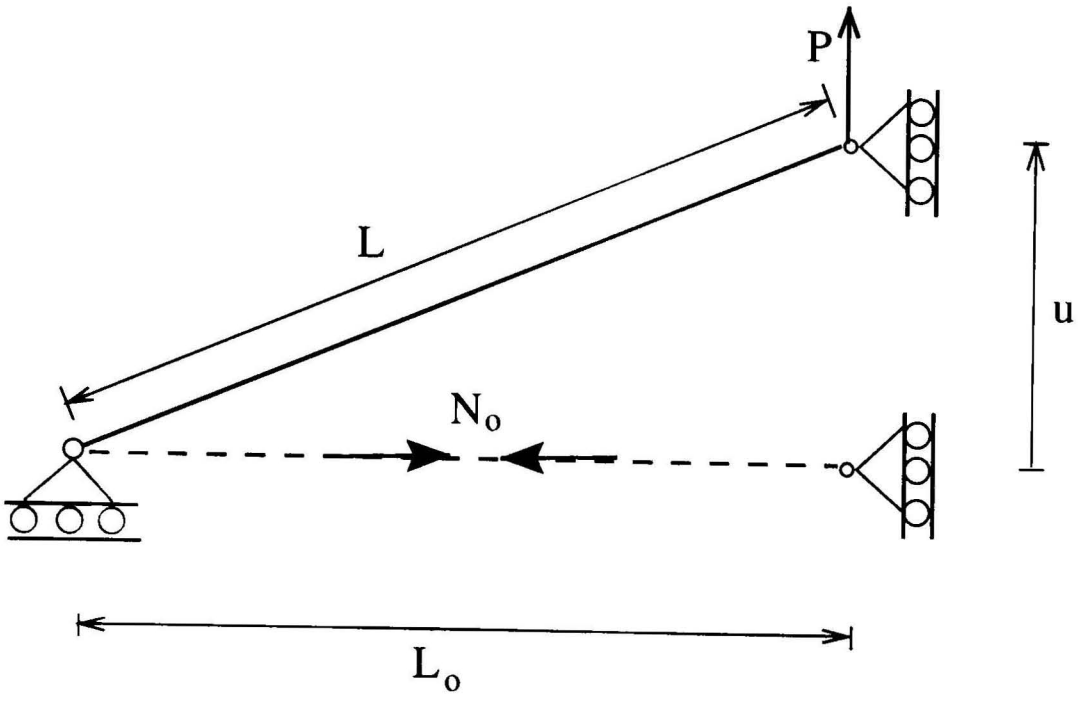

Figure 4.3: GNL behaviour of a tensioned cable

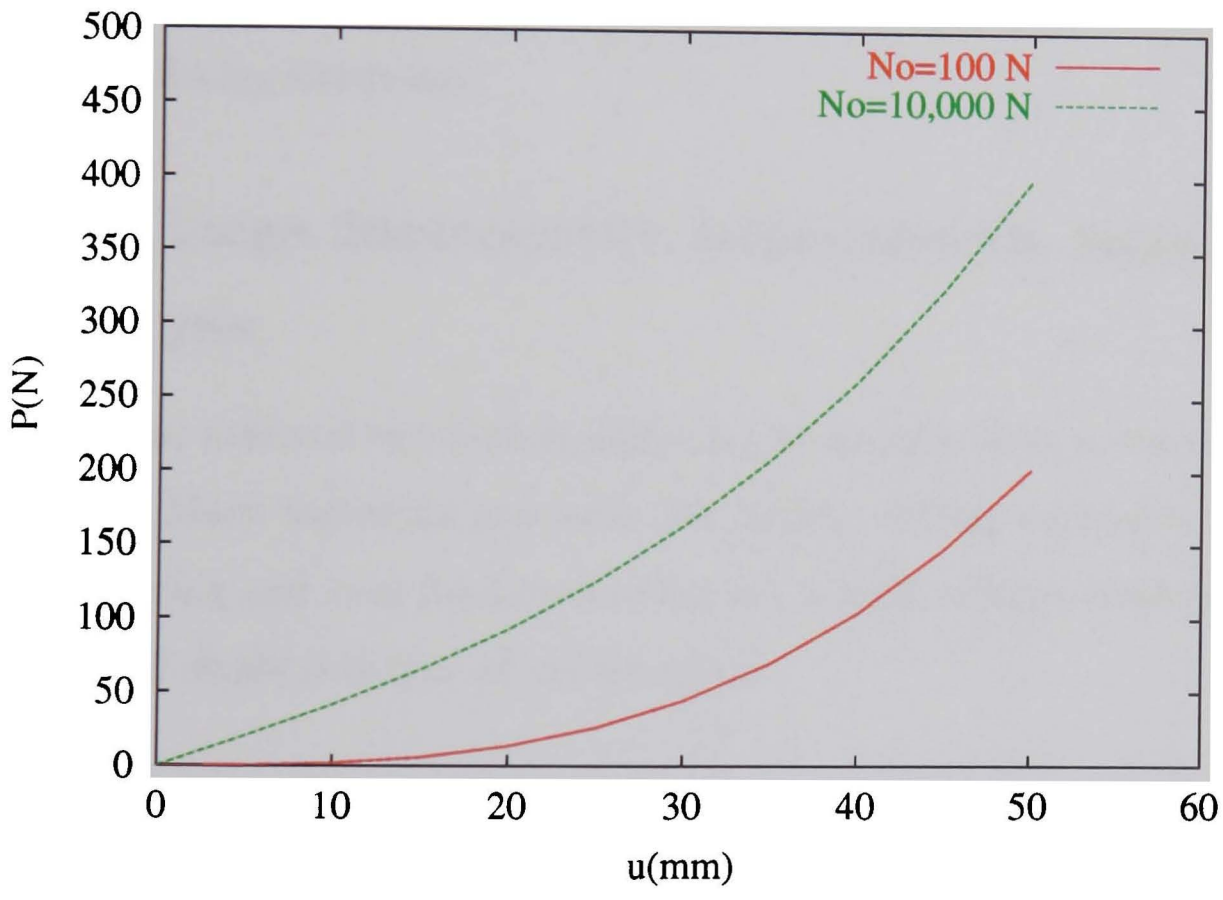

Figure 4.4: Load displacement characteristic of a cable

Cable in position u=0 is under the tension force N_o. Small Strain behaviour is assumed, which means the cross sectional area of the cable, A, remains nearly constant

and $\frac{L}{L_o} \approx 1$. Relation between load P and displacement u can be presented as [37]:

$$P = \frac{EA}{2L_o^3}u^3 + N_o\frac{u}{L_o} \tag{4.4}$$

Figure 4.4 shows the load-displacement $(p-u)$ relation for this case where:

$$N_o = 10^2 N \quad \text{and} \quad 10^4 N \quad , \quad A = 0.25mm^2$$

$$E = 2.0 \times 10^8 \frac{N}{mm^2} \quad , \quad L_o = 2500mm$$

The rotation in this problem is small enough because, for example, for u=50 mm (200 times the cable thickness):

$$\tan\theta = \frac{50}{2500} = 0.02 \longrightarrow \theta = 1.15^o$$

It can be seen in Figure 4.4, by increasing the initial tension force, N_o, the cable shows stiffening behaviour.

4.1.3 Large displacement, large rotation, large strain analysis

In this case material experiences large strains and this adds to the complexity of the problem. Many industrial processes like forging, rolling, extrusion, stretch forming, deep drawing and even food production get benefit of large strain phenomena. Figure 4.5 shows this type of deformation.

4.2 Three dimensional formulation for GNL analysis

4.2.1 Reference Frame for large deformation analysis

In this chapter the Total Lagrangian description is employed. A material particle which occupies position $\mathbf{X}$ in the undeformed state (Figure 4.6) is identified in the

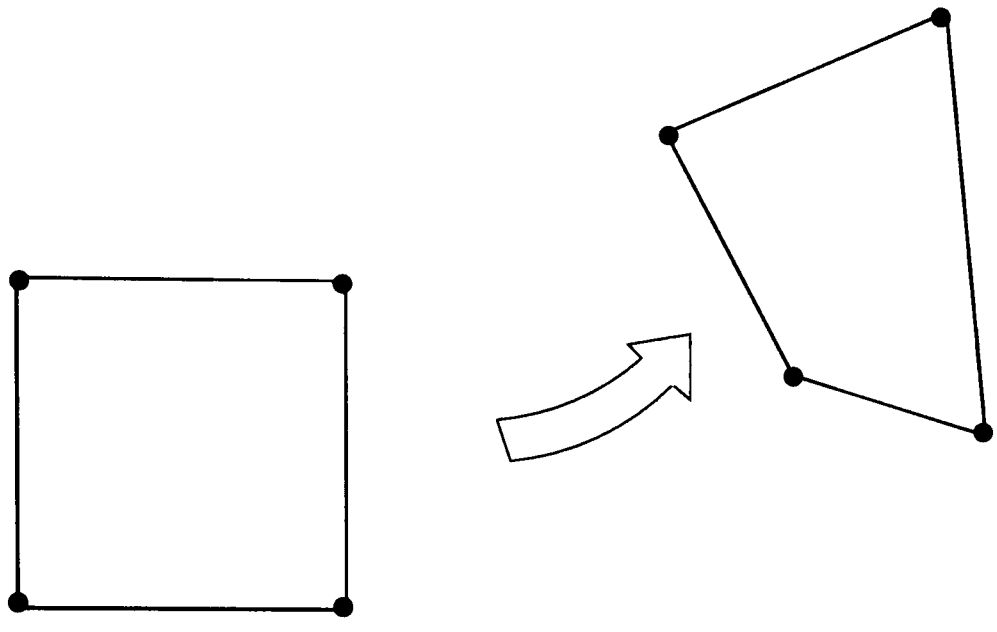

Figure 4.5: Large displacement, large rotation and large strain

cartesian co-ordinates as:

$$\mathbf{X} = \begin{bmatrix} X \\ Y \\ Z \end{bmatrix} \tag{4.5}$$

Suppose that this particle is displaced to position $\mathbf{x}$ during the deformation. Dis-

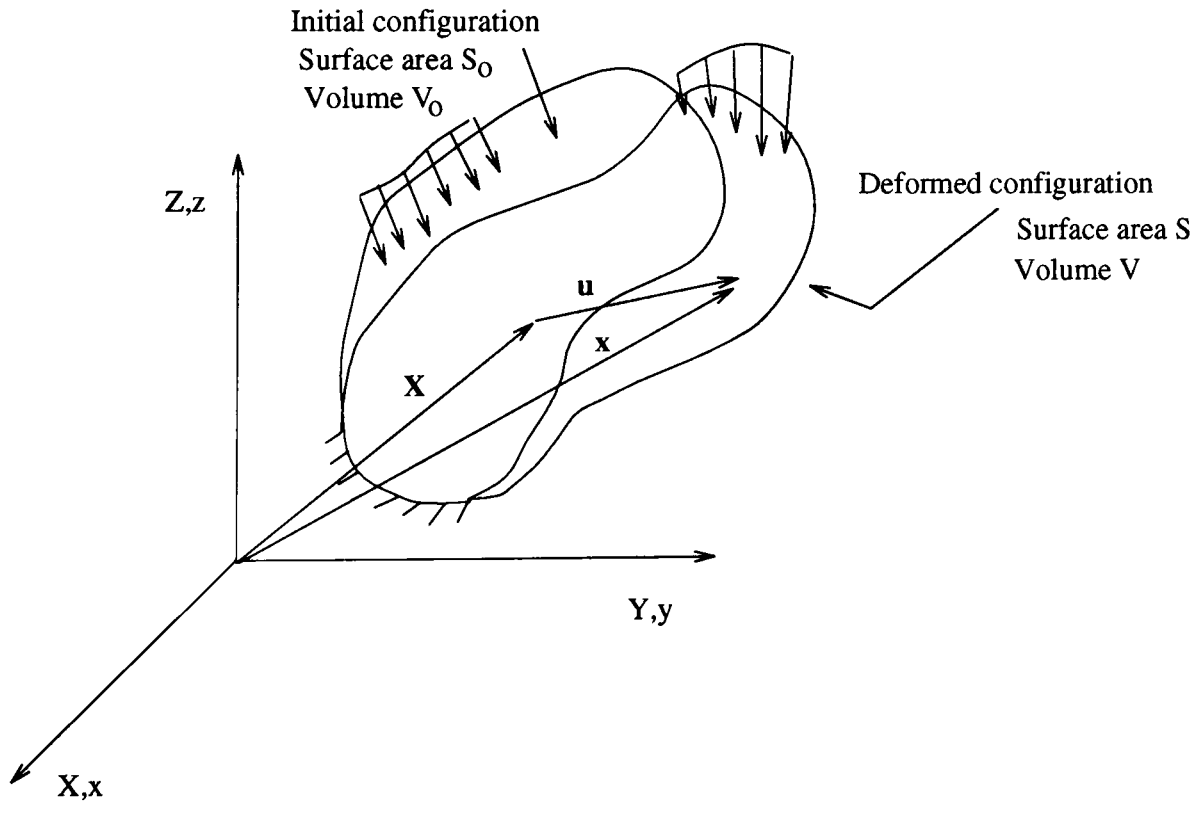

Figure 4.6: Motion of body in Cartesian frame

placement vector $\mathbf{u}$ is a function of $\mathbf{X}$ as:

$$\mathbf{u}(\mathbf{X}) = \begin{bmatrix} u \\ v \\ w \end{bmatrix} \tag{4.6}$$

Where u, v, w are x, y, z components of displacement vector respectively. The current co-ordinates will be:

$$\mathbf{x} = \mathbf{X} + \mathbf{u} \tag{4.7}$$

Where:

$$\mathbf{x} = \begin{bmatrix} x \\ y \\ z \end{bmatrix} \tag{4.8}$$

4.2.2 Stress and strain definitions

The Green's strain, is used in this study which was presented in chapter 2. The index form of this strain is:

$$E_{ij} = \frac{1}{2}[\frac{\partial u_i}{\partial X_j} + \frac{\partial u_j}{\partial X_i}] + \frac{1}{2}\frac{\partial u_k}{\partial X_i}\frac{\partial u_k}{\partial X_j} \tag{4.9}$$

Or in matrix form as:

$$\mathbf{E} = \mathbf{E}_o + \mathbf{E}_{nl} \tag{4.10}$$

where $\mathbf{E}_o$ is linear part of strain tensor and $\mathbf{E}_{nl}$ is nonlinear contribution of strain tensor, which reflects large deformation effects and is negligible in small deformation analysis. The nonlinear term of the strain tensor can be conveniently rewritten [16] as:

$$\mathbf{E}_{nl} = \frac{\mathbf{1}}{\mathbf{2}}\mathbf{A}(\boldsymbol{\theta})\boldsymbol{\theta} \tag{4.11}$$

where:

$$\boldsymbol{\theta} = \begin{bmatrix} \boldsymbol{\theta}_X \\ \boldsymbol{\theta}_Y \\ \boldsymbol{\theta}_Z \end{bmatrix} \tag{4.12}$$

$$\mathbf{A}(\boldsymbol{\theta}) = \begin{bmatrix} \boldsymbol{\theta}_X^T & 0 & 0 \\ 0 & \boldsymbol{\theta}_Y^T & 0 \\ 0 & 0 & \boldsymbol{\theta}_Z^T \\ \boldsymbol{\theta}_Y^T & \boldsymbol{\theta}_X^T & 0 \\ \boldsymbol{\theta}_Z^T & 0 & \boldsymbol{\theta}_X^T \\ 0 & \boldsymbol{\theta}_Z^T & \boldsymbol{\theta}_Y^T \end{bmatrix} \tag{4.13}$$

And typically:

$$\boldsymbol{\theta}_X = \begin{bmatrix} \frac{\partial u}{\partial X} \\ \frac{\partial v}{\partial X} \\ \frac{\partial w}{\partial X} \end{bmatrix} \tag{4.14}$$

The complete strain tensor can be rewritten as [16]:

$$\mathbf{E} = \mathbf{E}_o + \frac{1}{2}\mathbf{A}(\boldsymbol{\theta})\boldsymbol{\theta} \tag{4.15}$$

Where in vector form can be presented as:

$$\mathbf{E} = \begin{bmatrix} \epsilon_{XX} & \epsilon_{YY} & \epsilon_{ZZ} & \gamma_{XY} & \gamma_{XZ} & \gamma_{YZ} \end{bmatrix}^T \tag{4.16}$$

The stress associated with Green's strain is the second Piola-Kirchhoff stress which in vector form is given as:

$$\tilde{\boldsymbol{\sigma}} = \begin{bmatrix} \tilde{\sigma}_{XX} & \tilde{\sigma}_{YY} & \tilde{\sigma}_{ZZ} & \tilde{\sigma}_{XY} & \tilde{\sigma}_{XZ} & \tilde{\sigma}_{YZ} \end{bmatrix}^T \tag{4.17}$$

The relation between $\tilde{\boldsymbol{\sigma}}$ and Green's strain, $\mathbf{E}$, is assumed linear (Hook's law) and is given by:

$$\tilde{\boldsymbol{\sigma}} = \mathbf{DE} \tag{4.18}$$

where **D** is the elasticity matrix containing the elastic material terms, which in three dimensions is given by:

$$\mathbf{D} = \frac{E}{(1+\nu)(1-2\nu)} \begin{bmatrix} 1-\nu & \nu & \nu & 0 & 0 & 0 \\ \nu & 1-\nu & \nu & 0 & 0 & 0 \\ \nu & \nu & 1-\nu & 0 & 0 & 0 \\ 0 & 0 & 0 & \frac{1-2\nu}{2} & 0 & 0 \\ 0 & 0 & 0 & 0 & \frac{1-2\nu}{2} & 0 \\ 0 & 0 & 0 & 0 & 0 & \frac{1-2\nu}{2} \end{bmatrix} \tag{4.19}$$

Where E and ν are the Young's modulus and Poisson's ratio respectively.

4.2.3 Equilibrium equations

The static equilibrium equation of a solid body with current volume V, which initially occupied volume V_o has the form:

$$\frac{\partial \sigma^o_{ji}}{\partial X_j} + b^o_i = 0 \tag{4.20}$$

Here σ^o_{ji} is the first Piola-Kirchhoff stress tensor and b^o_i is the body force per unit of initial volume. By expressing equation (4.20) in terms of the second Piola-Kirchhoff stress tensor $\tilde{\boldsymbol{\sigma}}$, which is work conjugate with the Green's strain tensor, we have:

$$\frac{\partial (F_{ik}\tilde{\sigma}_{jk})}{\partial X_j} + b^o_i = 0 \tag{4.21}$$

where:

$$F_{ik} = \frac{\partial x_i}{\partial X_k} \tag{4.22}$$

F is deformation gradient tensor.

4.2.4 Boundary conditions

The boundary conditions are assumed:

$$t^o_i - t^o_{pi} = 0 \qquad \text{on} \quad S^t_o \tag{4.23}$$

$$u_i - u_{pi} = 0 \qquad \text{on} \quad S_o^u \tag{4.24}$$

Where S_o^t and S_o^u are parts of the boundary where prescribed traction t_{pi}^o and prescribed displacements u_{pi} are applied respectively. t_{pi}^o acts on the deformed element but is measured per unit of undeformed area. In terms of the second Piola-Kirchhoff stress tensor, employed in our formulation as stress measure, the boundary condition (4.23) can be rewritten as:

$$t_i^o = F_{ik}\tilde{t}_k = F_{ik}\tilde{\sigma}_{jk}n_j^o \tag{4.25}$$

$$F_{ik}\tilde{\sigma}_{jk}n_j^o - t_{pi}^o = 0 \qquad \text{on} \quad S_o^t \tag{4.26}$$

Where n_j^o are components of the outward unit normal vector to the surface of the body in the initial configuration.

4.2.5 Discretization of the equilibrium equations

Both FE and FV methods integrate the equilibrium equations over their respective control volumes. The FV technique can be classed as a weighted residual procedure where the overall residual for the whole domain is required to be zero. With this view point, vertex-based FV can be considered to be a particular case of finite elements with a non-Galerkin weighting. Following discussions reveal this point. The weighted residual form of the equilibrium equations(4.21) when accompanied by boundary conditions(4.25) can be written [48, 55] as:

$$\int_{V_o} W_m^T[\frac{\partial(F_{ik}\tilde{\sigma}_{jk})}{\partial X_j} + b_i^o]dV_o + \int_{S_o^t} W_{tm}^T[F_{ik}\tilde{\sigma}_{jk}n_j^o - t_{pi}^o]dS_o + \int_{S_o^u} W_{um}^T(u_i - u_{pi})dS_o = 0 \qquad m = 1, 2, ..., n \tag{4.27}$$

Where W_m, W_{tm} and W_{um} are weighting functions taken for internal and boundary control volumes. By assuming [48] $W_{um} = 0$ in S_o^u, choosing $W_{tm} = -W_m$ and integrating by parts the first term of the first integral of equation(4.27) becomes:

$$\int_{V_o} \frac{\partial[W_m^T(F_{ik}\tilde{\sigma}_{jk})]}{\partial X_j}dV_o - \int_{V_o} \frac{\partial W_m^T}{\partial X_j}F_{ik}\tilde{\sigma}_{jk}dV_o + \int_{V_o} W_m^T b_i^o dV_o - \int_{S_o^t} W_m^T F_{ik}\tilde{\sigma}_{jk}n_j^o dS_o + \int_{S_o^t} W_m^T t_{pi}^o dS_o = 0 \tag{4.28}$$

The first volume integral can be transformed into a surface integral based on the divergence theorem:

$$\int_{S_o} W_m^T F_{ik}\tilde{\sigma}_{jk} n_j^o dS_o - \int_{V_o} \frac{\partial W_m^T}{\partial X_j} F_{ik}\tilde{\sigma}_{jk} dV_o - \int_{S_o^t} W_m^T F_{ik}\tilde{\sigma}_{jk} n_j^o dS_o + \int_{V_o} W_m^T b_i^o dV_o + \int_{S_o^t} W_m^T t_{pi}^o dS_o = 0 \quad (4.29)$$

By considering $S_o^t \bigcup S_o^u = S_o$ the first and the second surface integrals can be treated as integrals over S_o^u, so:

$$-\int_{V_o} \frac{\partial W_m^T}{\partial X_j} F_{ik}\tilde{\sigma}_{jk} dV_o + \int_{S_o^u} W_m^T F_{ik}\tilde{\sigma}_{jk} n_j^o dS_o + \int_{V_o} W_m^T b_i^o dV_o + \int_{S_o^t} W_m^T t_{pi}^o dS_o = 0 \quad (4.30)$$

The indicial form of the above equation can be re-expressed in matrix form which is useful in programming for both the FE and FV formulations:

$$-\int_{V_o} \mathbf{F}(\mathbf{LW})^T \tilde{\boldsymbol{\sigma}} dV_o + \int_{S_o^u} \mathbf{W}^T \mathbf{F}\mathbf{T}\tilde{\boldsymbol{\sigma}} dS_o + \int_{V_o} \mathbf{W}^T \mathbf{b}^o dV_o + \int_{S_o^t} \mathbf{W}^T \mathbf{t}_p^o dS_o = 0 \quad (4.31)$$

Where:

$$\mathbf{T} = \begin{bmatrix} n_X & 0 & 0 & n_Y & n_Z & 0 \\ 0 & n_Y & 0 & n_X & 0 & n_Z \\ 0 & 0 & n_Z & 0 & n_X & n_Y \end{bmatrix} \quad (4.32)$$

$$\mathbf{F} = \begin{bmatrix} \frac{\partial x}{\partial X} & \frac{\partial x}{\partial Y} & \frac{\partial x}{\partial Z} \\ \frac{\partial y}{\partial X} & \frac{\partial y}{\partial Y} & \frac{\partial y}{\partial Z} \\ \frac{\partial z}{\partial X} & \frac{\partial z}{\partial Y} & \frac{\partial z}{\partial Z} \end{bmatrix} \quad (4.33)$$

$$\mathbf{L} = \begin{bmatrix} \frac{\partial}{\partial X} & 0 & 0 \\ 0 & \frac{\partial}{\partial Y} & 0 \\ 0 & 0 & \frac{\partial}{\partial Z} \\ \frac{\partial}{\partial Y} & \frac{\partial}{\partial X} & 0 \\ \frac{\partial}{\partial Z} & 0 & \frac{\partial}{\partial X} \\ 0 & \frac{\partial}{\partial Z} & \frac{\partial}{\partial Y} \end{bmatrix} \quad (4.34)$$

4.2.6 Discretization of the solution domain

The above formulations are based on the general weighted residual method and are applicable to either FE or FV approximations. Depending on the form of weighting function, **W**, adopted equation (4.31) leads to both the FE and FV formulations. To define the control volume over a mesh domain, there is a number of possibilities [4]. The control volume in this study is generated by connecting the centres of the mesh elements to the centre of their faces. This creates sub-control volumes in each mesh element. Combining all the sub-control volumes from all the mesh elements associated with a node, creates a polyhedral type cell that surrounds each of the nodes representing the vertices of the mesh elements. Defining control volumes in this manner is known as the cell vertex control volume or vertex centred control volume [58].

Figure 3.9 illustrates the CV definition based on this method with regard to a two dimensional mesh. In both of the finite element and finite volume techniques the weighted form of the equilibrium equation (4.31) with relevant form of weighting function **W** is integrated over relevant control volumes.

4.3 Bobnov-Galerkin finite element method

In the Galerkin approach [35, 59], the weighting function **W** is chosen as $W_m = N_m$ where N_m are the shape functions corresponding to node m. By introducing N_m to the general form of equilibrium equation (4.30), the surface integral over S_u^o disappears as N_m is zero at the boundary control volumes [48]. So for the finite element method, the equilibrium equation in matrix form is expressed as:

$$\int_{V_o} \mathbf{F}(\mathbf{LN})^T \tilde{\boldsymbol{\sigma}} dV_o - \boldsymbol{R} = 0 \tag{4.35}$$

Where:

$$\mathbf{R} = \int_{V_o} \mathbf{N}^T \mathbf{b}^o dV_o + \int_{S_o^t} \mathbf{N}^T \mathbf{t}_p^o dS_o \tag{4.36}$$

By interpolating the displacement field, $\mathbf{u}$, and the displacement gradients, $\boldsymbol{\theta}$, for individual elements we have:

$$\mathbf{u} = \mathbf{N}\bar{\mathbf{u}} \tag{4.37}$$

$$\boldsymbol{\theta} = \mathbf{G}\bar{\mathbf{u}} \tag{4.38}$$

The matrix $\mathbf{N}$ contains elemental shape functions and matrix $\mathbf{G}$, the gradient matrix. includes derivatives of these shape functions:

$$\mathbf{N} = \begin{bmatrix} \mathbf{N}_1 & \mathbf{N}_2 & \cdots & \mathbf{N}_n \end{bmatrix} \tag{4.39}$$

$$\mathbf{G} = \begin{bmatrix} \mathbf{G}_1 & \mathbf{G}_2 & \cdots & \mathbf{G}_n \end{bmatrix} \tag{4.40}$$

Where the submatrices $\mathbf{N}_m$ and $\mathbf{G}_m$, correspond to node m, are:

$$\mathbf{N}_m = \begin{bmatrix} N_m & 0 & 0 \\ 0 & N_m & 0 \\ 0 & 0 & N_m \end{bmatrix} \tag{4.41}$$

$$\mathbf{G}_m = \begin{bmatrix} \frac{\partial N_m}{\partial X} & 0 & 0 \\ 0 & \frac{\partial N_m}{\partial X} & 0 \\ 0 & 0 & \frac{\partial N_m}{\partial X} \\ \frac{\partial N_m}{\partial Y} & 0 & 0 \\ 0 & \frac{\partial N_m}{\partial Y} & 0 \\ 0 & 0 & \frac{\partial N_m}{\partial Y} \\ \frac{\partial N_m}{\partial Z} & 0 & 0 \\ 0 & \frac{\partial N_m}{\partial Z} & 0 \\ 0 & 0 & \frac{\partial N_m}{\partial Z} \end{bmatrix} \tag{4.42}$$

Linear part of Green's strain vector can be written as:

$$\epsilon_{\mathbf{o}} = \mathbf{B}_o\bar{\mathbf{u}} \tag{4.43}$$

Where:

$$\mathbf{B}_o = \mathbf{LN} = \begin{bmatrix} \mathbf{B}_{o1} & \mathbf{B}_{o2} & \cdots & \mathbf{B}_{on} \end{bmatrix} \tag{4.44}$$

$$\mathbf{B}_{oi} = \begin{bmatrix} \frac{\partial N_i}{\partial X} & 0 & 0 \\ 0 & \frac{\partial N_i}{\partial Y} & 0 \\ 0 & 0 & \frac{\partial N_i}{\partial Z} \\ \frac{\partial N_i}{\partial Y} & \frac{\partial N_i}{\partial X} & 0 \\ \frac{\partial N_i}{\partial Z} & 0 & \frac{\partial N_i}{\partial X} \\ 0 & \frac{\partial N_i}{\partial Z} & \frac{\partial N_i}{\partial Y} \end{bmatrix} \tag{4.45}$$

$$\bar{\mathbf{u}} = \begin{bmatrix} u_1 & v_1 & w_1 & \cdots & u_n & v_n & w_n \end{bmatrix}^T \tag{4.46}$$

Corresponding to total degrees of freedom of the element, matrix $\mathbf{F}$ in equation (4.35) has to be extended to diagonal matrix $\bar{\mathbf{F}}$ as:

$$\bar{\mathbf{F}} = \begin{bmatrix} \mathbf{F} & 0 & 0 \\ 0 & \ddots & 0 \\ 0 & 0 & \mathbf{F} \end{bmatrix} \tag{4.47}$$

The order of $\bar{\mathbf{F}}$ is equal to the total degrees of freedom of the element. By defining $\mathbf{B}$ as:

$$\mathbf{B}^T = \bar{\mathbf{F}}(\mathbf{LN})^T = \bar{\mathbf{F}}\mathbf{B_o}^T \tag{4.48}$$

equation (4.35) is rewritten as:

$$\int_{V_o} \mathbf{B}^T \tilde{\boldsymbol{\sigma}} dV_o - \boldsymbol{R} = \mathbf{0} \tag{4.49}$$

Matrix $\mathbf{B}$ can be rearranged as:

$$\mathbf{B} = \mathbf{B}_o + \mathbf{A}(\boldsymbol{\theta})\mathbf{G} \tag{4.50}$$

The matrix $\mathbf{B}$ can be presented in terms of nodal submatrices as:

$$\mathbf{B} = \begin{bmatrix} \mathbf{B}_1 & \mathbf{B}_2 & \cdots & \mathbf{B}_n \end{bmatrix} \tag{4.51}$$

Where the nodal submatrix $\mathbf{B}_i$ is:

$$\mathbf{B}_i = \begin{bmatrix} \frac{\partial N_i}{\partial X}(1+\frac{\partial u}{\partial X}) & \frac{\partial N_i}{\partial X}\frac{\partial v}{\partial X} & \frac{\partial N_i}{\partial X}\frac{\partial w}{\partial X} \\ \frac{\partial N_i}{\partial Y}\frac{\partial u}{\partial Y} & \frac{\partial N_i}{\partial Y}(1+\frac{\partial v}{\partial Y}) & \frac{\partial N_i}{\partial Y}\frac{\partial w}{\partial Y} \\ \frac{\partial N_i}{\partial Z}\frac{\partial u}{\partial Z} & \frac{\partial N_i}{\partial Z}\frac{\partial v}{\partial Z} & \frac{\partial N_i}{\partial Z}(1+\frac{\partial w}{\partial Z}) \\ \frac{\partial N_i}{\partial X}\frac{\partial u}{\partial Y}+\frac{\partial N_i}{\partial Y}(1+\frac{\partial u}{\partial X}) & \frac{\partial N_i}{\partial Y}\frac{\partial v}{\partial X}+\frac{\partial N_i}{\partial X}(1+\frac{\partial v}{\partial Y}) & \frac{\partial N_i}{\partial X}\frac{\partial w}{\partial Y}+\frac{\partial N_i}{\partial Y}\frac{\partial w}{\partial X} \\ \frac{\partial N_i}{\partial X}\frac{\partial u}{\partial Z}+\frac{\partial N_i}{\partial Z}(1+\frac{\partial u}{\partial X}) & \frac{\partial N_i}{\partial X}\frac{\partial v}{\partial Z}+\frac{\partial N_i}{\partial Z}\frac{\partial v}{\partial X} & \frac{\partial N_i}{\partial Z}\frac{\partial w}{\partial X}+\frac{\partial N_i}{\partial X}(1+\frac{\partial w}{\partial Z}) \\ \frac{\partial N_i}{\partial Y}\frac{\partial u}{\partial Z}+\frac{\partial N_i}{\partial Z}\frac{\partial u}{\partial Y} & \frac{\partial N_i}{\partial Y}\frac{\partial v}{\partial Z}+\frac{\partial N_i}{\partial Z}(1+\frac{\partial v}{\partial Y}) & \frac{\partial N_i}{\partial Z}\frac{\partial w}{\partial Y}+\frac{\partial N_i}{\partial Y}(1+\frac{\partial w}{\partial Z}) \end{bmatrix} \tag{4.52}$$

By considering the equations (4.12), (4.15) and (4.43), the Green's strain vector is expressed as:

$$\boldsymbol{\epsilon} = [\mathbf{B}_o + \frac{\mathbf{1}}{\mathbf{2}}\mathbf{A}(\boldsymbol{\theta})\mathbf{G}]\bar{\mathbf{u}} = [\mathbf{B} - \frac{\mathbf{1}}{\mathbf{2}}\mathbf{A}(\boldsymbol{\theta})\mathbf{G}]\bar{\mathbf{u}} = \tilde{\mathbf{B}}\bar{\mathbf{u}} \tag{4.53}$$

Where the nodal submatrix $\tilde{\mathbf{B}}_i$ is:

$$\tilde{\mathbf{B}}_i = \begin{bmatrix} \frac{\partial N_i}{\partial X}(1+\frac{1}{2}\frac{\partial u}{\partial X}) & \frac{1}{2}\frac{\partial N_i}{\partial X}\frac{\partial v}{\partial X} & \frac{1}{2}\frac{\partial N_i}{\partial X}\frac{\partial w}{\partial X} \\ \frac{1}{2}\frac{\partial N_i}{\partial Y}\frac{\partial U}{\partial Y} & \frac{\partial N_i}{\partial Y}(1+\frac{1}{2}\frac{\partial v}{\partial Y}) & \frac{1}{2}\frac{\partial N_i}{\partial Y}\frac{\partial w}{\partial Y} \\ \frac{1}{2}\frac{\partial N_i}{\partial Z}\frac{\partial u}{\partial Z} & \frac{1}{2}\frac{\partial N_i}{\partial Z}\frac{\partial v}{\partial Z} & \frac{\partial N_i}{\partial Z}(1+\frac{1}{2}\frac{\partial w}{\partial Z}) \\ \frac{1}{2}\frac{\partial N_i}{\partial X}\frac{\partial u}{\partial Y}+\frac{\partial N_i}{\partial Y}(1+\frac{1}{2}\frac{\partial u}{\partial X}) & \frac{1}{2}\frac{\partial N_i}{\partial Y}\frac{\partial v}{\partial X}+\frac{\partial N_i}{\partial X}(1+\frac{1}{2}\frac{\partial v}{\partial Y}) & \frac{1}{2}\frac{\partial N_i}{\partial X}\frac{\partial w}{\partial Y}+\frac{1}{2}\frac{\partial N_i}{\partial Y}\frac{\partial w}{\partial X} \\ \frac{1}{2}\frac{\partial N_i}{\partial X}\frac{\partial u}{\partial Z}+\frac{\partial N_i}{\partial Z}(1+\frac{1}{2}\frac{\partial u}{\partial X}) & \frac{1}{2}\frac{\partial N_i}{\partial X}\frac{\partial v}{\partial Z}+\frac{1}{2}\frac{\partial N_i}{\partial Z}\frac{\partial v}{\partial X} & \frac{1}{2}\frac{\partial N_i}{\partial Z}\frac{\partial w}{\partial X}+\frac{\partial N_i}{\partial X}(1+\frac{1}{2}\frac{\partial w}{\partial Z}) \\ \frac{1}{2}\frac{\partial N_i}{\partial Y}\frac{\partial u}{\partial Z}+\frac{1}{2}\frac{\partial N_i}{\partial Z}\frac{\partial u}{\partial Y} & \frac{1}{2}\frac{\partial N_i}{\partial Y}\frac{\partial v}{\partial Z}+\frac{\partial N_i}{\partial Z}(1+\frac{1}{2}\frac{\partial v}{\partial Y}) & \frac{1}{2}\frac{\partial N_i}{\partial Z}\frac{\partial w}{\partial Y}+\frac{\partial N_i}{\partial Y}(1+\frac{1}{2}\frac{\partial w}{\partial Z}) \end{bmatrix} \tag{4.54}$$

Tangent stiffness matrix $\mathbf{K}_t^e$ of the element can also be calculated by employing the principle of virtual work. These approaches are explained in Zienkiewicz [16] and Crisfield [60]. However matrix $\mathbf{K}_t^e$ may be expressed [61] as:

$$\mathbf{K}_t^e = \mathbf{K}^e + \mathbf{K}_\sigma^e \tag{4.55}$$

Where:

$$\mathbf{K}^e = \int_{V_o} \mathbf{B}^T\mathbf{D}\mathbf{B}dV_o \quad , \quad \mathbf{K}_\sigma^e = \int_{V_o} \mathbf{G}^T\mathbf{P}\mathbf{G}dV_o \tag{4.56}$$

Matrix $\mathbf{K}^e$ is referred to as the linear stiffness matrix and $\mathbf{K}_\sigma^e$ is referred to as the

"initial stress" or "geometric" contribution to the tangent stiffness matrix, where:

$$\mathbf{P} = \begin{bmatrix} \tilde{\sigma}_{XX}\mathbf{I} & \tilde{\sigma}_{YX}\mathbf{I} & \tilde{\sigma}_{ZX}\mathbf{I} \\ \tilde{\sigma}_{XY}\mathbf{I} & \tilde{\sigma}_{YY}\mathbf{I} & \tilde{\sigma}_{ZY}\mathbf{I} \\ \tilde{\sigma}_{XZ}\mathbf{I} & \tilde{\sigma}_{YZ}\mathbf{I} & \tilde{\sigma}_{ZZ}\mathbf{I} \end{bmatrix} \tag{4.57}$$

$\mathbf{I}$ being the identity matrix.

The above formulation is the traditional finite element approach for GLN problems. We will now look at the vertex-based finite volume method.

4.4 Finite volume method

The finite volume procedure can be viewed as a special case of the weighted equilibrium equation (4.31) in which:

$$\mathbf{W} = \mathbf{I} \quad \text{in the control volume}$$

$$\mathbf{W} = \mathbf{0} \quad \text{elsewhere}$$

By this choice the first volume integral of equation (4.31) disappears, yielding:

$$\int_{S_o^u} \mathbf{FT}\tilde{\boldsymbol{\sigma}} dS_o - \mathbf{R} = 0 \tag{4.58}$$

Where:

$$\mathbf{R} = -\int_{V_o} \mathbf{b}^o dV_o - \int_{S_o^t} \mathbf{t}_p^o dS_o \tag{4.59}$$

4.4.1 Calculation of tangent stiffness matrix for FVM

The virtual work V_w can be calculated by multiplying the virtual nodal displacement $\delta\bar{\mathbf{u}}_v$ and unbalance force vector $\boldsymbol{\Psi}$ which may be expressed as:

$$\boldsymbol{\Psi} = \int_{S_o^u} \mathbf{FT}\tilde{\boldsymbol{\sigma}} dS_o - \mathbf{R} \tag{4.60}$$

$$V_w = \delta\bar{\mathbf{u}}_v^T \boldsymbol{\Psi} \tag{4.61}$$

The variation of the virtual work is given by

$$\delta V_w = \delta\bar{\mathbf{u}}_v^T \delta\boldsymbol{\Psi} \tag{4.62}$$

$$\delta V_w = \delta\bar{\mathbf{u}}_v^T \frac{\partial\boldsymbol{\Psi}}{\partial\bar{\mathbf{u}}}\delta\bar{\mathbf{u}} = \delta\bar{\mathbf{u}}_v^T \mathbf{K}_t \delta\bar{\mathbf{u}} \tag{4.63}$$

By conservative assumption for the loading vector $\mathbf{R}$:

$$\delta V_w = \delta\bar{\mathbf{u}}_v^T \delta\left(\int_{S_o^u} \mathbf{F}\mathbf{T}\tilde{\boldsymbol{\sigma}} dS_o\right) \tag{4.64}$$

$$\delta V_w = \delta\bar{\mathbf{u}}_v^T \left(\int_{S_o^u} \delta\mathbf{F}\mathbf{T}\tilde{\boldsymbol{\sigma}} dS_o + \int_{S_o^u} \mathbf{F}\mathbf{T}\delta\tilde{\boldsymbol{\sigma}} dS_o\right) \tag{4.65}$$

By use of (4.18) $\delta\tilde{\boldsymbol{\sigma}}$ can be calculated as:

$$\delta\tilde{\boldsymbol{\sigma}} = \mathbf{D}\delta\mathbf{E} = \mathbf{D}\delta\left(\mathbf{B}_o\bar{\mathbf{u}} + \frac{1}{2}\mathbf{A}(\boldsymbol{\theta})\mathbf{G}\bar{\mathbf{u}}\right) = \mathbf{D}\left(\mathbf{B}_o\delta\bar{\mathbf{u}} + \frac{1}{2}(\delta\mathbf{A}(\boldsymbol{\theta}))\mathbf{G}\bar{\mathbf{u}} + \frac{1}{2}\mathbf{A}(\boldsymbol{\theta})\mathbf{G}\delta\bar{\mathbf{u}}\right) \tag{4.66}$$

As $\mathbf{A}$ is a function of $\bar{\mathbf{u}}$ so $\delta\tilde{\boldsymbol{\sigma}}$ may be expressed as:

$$\delta\tilde{\boldsymbol{\sigma}} = \mathbf{D}(\mathbf{B}_o + \mathbf{A}(\boldsymbol{\theta})\mathbf{G})\delta\bar{\mathbf{u}} = \mathbf{D}\mathbf{B}\delta\bar{\mathbf{u}} \tag{4.67}$$

Remark 1:

$$(\delta\mathbf{A}(\theta))\mathbf{G}\bar{\mathbf{u}} = \mathbf{A}(\theta)\mathbf{G}\delta\bar{\mathbf{u}}$$

So the second integral in (4.65) is expressed as:

$$\int_{S_o^u} \mathbf{F}\mathbf{T}\delta\tilde{\boldsymbol{\sigma}} dS_o = \int_{S_o^u} \mathbf{F}\mathbf{T}\mathbf{D}\mathbf{B}\delta\bar{\mathbf{u}} dS_o \tag{4.68}$$

For the calculation of the first integral in (4.65) variation of $\mathbf{F}$ must be calculated. By use of equation (4.33):

$$\delta\mathbf{F} = \begin{bmatrix} \frac{\partial\delta x}{\partial X} & \frac{\partial\delta x}{\partial Y} & \frac{\partial\delta x}{\partial Z} \\ \frac{\partial\delta y}{\partial X} & \frac{\partial\delta y}{\partial Y} & \frac{\partial\delta y}{\partial Z} \\ \frac{\partial\delta z}{\partial X} & \frac{\partial\delta z}{\partial Y} & \frac{\partial\delta z}{\partial Z} \end{bmatrix} \tag{4.69}$$

By substituting of equation (4.7) in above matrix yields:

$$\delta\mathbf{F} = \begin{bmatrix} \frac{\partial \delta u}{\partial X} & \frac{\partial \delta u}{\partial Y} & \frac{\partial \delta u}{\partial Z} \\ \frac{\partial \delta v}{\partial X} & \frac{\partial \delta v}{\partial Y} & \frac{\partial \delta v}{\partial Z} \\ \frac{\partial \delta w}{\partial X} & \frac{\partial \delta w}{\partial Y} & \frac{\partial \delta w}{\partial Z} \end{bmatrix} \tag{4.70}$$

Through matrix calculation, it can be shown that:

$$(\delta\mathbf{F})\mathbf{T}\tilde{\boldsymbol{\sigma}} = \tilde{\mathbf{T}}\mathbf{P}\mathbf{G}\delta\bar{\mathbf{u}} \tag{4.71}$$

Where:

$$\tilde{\mathbf{T}} = \begin{bmatrix} n_X\mathbf{I} & n_Y\mathbf{I} & n_Z\mathbf{I} \end{bmatrix} \tag{4.72}$$

and matrix $\mathbf{P}$ is given by (4.57). Based on these calculations variation V_w can be expressed as:

$$\delta V_w = \delta\bar{\mathbf{u}}_v^T\left(\int_{S_o^u} \mathbf{FTDB}dS_o + \int_{S_o^u} \tilde{\mathbf{T}}\mathbf{P}\mathbf{G}dS_o\right)\delta\bar{\mathbf{u}} \tag{4.73}$$

By comparing the above equation and the equation (4.63) stiffness matrix $\mathbf{K}_t^{cv}$ may be extracted as:

$$\mathbf{K}_t^{cv} = \mathbf{K} + \mathbf{K}_\sigma \tag{4.74}$$

Where:

$$\mathbf{K} = \int_{S_o^u} \mathbf{FTDB}dS_o \quad \text{and} \quad \mathbf{K}_\sigma = \int_{S_o^u} \tilde{\mathbf{T}}\mathbf{P}\mathbf{G}dS_o \tag{4.75}$$

4.4.2 Calculation of element's internal force

As indicated in chapter three in small deformation case of linear elastic problems discretized by CST elements, the internal force terms contributing to the elemental stiffness matrix coincide for FEM and FVM [48]. It can be shown this coincidence again exists in GNL analysis involving CST elements. Following discussion proves this equality of the internal force vector at any arbitrary node i of the domain.

$$\mathbf{P}_i^{FV} = -\int_{S_o^i} \mathbf{FT}\tilde{\boldsymbol{\sigma}}dS_o \tag{4.76}$$

$$\mathbf{P}_i^{FE} = \int_{V_o^i} \mathbf{B}^T\tilde{\boldsymbol{\sigma}}dV_o \tag{4.77}$$

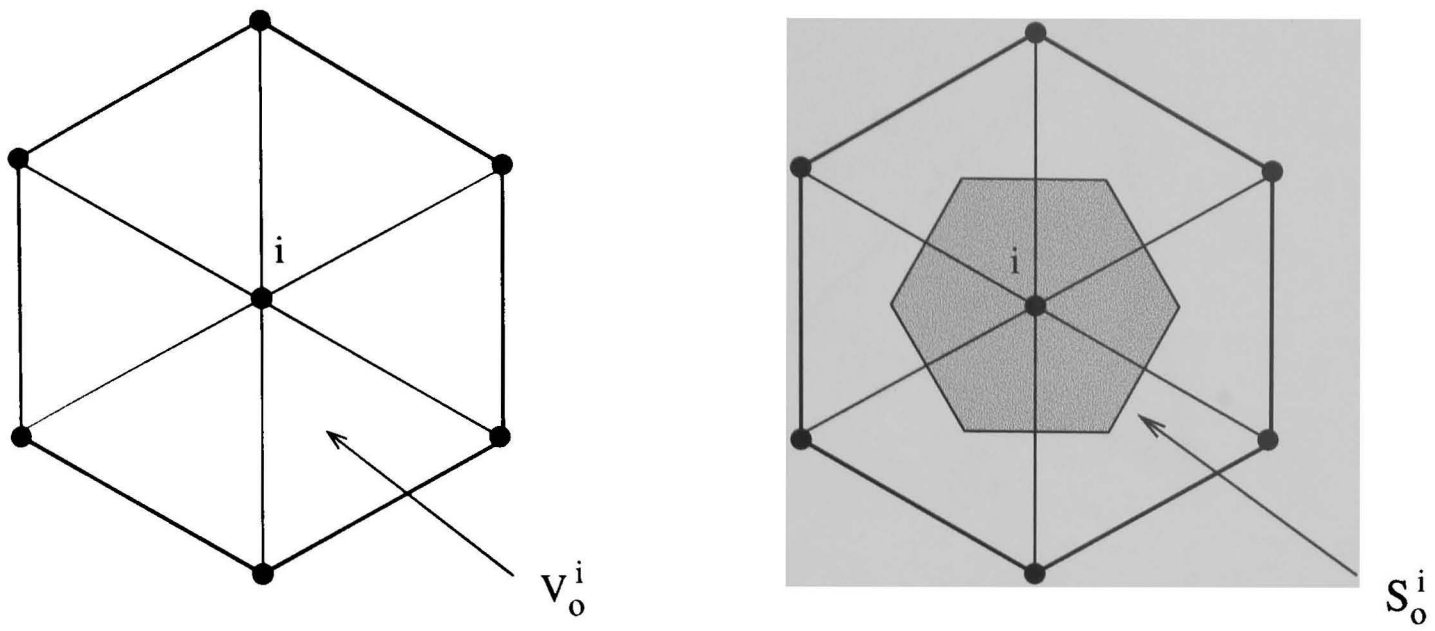

(a) (b)

Figure 4.7: (a) Elements around node i. (b) Element contributions to the control volume at node i.

For FVM using tensor notation and equation (4.76), the kth component of the ith node of the internal force vector is:

$$p_{ik}^{FV} = -\int_{S_o^i} \frac{\partial x_k}{\partial X_r} n_j \sigma_{jr} dS_o = -\sum_{e=1}^{noe} \int_{(S_o^i)^e} \frac{\partial x_k}{\partial X_r} n_j \sigma_{jr} dS_o \tag{4.78}$$

Where noe is the number of neighbouring elements at node i (Figure 4.7-b). By considering relation between deformed coordinates $\mathbf{x}$ and initial coordinates $\mathbf{X}$, equation (4.7). the above equation will be:

$$\begin{aligned} p_{ik}^{FV} &= -\sum_{e=1}^{noe} \int_{(S_o^i)^e} [\delta_{kr} n_j \sigma_{jr} + \frac{\partial u_k}{\partial X_r} n_j \sigma_{jr}] dS_o = \\ &-\sum_{e=1}^{noe} \int_{(S_o^i)^e} [n_j \sigma_{jk} + \frac{\partial u_k}{\partial X_r} n_j \sigma_{jr}] dS_o = \\ &-\sum_{e=1}^{noe} (\sigma_{jk} + \frac{\partial u_k}{\partial X_r} \sigma_{jr}) \int_{(S_o^i)^e} n_j dS_o \end{aligned} \tag{4.79}$$

The strain and stress components are constant over each element, thus allowing to be taken out of the integral.

For the FEM using equation (4.48) and equation (4.77), the kth component of the ith node of the internal force vector is:

$$p_{ik}^{FE} = \int_{V_o^i} \frac{\partial N_i}{\partial X_j} \sigma_{jr} \frac{\partial x_k}{\partial X_r} dv_o = \sum_{e=1}^{noe} \int_{(V_o^i)^e} \frac{\partial N_i}{\partial X_j} \sigma_{jr} \frac{\partial x_k}{\partial X_r} dv_o \tag{4.80}$$

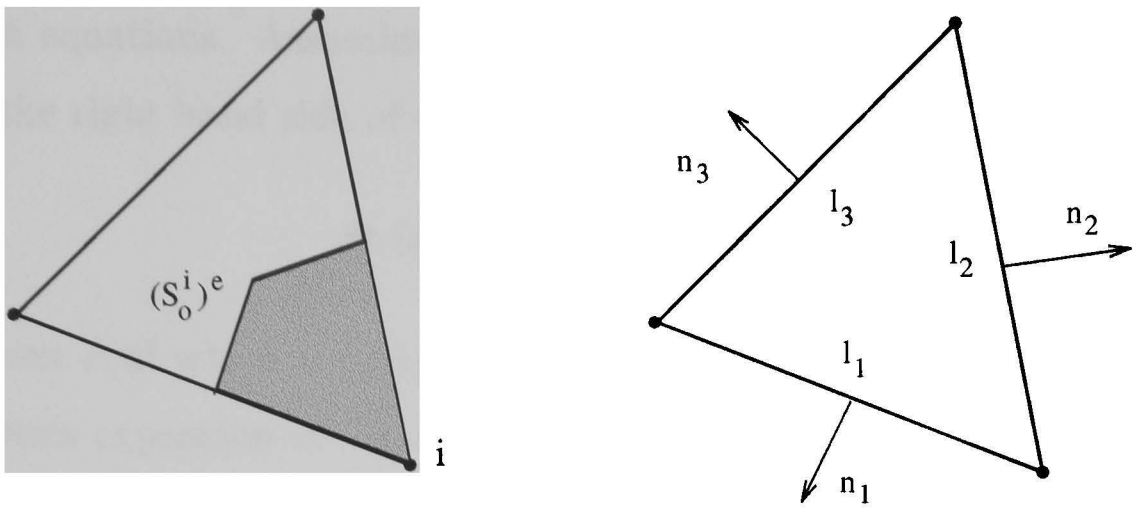

Figure 4.8: Single CST element: (a) elemental contributions and; (b) normal vector and lengths of element sides.

Again by using equation (4.7) the above equation will be:

$$p_{ik}^{FE} = \sum_{e=1}^{noe} \int_{(V_o^i)^e} [\frac{\partial N_i}{\partial X_j} \sigma_{jr} \delta_{kr} + \frac{\partial N_i}{\partial X_j} \sigma_{jr} \frac{\partial u_k}{\partial X_r}] dv_o = \tag{4.81}$$

$$\sum_{e=1}^{noe} \int_{(V_o^i)^e} (\sigma_{jk} + \frac{\partial u_k}{\partial X_r} \sigma_{jr}) \int_{(V_o^i)^e} \frac{\partial N_i}{\partial X_j} dv_o$$

The contributions for the two methods will be identical if the integral in equations (4.79).(4.81) are equal.

But for the eth element from element contributions at node i , Figure 4.8, we can write:

$$\int_{(V_o^i)^e} \frac{\partial N_i^e}{\partial x_j} \mathrm{dV_o} = \int_{(\partial V_o^i)^e} n_j N_i \mathrm{dS_o} = (n_1)_j \frac{1}{2} l_1 + (n_2)_j \frac{1}{2} l_2 = -\int_{(S_o^i)^e} n_j dS_o \tag{4.82}$$

This equivalence will be further illustrated by results of test case two.

4.4.3 Solution procedure of nonlinear equilibrium equations

The assembled equilibrium equation (4.58) is nonlinear and can be solved by the Newton-Ralphson method [62] involving a series of solution to linear incremental

equilibrium equations. Assuming an initial estimate of the total displacements $\bar{\mathbf{u}}^i$ for which the right hand side of equation (4.58) is not zero where can be shown as:

$$\mathbf{\Psi}\ (\bar{\mathbf{u}}^i) = \int_{S_o^u} \mathbf{F}\mathbf{T}\tilde{\boldsymbol{\sigma}} dS_o - \mathbf{R} \tag{4.83}$$

An increment $\Delta\bar{\mathbf{u}}^i$ which is necessary to achieve equilibrium, can be calculated by Taylor's series expansion of $\mathbf{\Psi}$ about $\bar{\mathbf{u}}^i$ by ignoring third and succeeding terms, as:

$$\mathbf{\Psi}\ (\bar{\mathbf{u}}^i + \Delta\bar{\mathbf{u}}^i) = \mathbf{\Psi}\ (\bar{\mathbf{u}}^i) + \mathbf{K}_t^{cv}\Delta\bar{\mathbf{u}}^i \tag{4.84}$$

Where $\mathbf{K}_t^{cv}$ is tangent stiffness matrix which has been calculated in section 4.4.1. Resulting increment $\Delta\bar{\mathbf{u}}^i$ in nodal displacements is obtained as:

$$\Delta\bar{\mathbf{u}}^i = -[\mathbf{K}_t^{cv}]^{-1}\mathbf{\Psi}(\bar{\mathbf{u}}^i) \tag{4.85}$$

from which a new approximation for the total displacements can be obtained as:

$$\bar{\mathbf{u}}^{i+1} = \bar{\mathbf{u}}^i + \Delta\bar{\mathbf{u}}^i \tag{4.86}$$

This iteration process continues until a given convergence criteria is satisfied. In the present work the ratio of Euclidean norms of out of balance force vector and applied load vector are considered as the convergence criteria:

$$\frac{\|\ \mathbf{\Psi}\ (\bar{\mathbf{u}}^i)\|}{\|\mathbf{R}\|} < \text{Tolerance} \tag{4.87}$$

4.5 Results and Discussion

Both the FEM and FVM result in a system of equations of the form:

$$\mathbf{K}\mathbf{U} = \mathbf{P} \tag{4.88}$$

Where $\mathbf{K}$ is the system stiffness matrix, $\mathbf{U}$ is the displacement vector and $\mathbf{P}$ is the force vector acting on the system. As discussed before, the solution of these equations is achieved through an iterative procedure based on the Newton- Ralphson

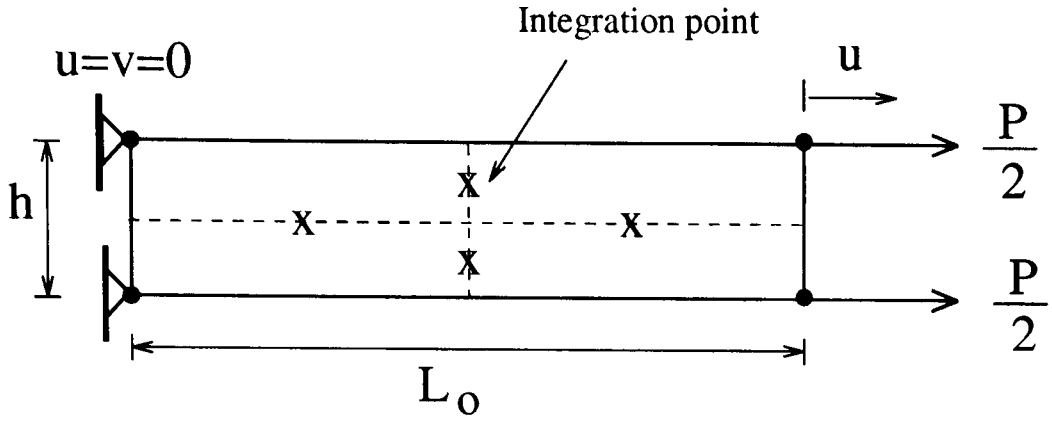

Figure 4.9: Tensile strip

method [62]. The tolerance value in equation(4.87) was considered as 0.001 for both methods. The conjugate gradient solver was used for solving the linear equations formed in the iteration procedure of the Newton-Ralphson method. Although in the FVM the stiffness matrix **K** is nonsymmetric but for the structured mesh, applied in the following test cases, the nonsymmetry is not too severe that this solver cannot be applied. To illustrate the effectiveness of the cell vertex finite volume method for analysis of GNL problems four test problems have been studied.

4.5.1 Test case-1

The first test problem was a tensile strip (Figure 4.9). The tensile strip was discretized by one bilinear quadrilateral element, plane stress assumption was made and the following properties have been assumed:

L_o=100 cm h=5 cm

$A_o = 5cm^2$ E=2.16x10^7 N/cm^2 $\nu = 0$

The volume integrals for the finite element analysis were approximated using a four-point Gauss rule for quadrilateral elements and the surface integrals for the finite volume method were approximated by summation of quantities of integrands at the integration points as shown in Figure 4.9. For validation, the solutions of an in-house FV code and FE code developed for GNL analysis were compared with analytical results which are available [56, 60]. The analytical load-deformation relation

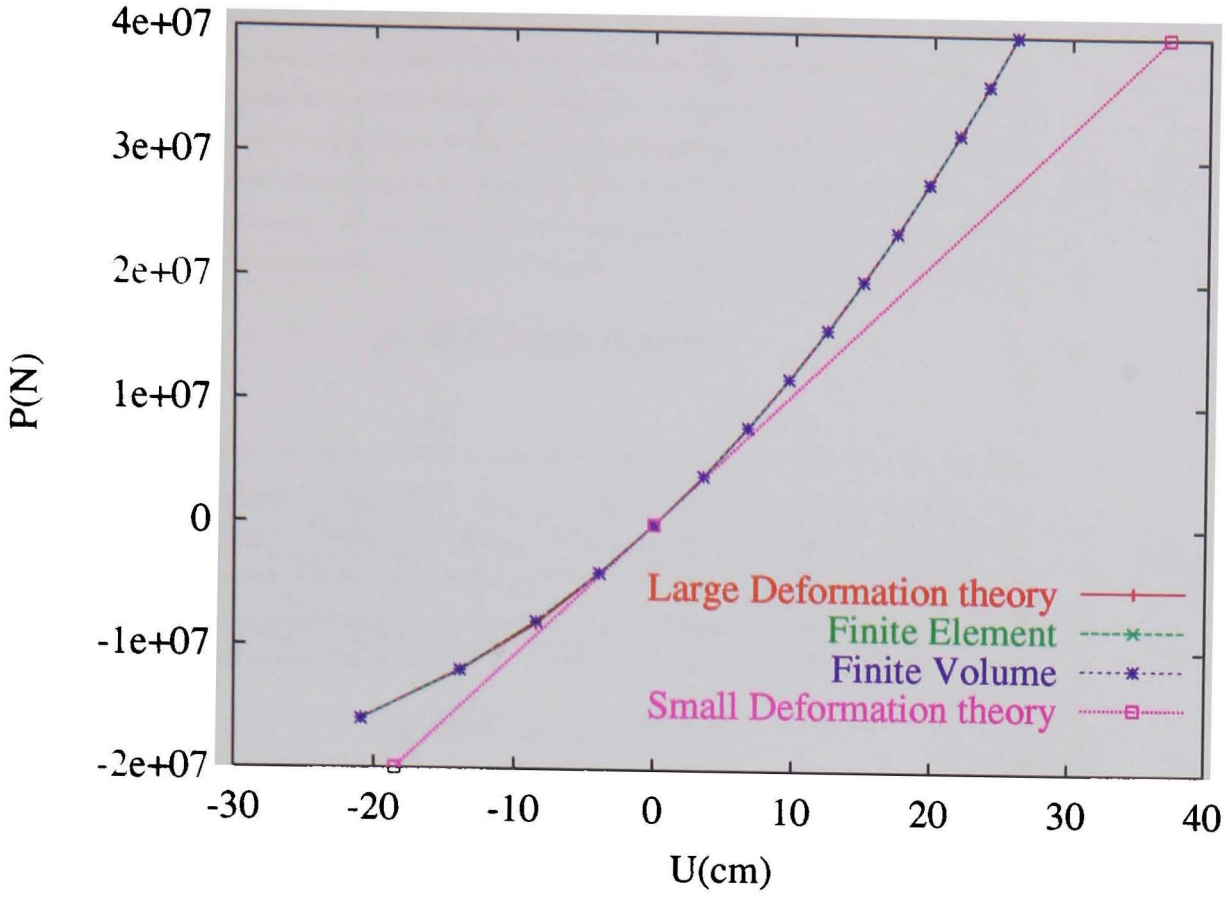

Figure 4.10: Load-Deformation response for tensile strip

based on Green's strain definition [60] is given as:

$$P_G = \frac{A_o L}{L_o} E\epsilon_G = EA_o(1 + \frac{u}{L_o})(\frac{u}{L_o} + \frac{1}{2}(\frac{u}{L_o})^2) \tag{4.89}$$

Figure 4.10 shows good agreement between results of three methods.

4.5.2 Test case-2

The second test problem was a cantilever beam under a concentrated load. The geometry and material properties were the same as for the first test and the BLQ elements (Figure 4.11-a) and the CST elements (Figure 4.11-b) have been used for discretization. Vertical and horizontal displacements at the centre of the free end were calculated by both techniques and have been compared with the analytical results taken from Timoshenko [63].

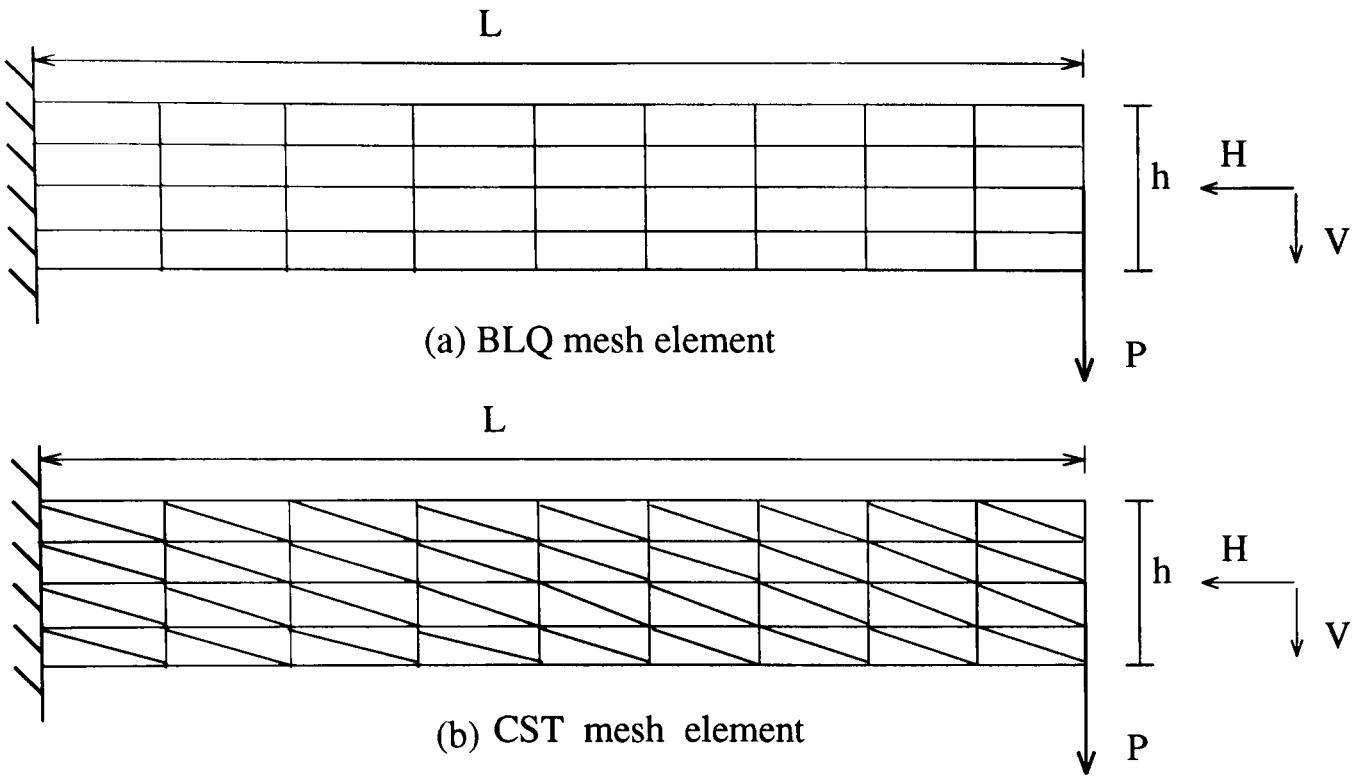

Figure 4.11: End mid-point loaded cantilever beam

Figures 4.12-a and 4.12-b show the FEM's results and Figures 4.12-c and 4.12-d show the FVM's results in all load levels. These figures show the results of both FE and FV formulations are convergent to the analytical results and with the same mesh density, FE results are slightly closer to the analytical results. In Figure 4.13, corresponding to load P equal to $\frac{3EI}{L^2}$, the results of the FE and the FV for the tip displacement are compared together in different total number of BLQ elements. These results demonstrate that for a low number of elements, the differences between FE and FV is considerable, but by increasing the number of elements the two methods converge to the analytical results. By applying small deformation theory, the different rate of convergence for the FE and the FV can be seen again, Figure 4.13-c shows this different rate.

Figure 4.14 shows the Von Mises stress distribution over the beam and the graphs show the variation of this stress along the top surface of the beam for the both FE and FV methods which predict the same results. In both methods 1280 elements are applied.

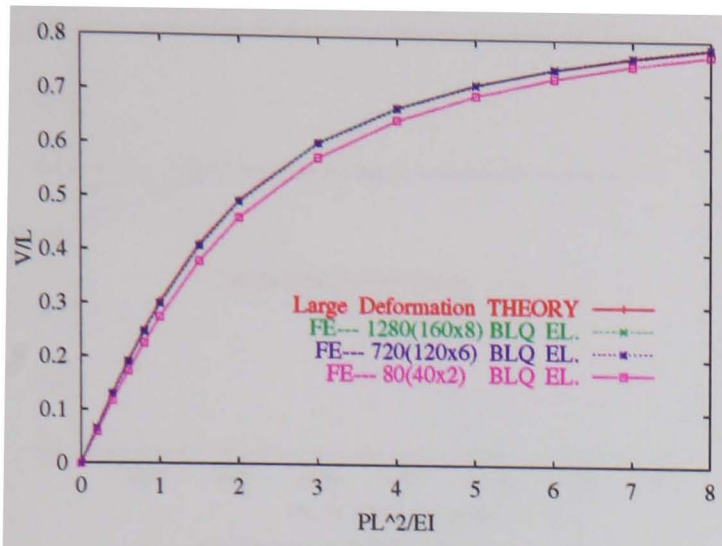

(a)- Vertical displacement of cantilever beam(FE)

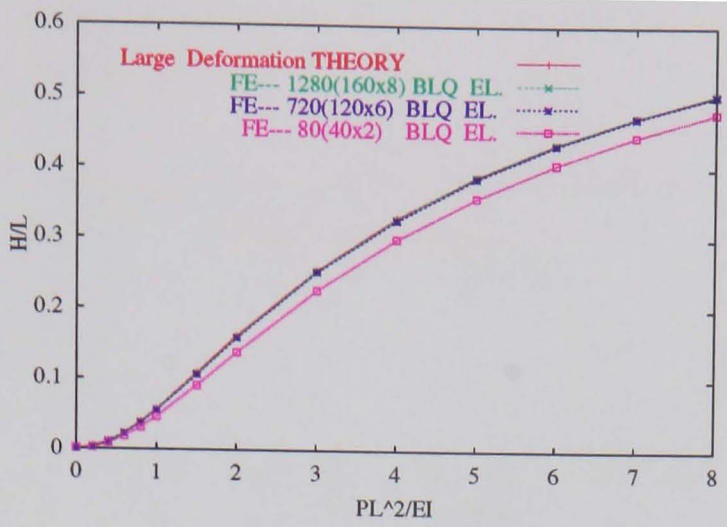

(b)- Horizontal displacement of cantilever beam(FE)

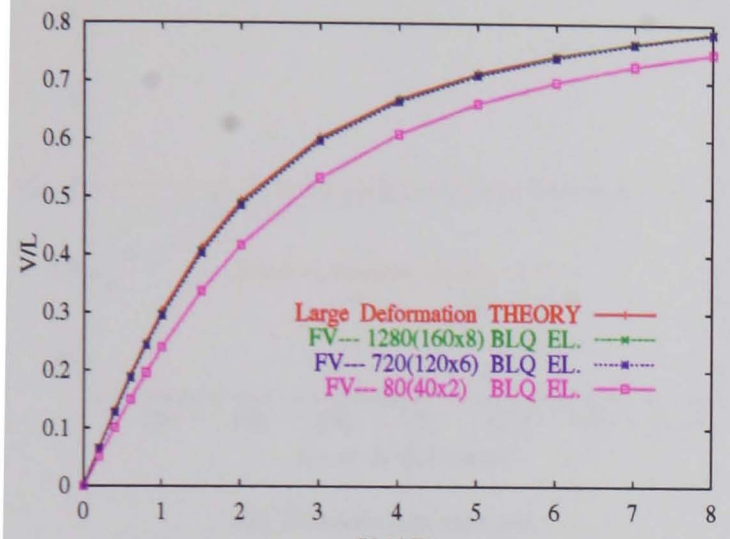

(c)- Vertical displacement of cantilever beam(FV)

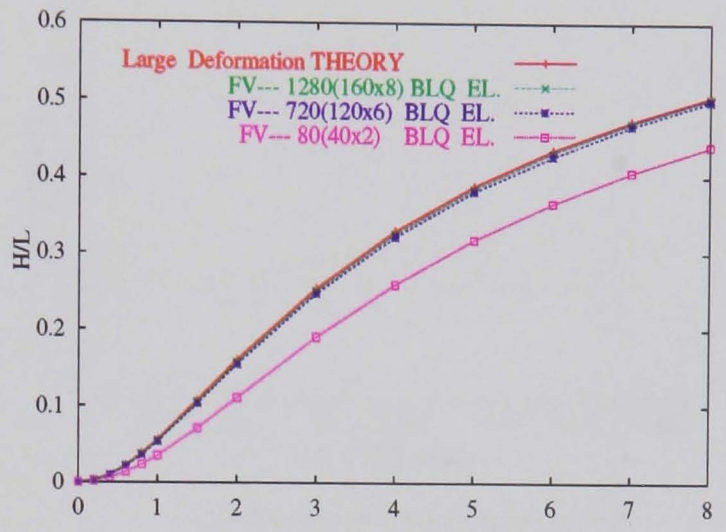

(d)- Horizontal displacement of cantilever beam(FV)

Figure 4.12: Vertical and Horizontal displacement of cantilever beam

As mentioned before, the solution of equilibrium equations in both methods is achieved through an iterative procedure based on the Newton-Ralphson method. The tolerance value in equation (4.87) was considered as 0.001 for both methods. Figure 4.13-d shows the number of iterations needed to achieve the equilibrium state in both FE and FV methods for different element numbers corresponding to load P, equal to $\frac{3EI}{L^2}$. As this figure shows, there is no significant difference in iteration numbers, just one or two more iterations in FV method was needed. Figure 4.15 presents the comparison of FEM and the FVM's results by using the BLQ and the

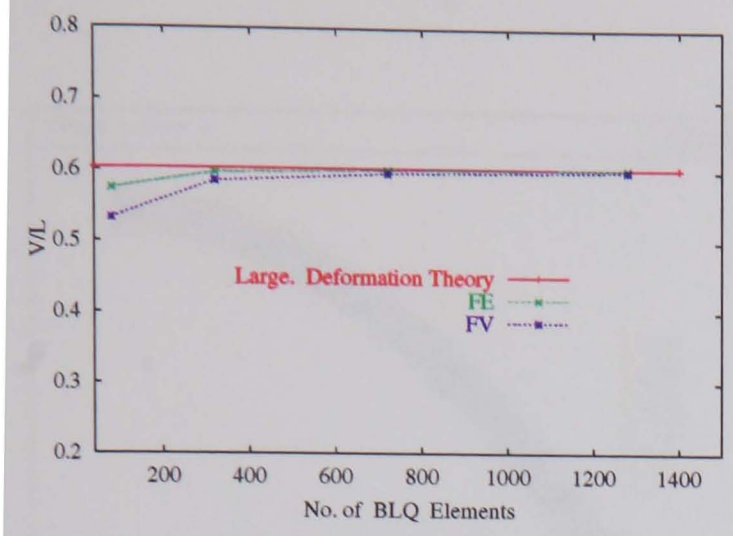

(a)-Vertical displacement

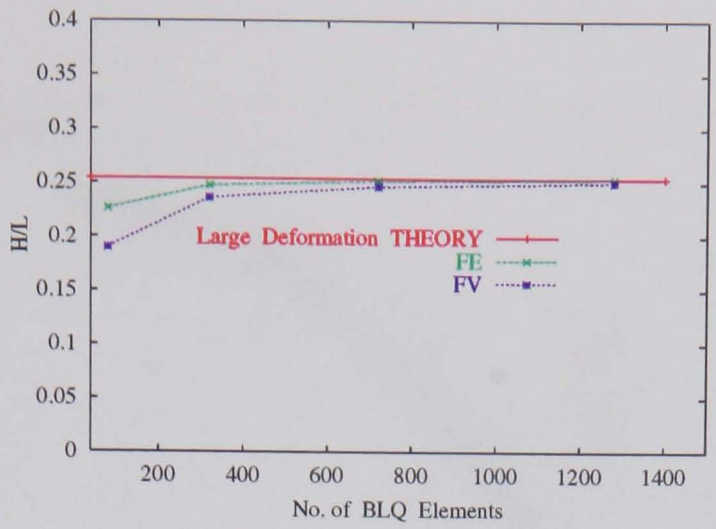

(b)-Horizontal displacement

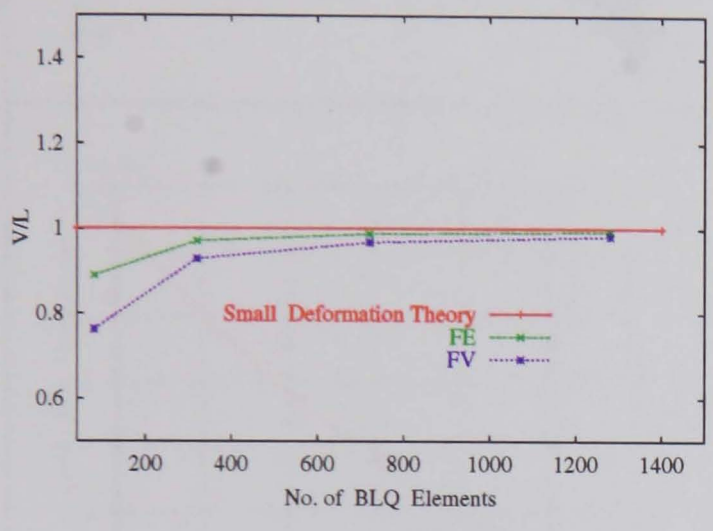

(c)-Vertical displacement

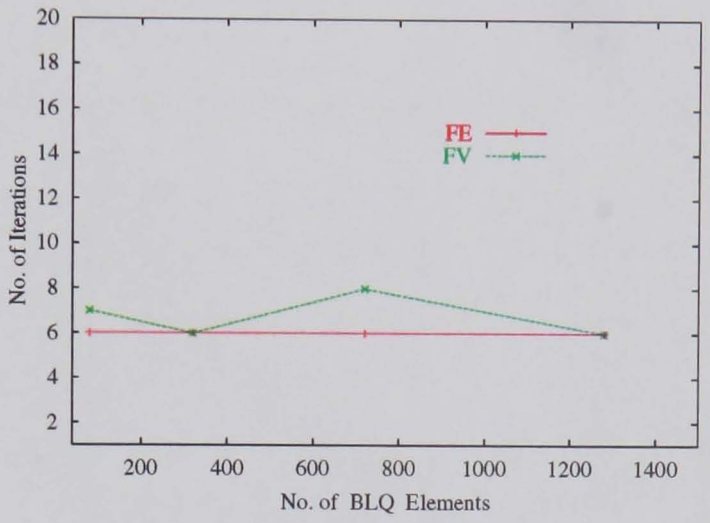

(d)-Number of iteration in FE and FV

Figure 4.13: Normalised vertical and horizontal displacement of cantilever beam ($\frac{PL^2}{EI} = 3$)

CST elements. It shows the FVM and FEM's result are the same for CST elements , as analytical discussion in section 4.4.2 demonstrated. It can be seen that for BLQ element, the result is more accurate than the CST element result.

Table (4.1) shows the total CPU times spent for the solution procedures using the different methods and the different element types. The contents of table (4.1), correspond to the applied load p, equal to $\frac{3EI}{L^2}$. The tests were carried out on a Dec Alpha work station. Conjugate gradient solver was used in both FE and FV methods. As it can be seen, the total CPU time of FV procedure for CST element is approximately two times that of FE procedure and for BLQ element there is no much differences.

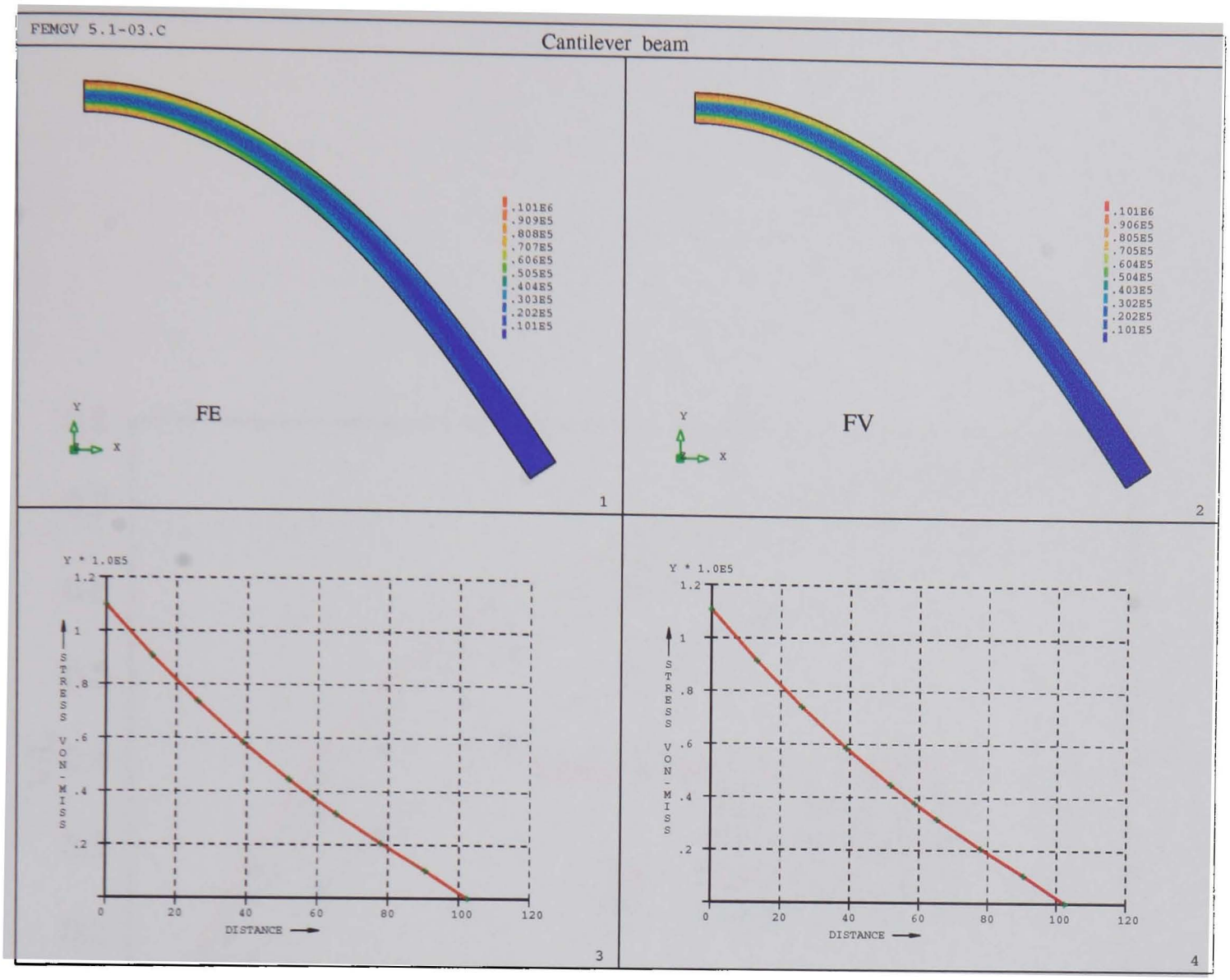

Figure 4.14: Von-Mises stress

$\frac{PL^2}{EI}$ =3 Tolerance=0.001 $\frac{V}{L}$ =0.603 (Theory result)

Element type	CPU time(Sec)		Normalised vertical displacement ($\frac{V}{L}$)		Error(%)	
	FE M	FVM	FEM	FVM	FEM	FVM
BLQ(1280)	40	49	0.603	0.600	0.0	0.5
CST(1280x2)	42	79	0.591	0.591	2	2

Table 4.1: CPU time comparison

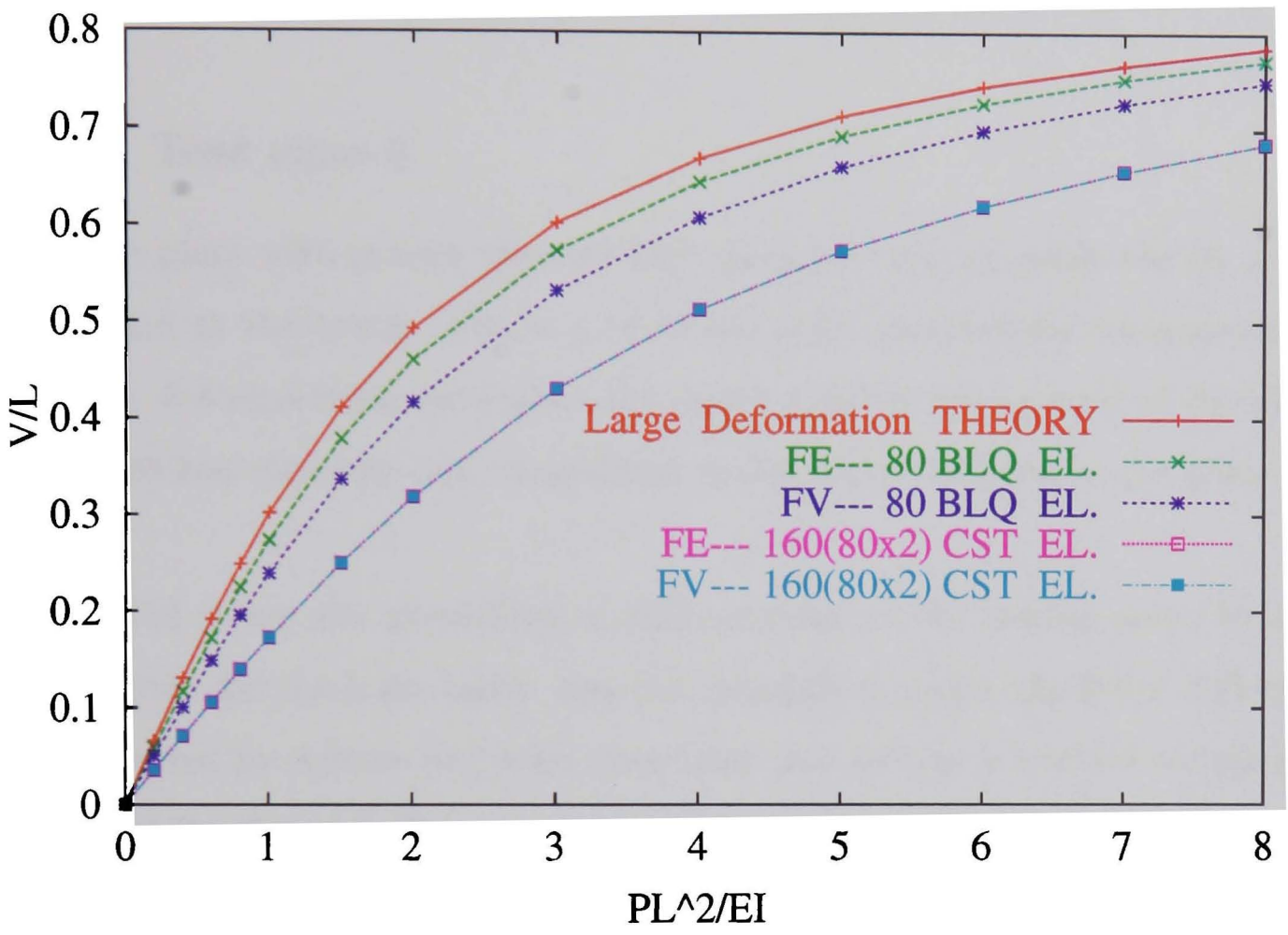

Figure 4.15: Normalised vertical displacement of cantilever beam ($\frac{PL^2}{EI} = 3$)

In the case of CST element, in FV the set up time of system matrices (e.g. global stiffness matrix, unbalance force vector, equation (4.60)) is higher than that in FE method. This is due to each individual element is visited three times where in FE just one visit is enough for providing element information for calculation of element contributions in system matrices. In linear elastic analysis may be it has a minor effect but in the GNL analysis where system matrices are updated during iterations, e.g. Newton-Ralphson procedure, it is a major issue in terms of CPU time.

4.5.3 Test case-3

A square plate with simple support and clamped support subjected to a concentrated load at the centre (Figure 4.16-b) has been analysed for its large deflection response. 8-noded brick elements were used to model one quarter of the plate. In both cases two elements were considered through the thickness of the plate.

Figure 4.16 shows the prediction of displacement at the loaded point by FE and FV methods for the both cases. For the clamped support, the finite difference results reported by Adotte [64] have been used as a reference and for simple support one, ANSYS software's [65] results have been used.

It is obvious that modelling of a plate by brick element, is inefficient and impractical [56], because the discretization would have to be very fine for a reasonably accurate solution, however, Figures 4.16-a and 4.16-c show that FE and FV converge to the reference solution but not very fast. It has to be mentioned in Figure 4.16-a ANSYS' results are based on using the shell elements and are stable after converging as it is expectful.

4.5.4 Test case-4

Figure 4.17-a shows a uniformly loaded column. The column like previous test case was discretized with 8-noded brick elements. The aim of this test was to compare the FEM and the FVM capabilities for the three dimensional analysis of axial loading case. In Figures 4.17-b and 4.18 the capability of the FVM for prediction of displacement, stress and strain is compared with the FE method. The Figures show good accuracy in FV method.

4.6 Closure

A cell vertex based finite volume formulation was developed for the analysis of geometrically nonlinear problems based on Lagrangian approach. The results have revealed that similar to the small deformation analysis, the accuracy of CV-FV method is promising. This study, accompanied by previous works on implementation of CV-FV procedure in the simulation of material nonlinearity problems by Taylor *et al.*. [66] shows that CV-FV method can be considered as a candidate for industrial process analysis (e.g. forging, metal forming, ...). Further work in this research reveals more capability of the CV-FV method in particular and finite volume method in general, for solid mechanics problems and multiphysics problems analysis.

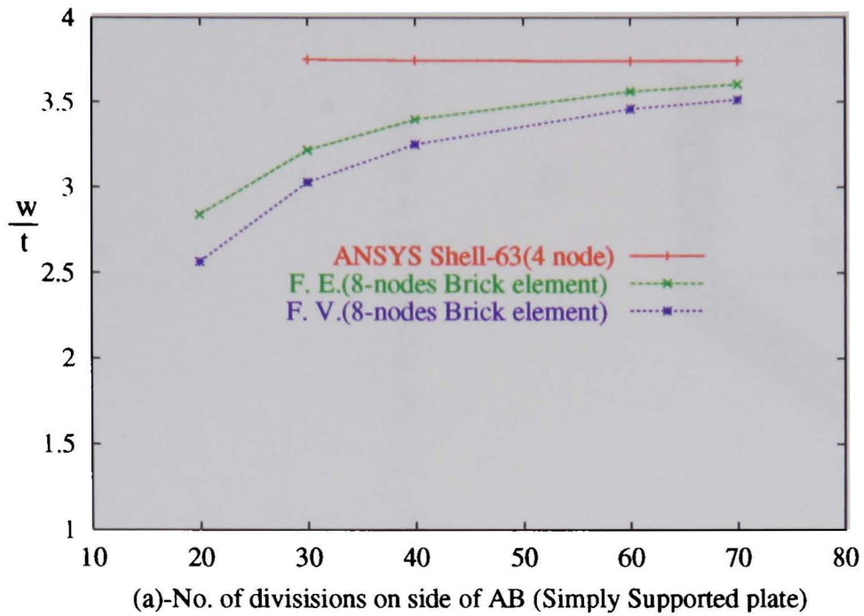

(a)-No. of divisisions on side of AB (Simply Supported plate)

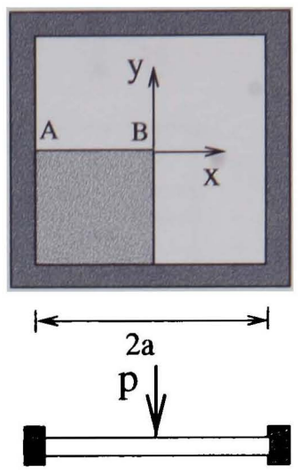

E=Young's modulus=1E+07 psi

v=Poisson ratio=0.3

t=plate thickness=.0.12 inch

w=displacement of centre of plate

2a=24 inch

$$D=\frac{Et^3}{12(1-v^2)}$$

$$\frac{Pa^2}{Dt}=800$$

(b)

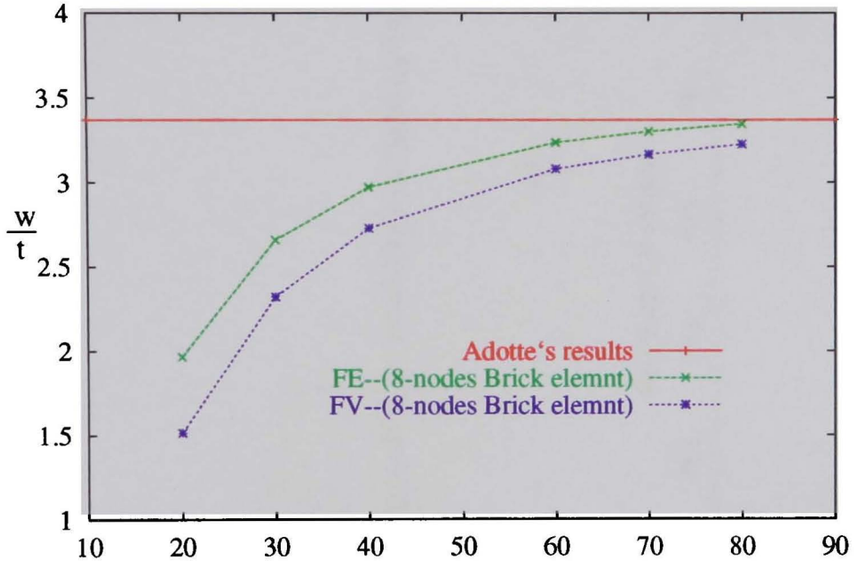

(c)-No. of divisisions on side of AB (Clamped plate)

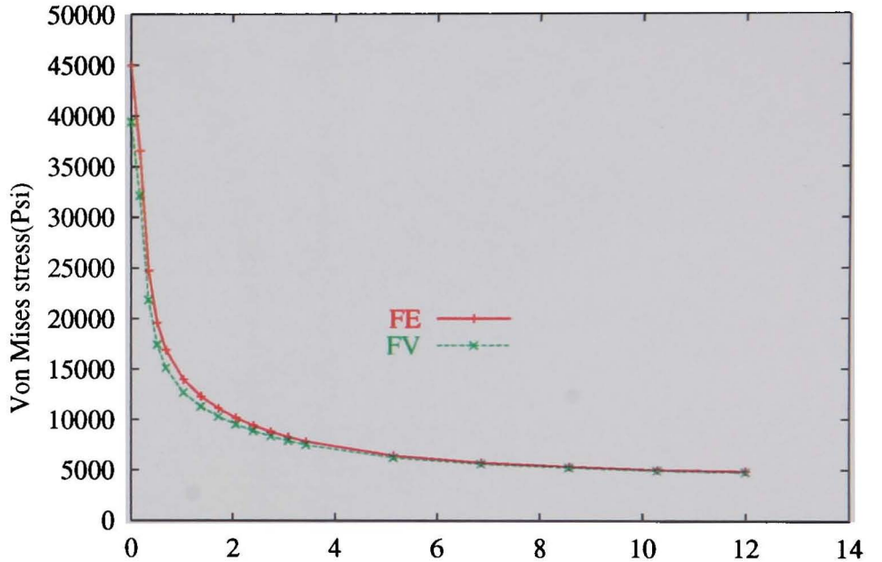

(d)-Distance along side of AB(on mid-plane of simply supported plate)

Figure 4.16: Square plate subjected to a concentrated load at the centre

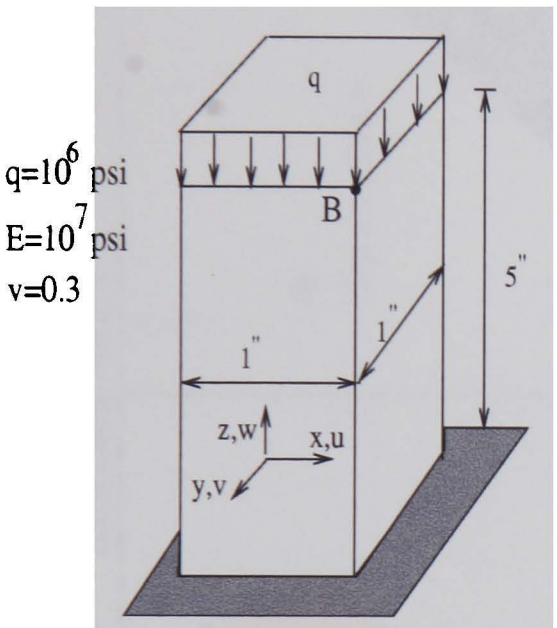

(a)

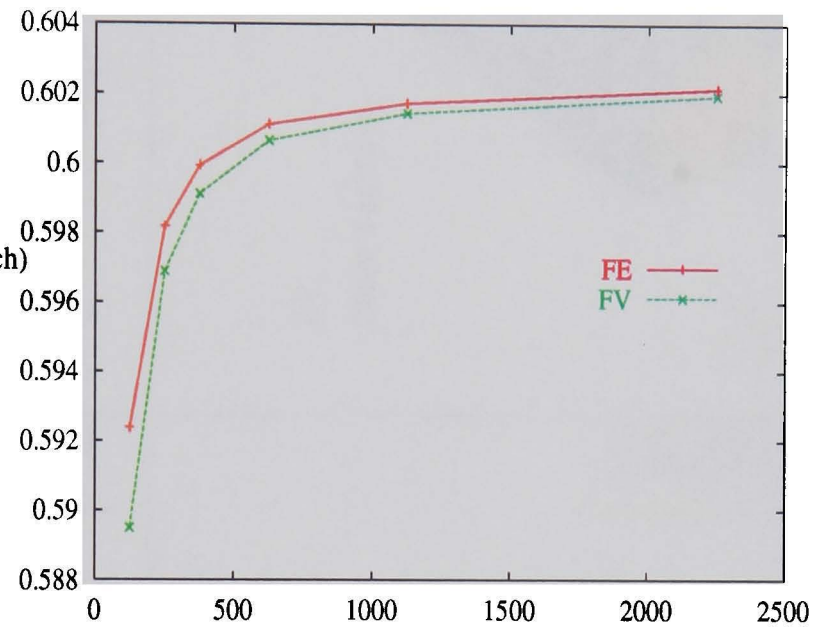

(b)

Figure 4.17: (a)-Uniform loaded column, (b)-Vertical displacement of corner B

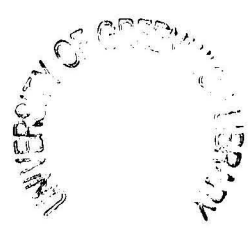

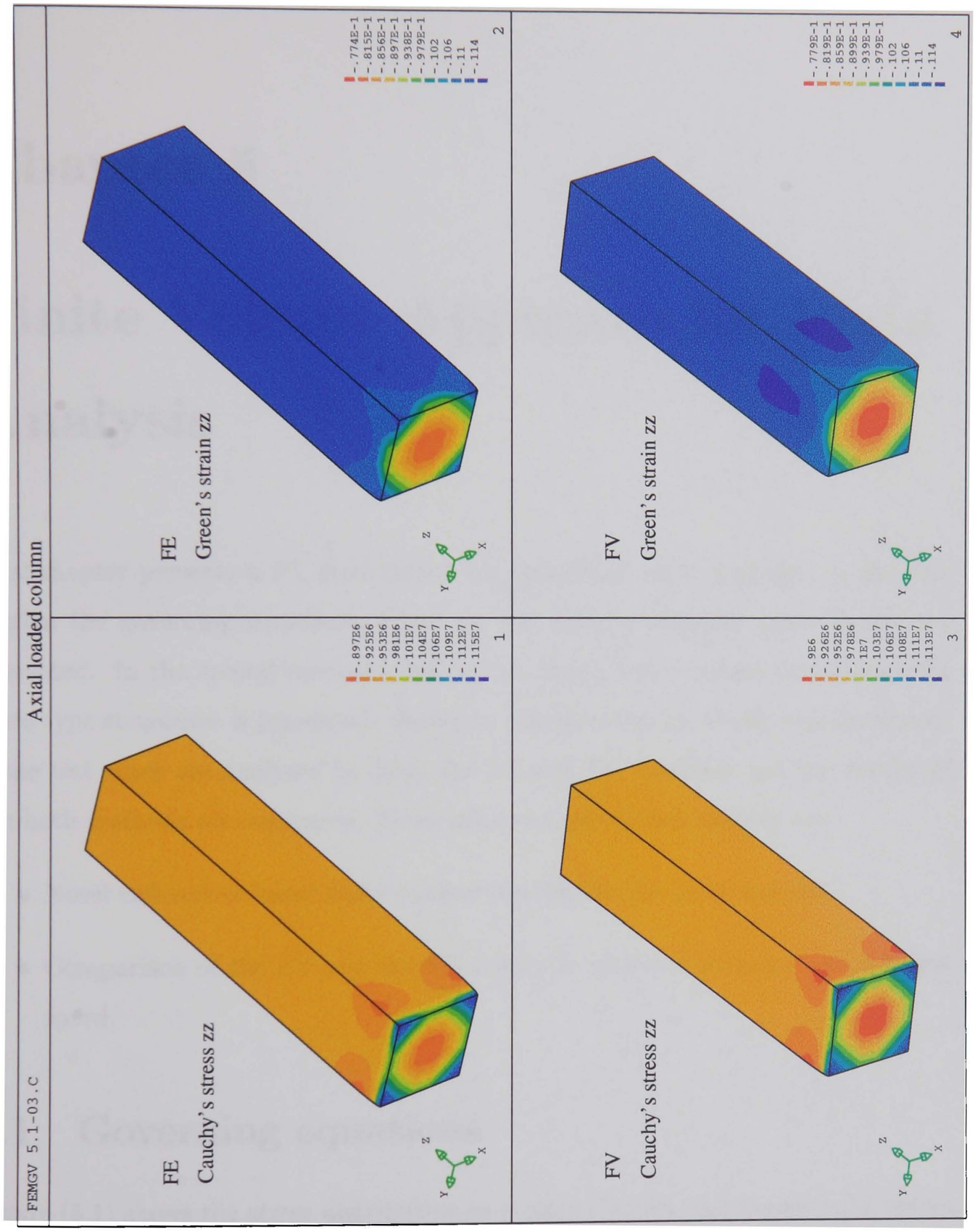

Figure 4.18: Development of stress and strain in column

Chapter 5

Finite Volume Approach for Plate Analysis

This chapter presents a FV formulation for thin/thick plate analysis. In the first section the governing equations, based on the Reissner/Mindlin plate theory are presented. In the second section a cell vertex based finite volume formulation for plate type structures is presented. Based on this formulation a code was developed. Some test cases are analysed by both the FE and FV methods and the results of the both methods are compared. Novel achievements of this chapter are:

- Novel cell-vertex based finite volume formulation for plate analysis.
- Comparison of the FV and the FE results in terms of accuracy and solution speed.

5.1 Governing equations

Figure (5.1) shows the stress distribution in a plate element and Figure 5.2-a shows shear forces and bending moments as resultant of these stresses. With reference to Figure 5.2-b and assumptions in Reissner/Mindlin plate theory and the small displacement bending theory the displacement components at a point of plate are:

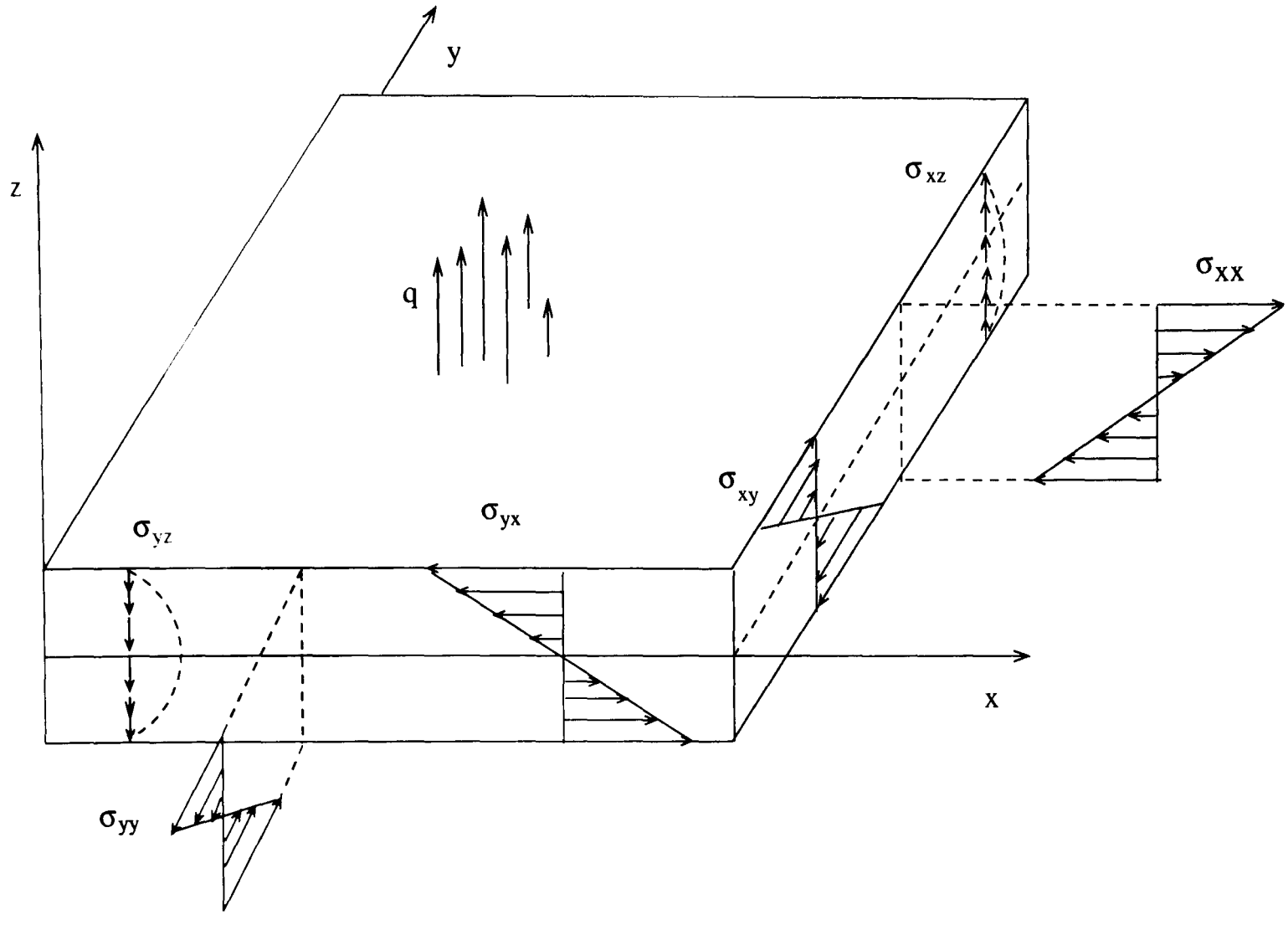

Figure 5.1: Stress distribution in plate

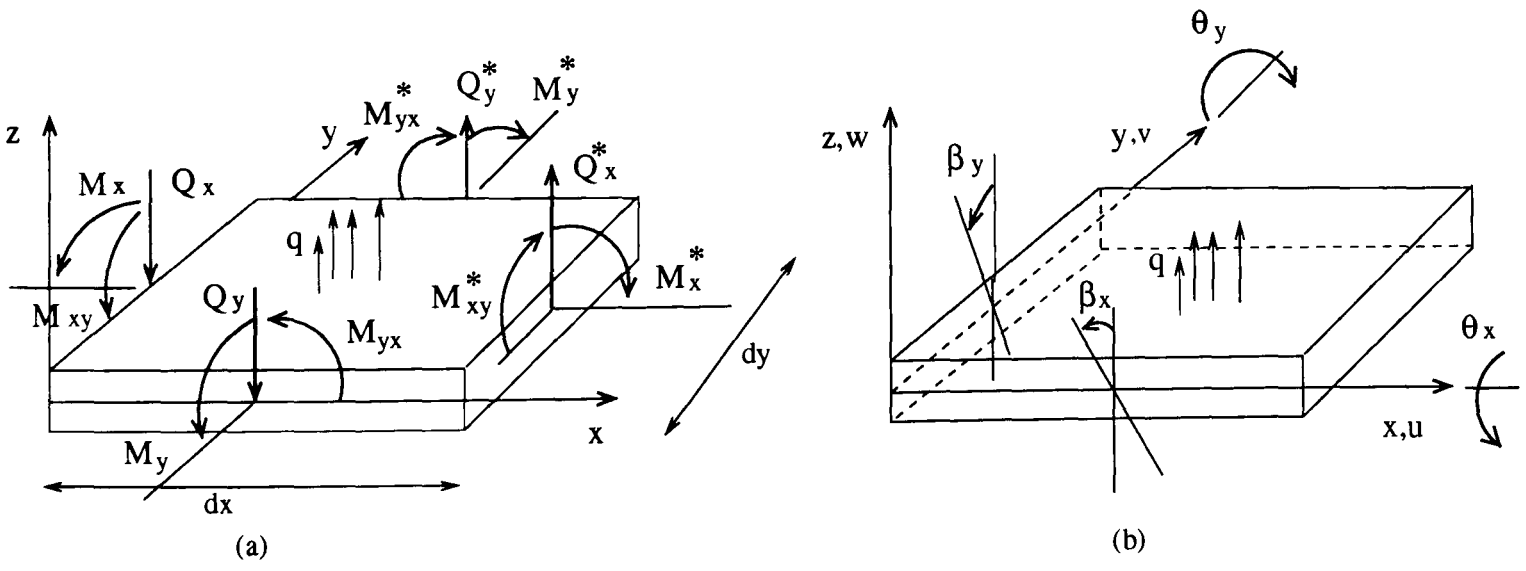

Figure 5.2: Moment, shear force and section rotation positive convention

$$u = -z\beta_x(x,y) \qquad v = -z\beta_y(x,y) \qquad w = w(x,y) \tag{5.1}$$

Where w is the transverse displacement and β_x and β_y are the rotations of the normal of the mid-plane in the xz and yz planes, respectively. It is instructive to note that the Kirchhoff plate theory excludes shear deformations in the plate, hence, without shear effects equation (5.1) can be expressed as: $\beta_x = \frac{\partial w}{\partial x}$ and $\beta_y = \frac{\partial w}{\partial y}$. The bending strains $\epsilon_{xx}, \epsilon_{yy}, \epsilon_{xy}$ vary linearly through the plate thickness and are given by the curvatures of the plate as:

$$\begin{bmatrix} \epsilon_{xx} \\ \epsilon_{yy} \\ \gamma_{xy} \end{bmatrix} = \begin{bmatrix} \frac{\partial u}{\partial x} \\ \frac{\partial v}{\partial y} \\ \frac{\partial u}{\partial y} + \frac{\partial v}{\partial x} \end{bmatrix} = -z \begin{bmatrix} \frac{\partial \beta_x}{\partial x} \\ \frac{\partial \beta_y}{\partial y} \\ \frac{\partial \beta_x}{\partial y} + \frac{\partial \beta_y}{\partial x} \end{bmatrix} \tag{5.2}$$

The governing equations of thick and thin plates can be obtained by writing the equilibrium equations of applied forces and stress resultant forces acting on the mid-plane of the plate:

$$\sum F_z = 0$$

$$\sum M_x = 0 \tag{5.3}$$

$$\sum M_y = 0$$

The first equation expresses the equilibrium of forces in the z direction and the last two equations express equilibrium of moments about x and y axes respectively. By omitting the in-plain behaviour (membrane action) and with reference to the illustrated sign convention in Figure 5.2-a, the equilibrium equation (5.3) can be expressed in matrix form as:

$$\begin{bmatrix} 0 & 0 & 0 \\ 0 & \frac{\partial}{\partial y} & \frac{\partial}{\partial x} \\ \frac{\partial}{\partial x} & 0 & \frac{\partial}{\partial y} \end{bmatrix} \begin{bmatrix} M_x \\ M_y \\ M_{xy} \end{bmatrix} - \begin{bmatrix} \frac{\partial}{\partial x} & \frac{\partial}{\partial y} \\ 1 & 0 \\ 0 & 1 \end{bmatrix} \begin{bmatrix} Q_x \\ Q_y \end{bmatrix} = \begin{bmatrix} q \\ 0 \\ 0 \end{bmatrix} \tag{5.4}$$

Where Q_x and Q_y are shear forces per unit length and M_x,M_y and M_{xy} are bending moments per unit length at every point of the mid-plane of the plate. It is notable in Figure 5.2-a, the star quantities are defined as follows:

$$\begin{aligned} M_x^* &= M_x + \frac{\partial M_x}{\partial x} dx \\ M_{xy}^* &= M_{xy} + \frac{\partial M_{xy}}{\partial x} dx \\ Q_x^* &= Q_x + \frac{\partial Q_x}{\partial x} dx \\ M_y^* &= M_y + \frac{\partial M_y}{\partial y} dy \\ M_{yx}^* &= M_{yx} + \frac{\partial M_{yx}}{\partial y} dy \\ Q_y^* &= Q_y + \frac{\partial Q_y}{\partial y} dy \end{aligned} \tag{5.5}$$

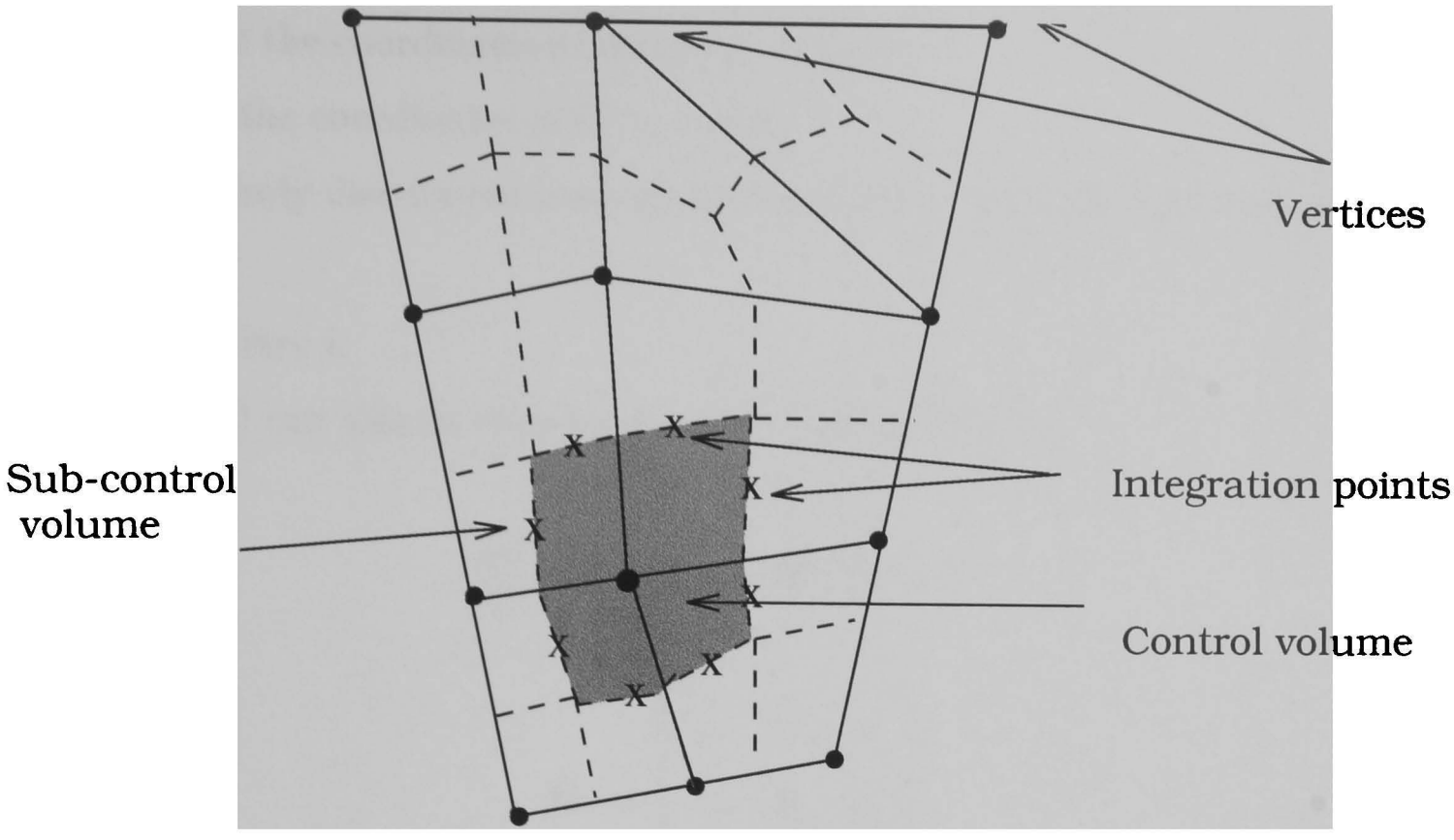

Figure 5.3: Control volume around a computational node

5.2 Finite volume formulation for plate analysis

Equation (5.4) illustrates equilibrium at the continuum level and for obtaining the discretized equation which expresses the equilibrium of a plate control volume at the discretized level, equation (5.3) can be applied. By applying the three equilibrium equations, i.e. (5.3), for any control volume in Figure 5.3 the matrix form of the equilibrium equations (5.3) can be expressed as:

$$\sum_i \begin{bmatrix} 0 & 0 & 0 \\ 0 & n_y^i & n_x^i \\ n_x^i & 0 & n_y^i \end{bmatrix} \begin{bmatrix} M_x^i \\ M_y^i \\ M_{xy}^i \end{bmatrix} l_i - \sum_i \begin{bmatrix} n_x^i & n_y^i \\ y_m^i - y_o^c & y_m^i - y_o^c \\ x_m^i - x_o^c & x_m^i - x_o^c \end{bmatrix} \begin{bmatrix} Q_x^i \\ Q_y^i \end{bmatrix} l_i = \begin{bmatrix} qA_c \\ 0 \\ 0 \end{bmatrix} \tag{5.6}$$

Where:

n_x^i and n_y^i are cosine directions of outward normal of face i.

x_m^i and y_m^i are the coordinates of midpoint of face i.

x_o^c and y_o^c are the coordinates of CV's centre.

q is the uniformly distributed load applied on the CV with the mid-surface area of A_c.

l_i is length of face i.

Equation (5.6) can also be expressed in its compact form as:

$$\sum_i \mathbf{H}_i \mathbf{M}_i l_i - \sum_i \mathbf{H}_i^* \mathbf{Q}_i l_i = \mathbf{P}_i \tag{5.7}$$

Where:

$$\mathbf{H}_i = \begin{bmatrix} 0 & 0 & 0 \\ 0 & n_y^i & n_x^i \\ n_x^i & 0 & n_y^i \end{bmatrix}$$

$$\mathbf{M}_i = \begin{bmatrix} M_x^i \\ M_y^i \\ M_{xy}^i \end{bmatrix}$$

$$\mathbf{H}_i^* = \begin{bmatrix} n_x^i & n_y^i \\ y_m^i - y_o^c & y_m^i - y_o^c \\ x_m^i - x_o^c & x_m^i - x_o^c \end{bmatrix}$$

$$\mathbf{Q}_i = \begin{bmatrix} Q_x^i \\ Q_y^i \end{bmatrix}$$

$$\mathbf{P}_i = \begin{bmatrix} qA_c \\ 0 \\ 0 \end{bmatrix}$$

All moments and shear forces are measured per unit length and their variation on the control volume faces, is assumed uniform. By applying the Reissner/Mindlin plate theory and with reference to Figure 5.2-(b), moments and shear forces at each

point in the CV can be expressed [56] as :

$$\mathbf{M} = -\mathbf{D}^* \boldsymbol{\epsilon}^* \tag{5.8}$$

$$\mathbf{Q} = G^* \boldsymbol{\gamma} \tag{5.9}$$

where:

$$\mathbf{M} = \begin{bmatrix} M_x \\ M_y \\ M_{xy} \end{bmatrix} \tag{5.10}$$

$$\mathbf{Q} = \begin{bmatrix} Q_x \\ Q_y \end{bmatrix} \tag{5.11}$$

$$\boldsymbol{\gamma} = \begin{bmatrix} \gamma_{xz} \\ \gamma_{yz} \end{bmatrix} \tag{5.12}$$

$$\mathbf{D}^* = \frac{Et^3}{12(1-\nu^2)} \begin{bmatrix} 1 & \nu & 0 \\ \nu & 1 & 0 \\ 0 & 0 & \frac{1-\nu}{2} \end{bmatrix} \quad , \quad G^* = kGt \tag{5.13}$$

$$\boldsymbol{\epsilon}^* = \begin{bmatrix} \frac{\partial \beta_x}{\partial x} \\ \\ \frac{\partial \beta_y}{\partial y} \\ \\ \frac{\partial \beta_x}{\partial y} + \frac{\partial \beta_y}{\partial x} \end{bmatrix} \tag{5.14}$$

By use of equation(5.1) the lateral shear deformations can be expressed as:

$$\boldsymbol{\gamma} = \begin{bmatrix} \frac{\partial w}{\partial x} - \beta_x \\ \\ \frac{\partial w}{\partial y} - \beta_y \end{bmatrix} \tag{5.15}$$

Where E is Young's modulus, G is shear modulus, t is thickness of the CV, k is the

lateral shear correction factor [67]. The transverse displacement , w, and section rotations, β_x and β_y, can be interpolated [23] as:

$$w = \sum_{j=1}^{r} N_j w_j \qquad -\beta_x = \theta_y = \sum_{j=1}^{r} N_j \theta_y^j \qquad \beta_y = \theta_x = \sum_{j=1}^{r} N_j \theta_x^j \tag{5.16}$$

where w_j, θ_x^j and θ_y^j are the nodal values of the unknown variables w,θ_x and θ_y respectively, N_j is the interpolation function and r is the number of element nodes. By using the mentioned interpolations, the curvature $\boldsymbol{\epsilon}^*$ and transverse shear strains $\boldsymbol{\gamma}$ can be calculated in terms of nodal unknown variables as:

$$\boldsymbol{\epsilon}^* = \mathbf{B}_b \bar{\mathbf{u}} \tag{5.17}$$

$$\boldsymbol{\gamma} = \mathbf{B}_s \bar{\mathbf{u}} \tag{5.18}$$

Where for four-noded quadrilateral elements we have:

$$\bar{\mathbf{u}} = \begin{bmatrix} w_1 & \theta_x^1 & \theta_y^1 & \dots & \theta_y^4 \end{bmatrix}^T \tag{5.19}$$

$$\mathbf{B}_b = \begin{bmatrix} \mathbf{B}_b^1 & \mathbf{B}_b^2 & \mathbf{B}_b^3 & \mathbf{B}_b^4 \end{bmatrix} \tag{5.20}$$

$$\mathbf{B}_s = \begin{bmatrix} \mathbf{B}_s^1 & \mathbf{B}_s^2 & \mathbf{B}_s^3 & \mathbf{B}_s^4 \end{bmatrix} \tag{5.21}$$

For typical node i:

$$\mathbf{B}_b^i = \begin{bmatrix} 0 & 0 & -\frac{\partial N_i}{\partial x} \\ 0 & \frac{\partial N_i}{\partial y} & 0 \\ 0 & \frac{\partial N_i}{\partial x} & -\frac{\partial N_i}{\partial y} \end{bmatrix} \tag{5.22}$$

$$\mathbf{B}_s^i = \begin{bmatrix} \frac{\partial N_i}{\partial x} & 0 & N_i \\ \frac{\partial N_i}{\partial y} & -N_i & 0 \end{bmatrix} \tag{5.23}$$

By substituting equations(5.17) and equation(5.18) into equation (5.8) and finally in equation (5.7), we have:

$$(-\sum \mathbf{H}\mathbf{D}^*\mathbf{B}_b l_i - \sum \mathbf{H}^* G^* \mathbf{B}_s l_i)\bar{\mathbf{u}} = \mathbf{P}_i \tag{5.24}$$

Or in compact form:

$$\mathbf{K}^c\bar{\mathbf{u}} = \mathbf{P}_i \tag{5.25}$$

$$K^c = K_b^c + K_s^c \tag{5.26}$$

$$\mathbf{K}_b^c = -\sum \mathbf{H}\mathbf{D}^*\mathbf{B}_b l_i \qquad , \qquad \mathbf{K}_s^c = -\sum \mathbf{H}^* G^* \mathbf{B}_s l_i \tag{5.27}$$

Where $\mathbf{K}_b^c$ is the bending stiffness matrix and $\mathbf{K}_s^c$ is the shear stiffness matrix.

5.3 Boundary conditions and solution of the discretized equilibrium equations

Due to the consistence of the presented discretization method with the FEM, where CV's are overlayed on the FE mesh, the boundary conditions can be applied as usual as FE method. The dependent variables like displacement over a CV are approximated by using the element shape functions. By assembling the CV's stiffness matrix , $\boldsymbol{K}^c$, the global stiffness matrix of system, $\mathbf{K}$, can be arranged as usual and the final equilibrium equation is given by:

$$\boldsymbol{K}\bar{\boldsymbol{u}} = \boldsymbol{P} \tag{5.28}$$

where $\bar{\boldsymbol{u}}$ is nodal displacement and rotations and $\mathbf{P}$ is the generalized force vector which contains force and moments. The stiffness matrix of a control volume, $\mathbf{K}^c$, is evaluated at respective integration points. The above equation can be solved by bi-conjugate gradient method which we have used here.

5.4 Results and discussion

To validate the presented FV formulation four test cases were studied. In all cases the FV results were compared with results of an in-house finite element code. The

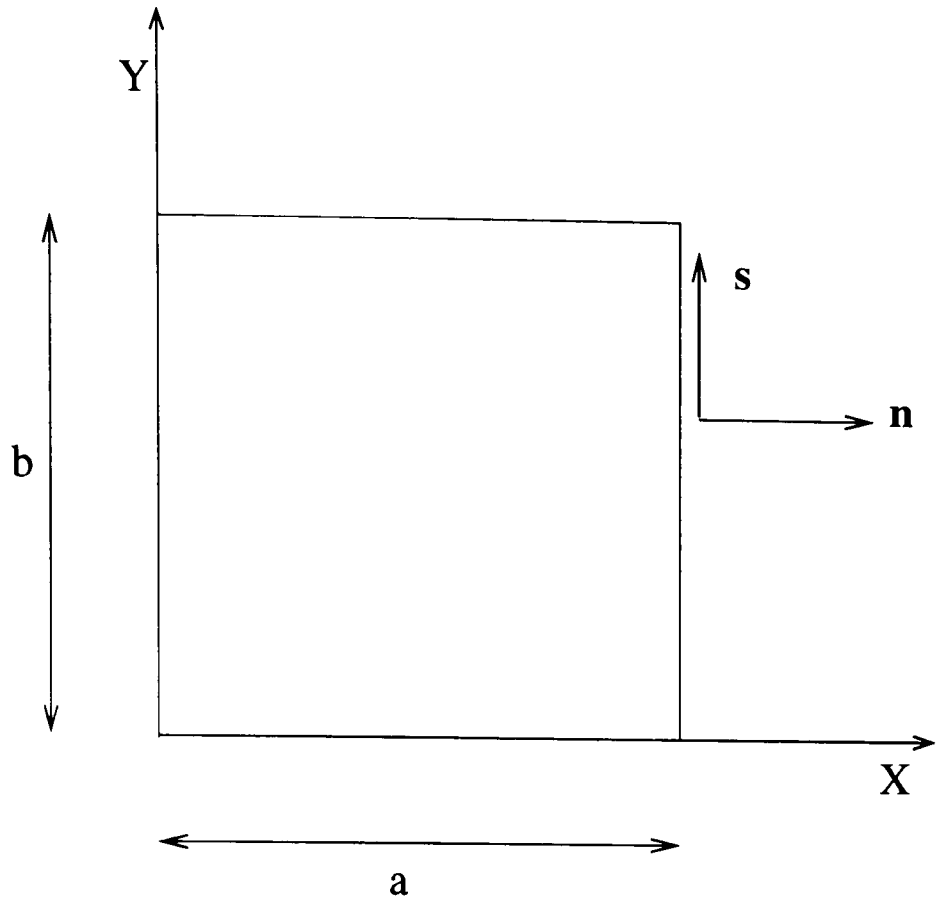

Figure 5.4: Tangential and normal directions at boundary of a plate

first test case was a tip loaded cantilever beam and the second was a simply supported plate under the uniform lateral load with moderate thickness. In the third and fourth test cases a thin plate was analysed where for test case three a uniformly distributed load, and in test case four a concentrated central load was considered for the analysis. Two types of boundary conditions are usually considered in plate analysis. (with reference to Figure 5.4), these are:

- For a simply supported boundary, the following conditions can be considered:

  1) $w = \theta_n$=0 or:

  2) w=0

- For a clamped boundary the following conditions can be considered:

  1) $w = \theta_s = \theta_n$=0 or:

  2) $w = \theta_n$=0

Where θ_s and θ_n are section rotations at the boundary about the tangent vector s

and normal vector **n** respectively. A boundary condition of type (1) is called a hard boundary condition and a boundary condition of type (2) is called a soft boundary condition. In the following tests the hard boundary conditions have been assumed, otherwise it is explicitly mentioned.

5.4.1 Test case-1

A cantilever beam with concentrated load at the end was discretized by four-noded quadrilateral(BLQ) elements. The height of the beam was considered as the thickness of the plate elements. The ratio of height to length of the beam, λ, was 0.01, see Figure 5.5. The end vertical displacement was predicted using both FE and FV. For FE the full numerical integration (in this case two gauss points in each direction) was used. The results were compared with the analytical results which were taken from Timoshenko [68] with poisson's ratio equal to 0.3. As Figure 5.5 shows, the FV results converge to the analytical solution much quicker than FE predictions. This due to the nature of Reissner based formulation and by decreasing the parameter λ the element "locks" for FE methods. The locking problem of FEM in thin plate analysis is well known and is caused by the imposition of the constraints $\gamma_{xz} = \gamma_{yz} = 0$ by the shear strain energy terms in the total potential energy when the limiting thin plate situation is approached. The shear strain energy terms may be interpreted as penalty functions, which force the shear strains to equal zero as λ is reduced. The imposition of these constraints leads to the deterioration of the stiffness matrix and overstiff results are obtained [67].

By applying techniques like the reduced integration method [69], selective integration method [70], and mixed interpolation method [23, 56], the shear locking problem can be removed. The four-noded quadrilateral element, MITC4 which was developed by Bathe *et al.* [23, 56] based on the mixed interpolation methods, has been used in our FE code. By applying such enhanced quadrilateral element, FE

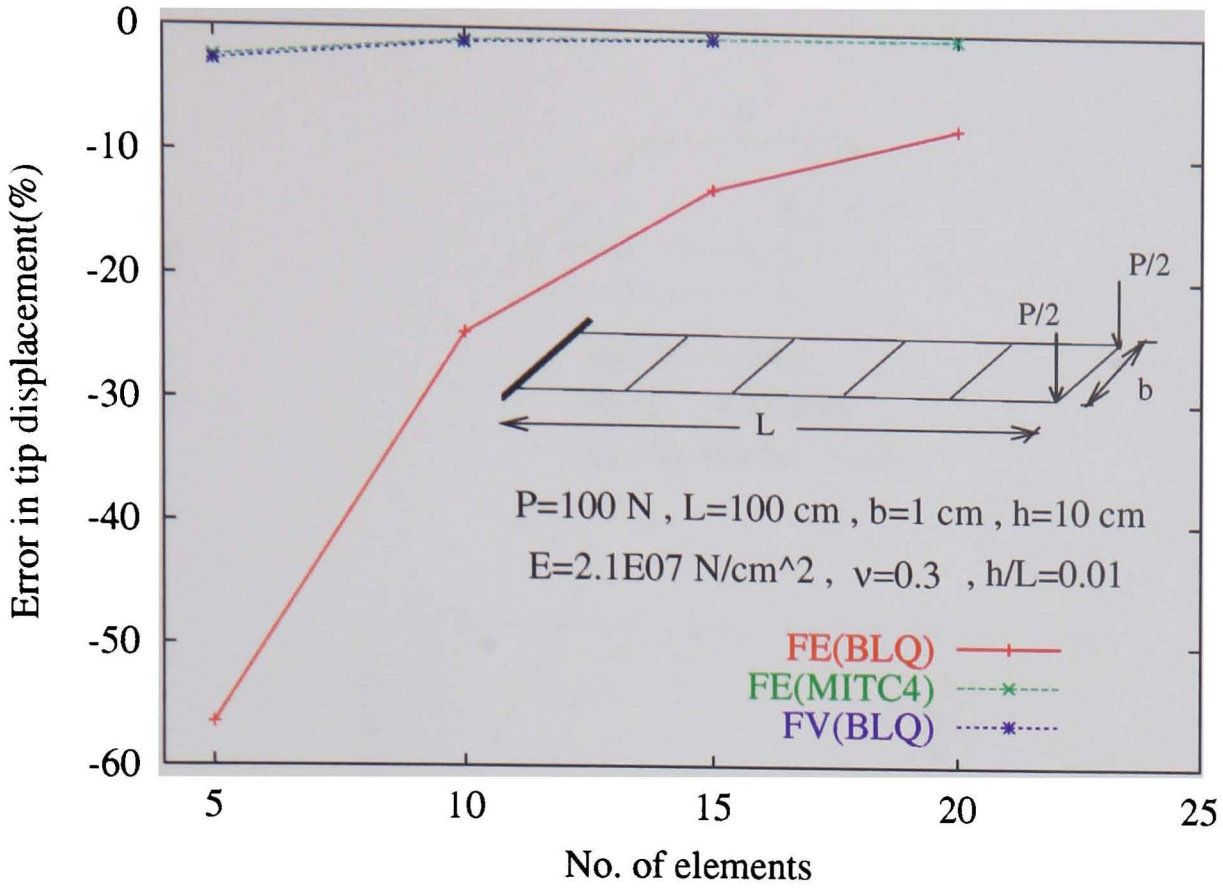

Figure 5.5: Tip concentrate loaded cantilever beam is modelled by plate element

results improved highly and coincided with FV results. In this analysis, the FV did not show such shear locking due to the nature of its integration technique, where there is one integration point correspondence to each side of the element. This type of the integration is the form that the reduced integration method seeks to achieve in FE method.

5.4.2 Test case-2

For the second test case, a moderately thick($\lambda = 0.01$) square simply supported plate was analysed by FE and FV where the central displacement and bending moment have been compared with the analytical results [71]. In this case, as Figures 5.6-a and 5.6-b demonstrated, the FE method with BLQ elements converges to the analytical results slowly for both central bending moment and displacement, but by applying MITC4 elements, the FE is marginally faster than FV. Table (5.1) shows the total CPU times spent for the solution procedures and accuracy of the results for

(a)

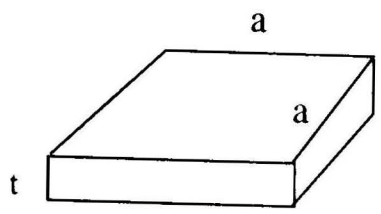

a=2 m , t=0.20 m

t/a=0.1 , q=100 MPa

E=210E03 MPa , ν=0.3

(b)

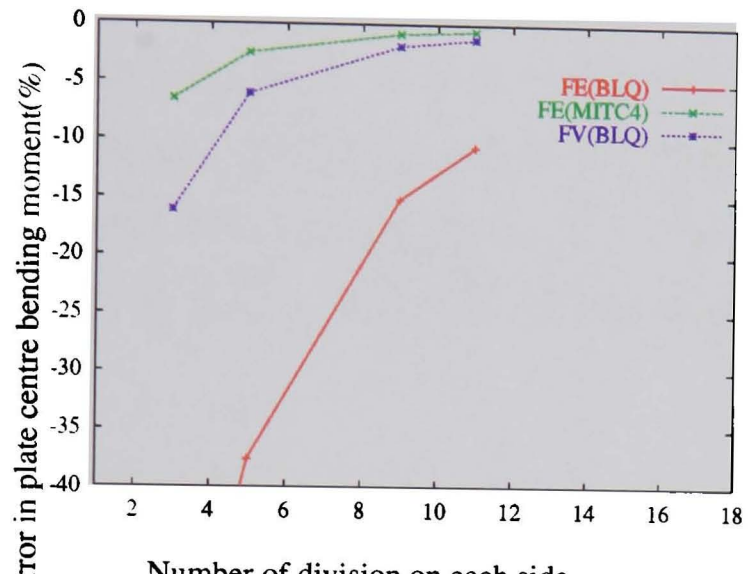

(c)

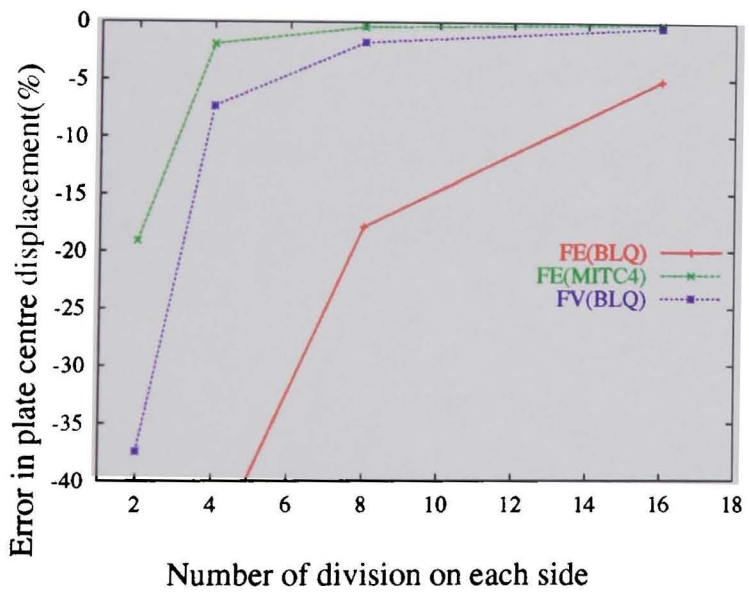

Figure 5.6: Comparison of FE and FV results for a moderately thick, simply supported plate.

Test case-2. analytical result for central displacement=4.443 E-2 m(Mindlin plate theory)

Methods	FE(BLQ)	FE(MITC4)	FV(BLQ)
CPU Time(sec)	8	8	6
Central displacement(m)	4.215E-2	4.439E-2	4.424E-2
Error(%)	-5.14	-0.09	-0.42

Table 5.1: Comparison of CPU time and accuracy for FE and FV

the different methods. The regular mesh allows us to use conjugate gradient solver for the FV method. The results in table (5.1), are based on 16 equal divisions on each side of the plate. The tests were carried out on a SUN SPARC20 work station. No much difference can be seen between the total spent CPU times for the different methods. But the accuracy of the FE method with MITC4 element is marginally higher.

5.4.3 Test case-3

By reducing the thickness of previous test case to $\lambda = 0.001$ and considering both simply and clamped boundary conditions, FE with BLQ elements fails in predicting the accurate central displacement, but the FV method has no problem and converges to the analytical result as FE with MITC4 is able to do. Figure 5.7-a and 5.7-b show the results which were compared with the analytical results based on Kirshhoff plate theory [68].

5.4.4 Test case-4

By changing the uniform load in test case 3 to a central concentrated load the same incapability for FE with BLQ elements exists. As Figures 5.8-a and 5.8-b show FV and FE with MITC4 can predict the accurate results with both simple and clamped boundary conditions.

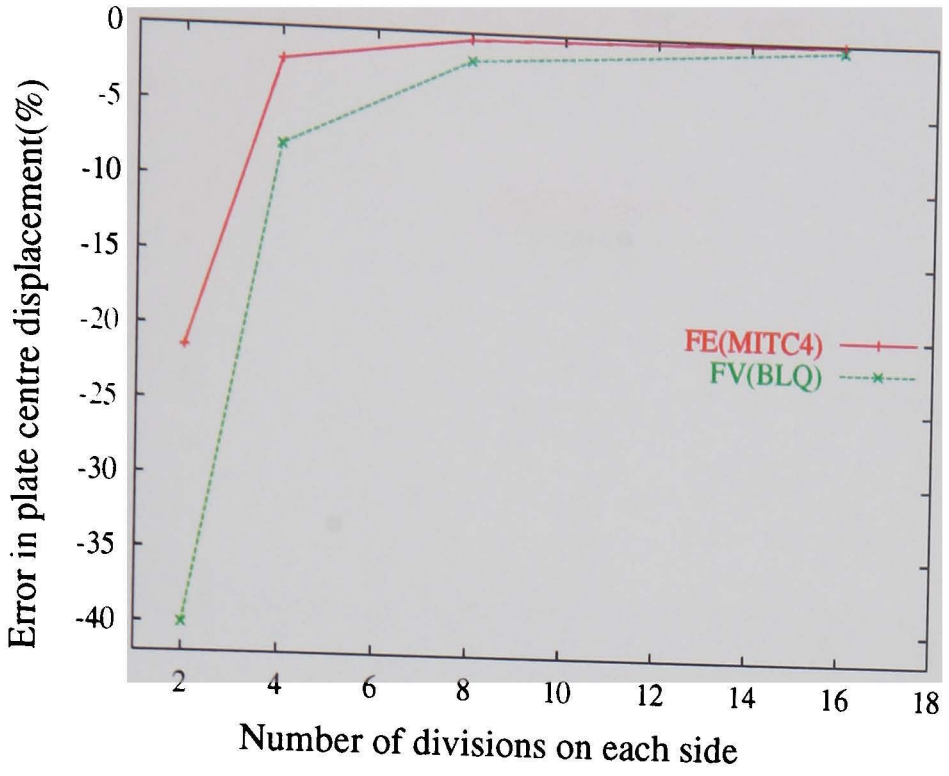

(a)-Simply supported plate(q=1 Pa)

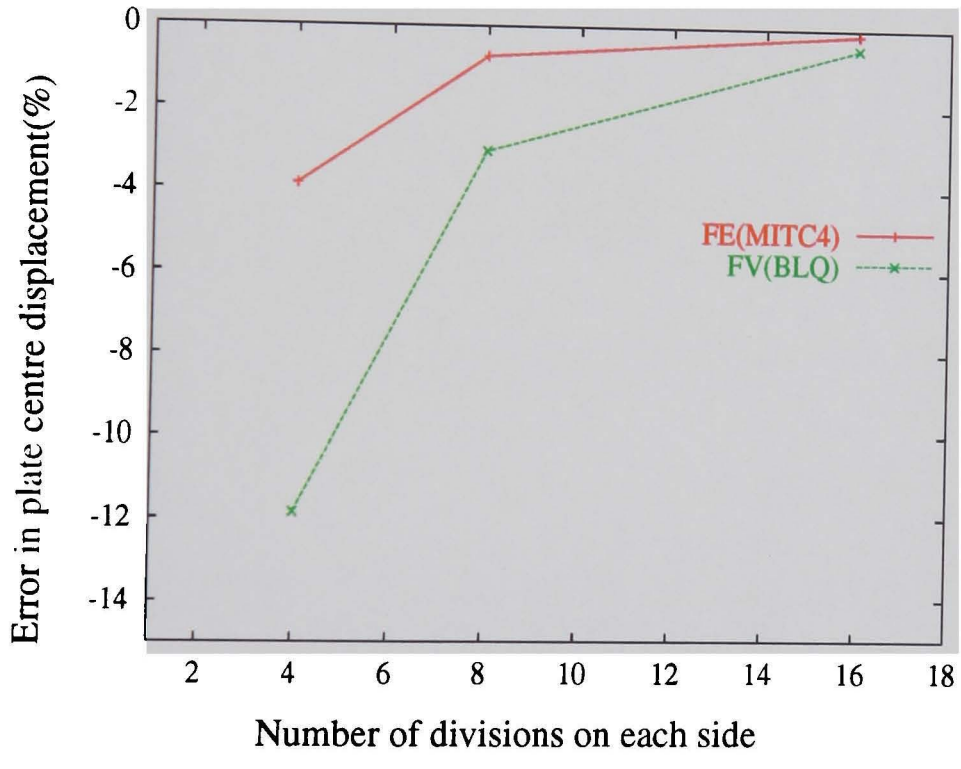

(b)-Clamped plate(q=3.1 Pa)

Figure 5.7: Error in displacement prediction of a uniformly loaded thin plate , $\lambda = 0.001$.

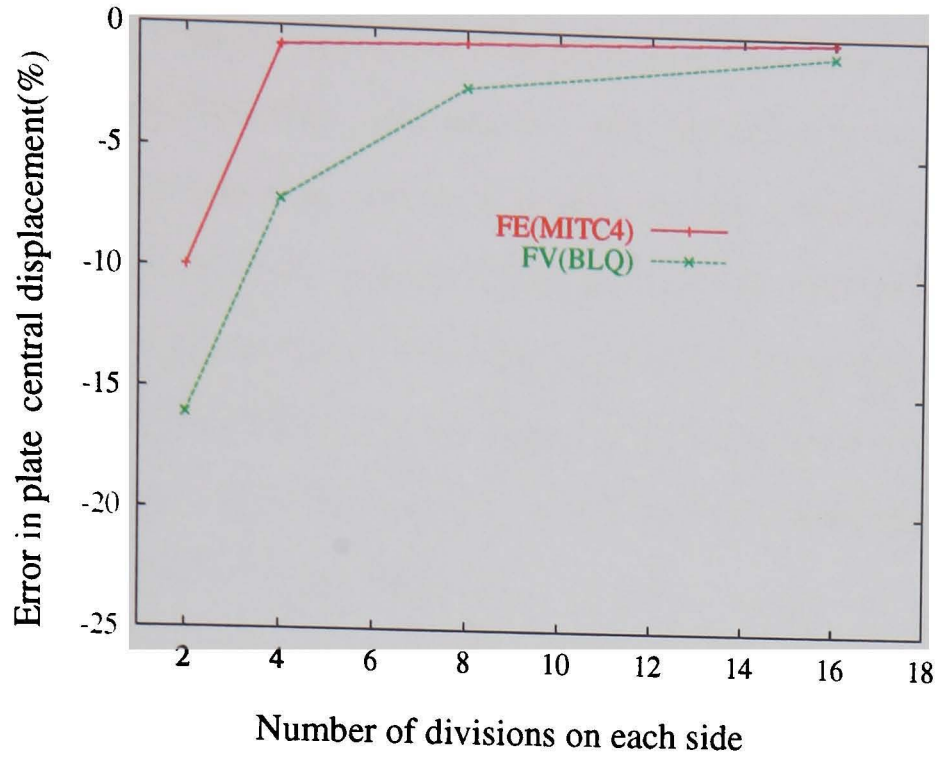

(a)-Simply supported plate(P=1.5 N)

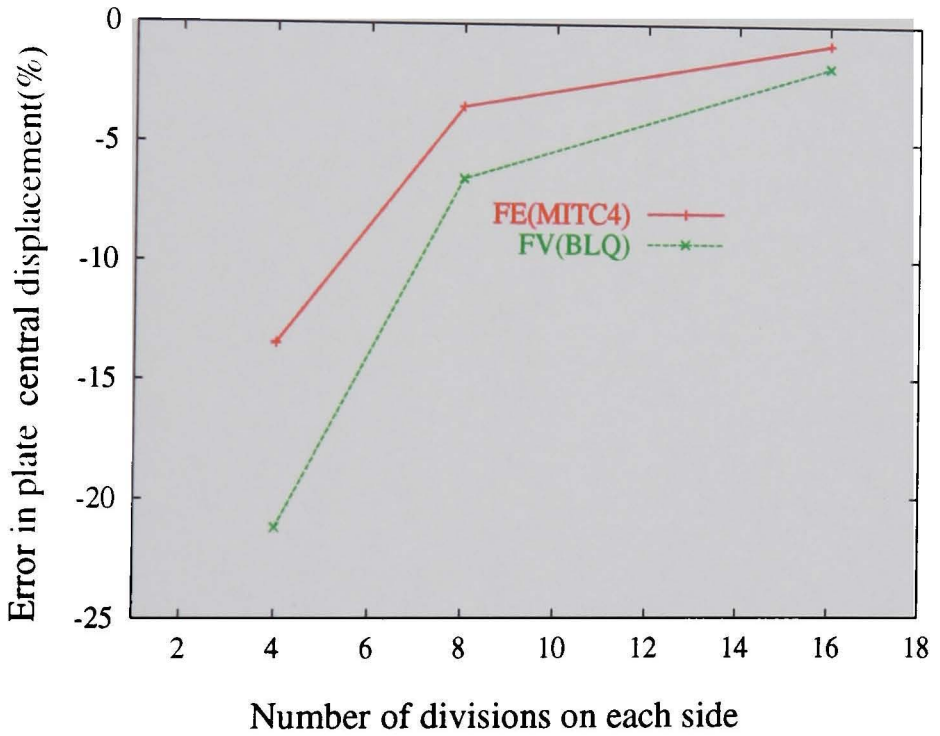

(b)-Clamped plate(P=3.1 N)

Figure 5.8: Error in displacement prediction of a thin plate under the central concentrated load, $\lambda = 0.001$.

5.5 Closure

A vertex based finite volume approach was developed for the thick and thin plate analysis. The Reissner/Mindlin plate theory was implemented in the formulation. The method is easy in concept which is based on the expressing the equilibrium state of an individual control volume with compatible deformations at common nodes with neighbouring volumes. The results present, in moderately thin and very thin plate analysis, FEM suffers from locking problem while FVM is free of locking matters. It is another profitable feature of FVM and encourages researchers for more investigation of FVM capabilities.

Chapter 6

CFD Approach for the Analysis of Solid Mechanics and Thermally Coupled Stress-Flow Problems

The aim of this chapter is to provide a solid mechanics formulation using a CFD framework to solve problems involving compressible and incompressible or nearly incompressible materials. In this approach, in addition to displacement components, the pressure field is also considered as an unknown variable. The development of this type of formulations is encouraged by the following:

- The usual displacement formulation becomes unstable when Poisson's ratio is larger than 0.4.
- The similarity between the fluid flow equations and solid mechanics equations may enable modifications to an available CFD code for solving solid mechanics problems.
- This formulation provides a foundation for analysing problems involving stress-flow-thermal (multiphysics) effects using a single code.

Multiphysics problems can be found in the following applications:

- Temperature-stress problems arising in unevenly heated piping systems.
- Thermal stress problems arising in electronics equipment (flow, heat, stress).
- Thermal and mechanical stress problems in the blades, disks and combustors of power generation equipment (flow, heat, stress).
- Residual stress problems in casting and other forming processes (flow, phase change, temperature, stress).

The discussion in this chapter is limited to small elastic strains. The similarities between the solid equations and fluid flow equations will be addressed and then some necessary modifications will be discussed to achieve a desired technique for solution of solid mechanics and multiphysics problems. The PHYSICA [33] code, a cell centred finite volume(CC-FV) based CFD code, is used to undertake this analysis. The modifications to this CFD code will be demonstrated with test cases for stress only problems and multiphysics problems. The novelty of the work in this chapter is:

- Solving the stress equations in a CFD code.
- Technique involves small changes to current CFD environment.
- Comparison between this single solver with traditional 2-solver approach for a number of problems.
- Extension of structured multiphysics solver [32] to unstructured meshes.

6.1 A CFD algorithm for solid problems

The solid stress need to be calculated in design when material shows incompressibile or compressible behaviour. Although this can be dealt with using the available techniques in solid mechanics field (i.e., finite element method), the solid and fluid equations are similar and it can be shown that a CFD approach can also be applied

for the analysis. The idea is, when the solid momentum equations including of constitutive equations are formulated with displacements as the dependent variables, their form is almost identical with those governing the velocities field in the fluid flow equations. Therefore, displacements can be computed for solids and velocity for fluids [72]. The next section highlights the similarities between solid and fluid equations.

6.1.1 Fluid momentum equations

Based on Newton's second law the momentum equations in three dimensions are [73]:

$$\begin{aligned}
\frac{\partial(\rho v_x)}{\partial t} + div(\rho v_x \mathbf{v}) &= -\frac{\partial p}{\partial x} + \frac{\partial \sigma_{xx}}{\partial x} + \frac{\partial \sigma_{yx}}{\partial y} + \frac{\partial \sigma_{zx}}{\partial z} + S_{Mx} \\
\frac{\partial(\rho v_y)}{\partial t} + div(\rho v_y \mathbf{v}) &= -\frac{\partial p}{\partial y} + \frac{\partial \sigma_{xy}}{\partial x} + \frac{\partial \sigma_{yy}}{\partial y} + \frac{\partial \sigma_{zy}}{\partial z} + S_{My} \\
\frac{\partial(\rho v_z)}{\partial t} + div(\rho v_z \mathbf{v}) &= -\frac{\partial p}{\partial z} + \frac{\partial \sigma_{xz}}{\partial x} + \frac{\partial \sigma_{yz}}{\partial y} + \frac{\partial \sigma_{zz}}{\partial z} + S_{Mz}
\end{aligned} \tag{6.1}$$

Where:

$\mathbf{v}$ is velocity vector.

v_i is component of velocity vector $\mathbf{v}$ on i direction.

ρ is density.

p is pressure.

σ_{ij} is viscous stress component (deviatoric stress component) which acts in the j direction on a surface where its normal is in the i direction.

S_{Mi} is the source term which includes contributions due to body forces in the i direction.

6.1.2 Navier-stokes equations for a Newtonian fluid

The momentum equations contain further unknowns of the viscous stress components σ_{ij}. In many fluid flows the viscous stresses can be expressed as functions of

the local deformation rate (or strain rate). In three dimensional flows the local rate of deformation is composed of the linear deformation rate and the volumetric deformation rate. The rate of linear deformation of a fluid element has nine components in three dimensions, six of which are independent in isotropic fluids [74]:

$$
\begin{aligned}
e_{xx} &= \frac{\partial v_x}{\partial x} \\
e_{yy} &= \frac{\partial v_y}{\partial y} \\
e_{zz} &= \frac{\partial v_z}{\partial z} \\
e_{xy} = e_{yx} &= \frac{1}{2}\left(\frac{\partial v_x}{\partial y} + \frac{\partial v_y}{\partial x}\right) \\
e_{xz} = e_{zx} &= \frac{1}{2}\left(\frac{\partial v_x}{\partial z} + \frac{\partial v_z}{\partial x}\right) \\
e_{yz} = e_{zy} &= \frac{1}{2}\left(\frac{\partial v_y}{\partial z} + \frac{\partial v_z}{\partial y}\right)
\end{aligned}
\tag{6.2}
$$

The volumetric deformation is given by:

$$
\frac{\partial v_x}{\partial x} + \frac{\partial v_y}{\partial y} + \frac{\partial v_z}{\partial z} = div\mathbf{v} \tag{6.3}
$$

In a Newtonian fluid the viscous stresses are proportional to the rate of deformation. The three-dimensional form of Newton's law of viscosity for compressible flows involves two constants of proportionality:

$$
\begin{aligned}
\sigma_{xx} &= 2\mu e_{xx} + \lambda div\mathbf{v} \\
\sigma_{yy} &= 2\mu e_{yy} + \lambda div\mathbf{v} \\
\sigma_{zz} &= 2\mu e_{zz} + \lambda div\mathbf{v} \\
\sigma_{xy} &= \sigma_{yx} = \mu e_{xy} \\
\sigma_{xz} &= \sigma_{zx} = \mu e_{xz} \\
\sigma_{yz} &= \sigma_{zy} = \mu e_{yz}
\end{aligned}
\tag{6.4}
$$

Where μ is dynamic viscosity and λ is the second constant. Not much is known about λ, because its effect is small in practice. For gases $\lambda = -\frac{2}{3}\mu$ is a good approximation in practice [74]. For an incompressible fluid, $div\mathbf{v}$ =0 so in the above constitutive equations there will be just μ as the constant. Substitution of the above constitutive equations, (6.2), (6.3) and (6.4) into equation (6.1) yields the so called Navier-Stokes equations:

$$\begin{aligned}
\frac{\partial(\rho v_x)}{\partial t} + div(\rho v_x \mathbf{v}) &= -\frac{\partial p}{\partial x} + \frac{\partial}{\partial x}[2\mu\frac{\partial v_x}{\partial x} + \lambda div\mathbf{v}] + \frac{\partial}{\partial y}[\mu(\frac{\partial v_y}{\partial x} + \frac{\partial v_x}{\partial y})] + \\
&\quad \frac{\partial}{\partial z}[\mu(\frac{\partial v_x}{\partial z} + \frac{\partial v_z}{\partial x})] + S_{Mx} \\
\frac{\partial(\rho v_y)}{\partial t} + div(\rho v_y \mathbf{v}) &= -\frac{\partial p}{\partial y} + \frac{\partial}{\partial x}[\mu(\frac{\partial v_x}{\partial y} + \frac{\partial v_y}{\partial x})] + \frac{\partial}{\partial y}[2\mu\frac{\partial v_y}{\partial y} + \lambda div\mathbf{v}] + \\
&\quad \frac{\partial}{\partial z}[\mu(\frac{\partial v_y}{\partial z} + \frac{\partial v_z}{\partial y})] + S_{My} \qquad (6.5) \\
\frac{\partial(\rho v_z)}{\partial t} + div(\rho v_z \mathbf{v}) &= -\frac{\partial p}{\partial z} + \frac{\partial}{\partial x}[\mu(\frac{\partial v_x}{\partial z} + \frac{\partial v_z}{\partial x})] + \frac{\partial}{\partial y}[\mu(\frac{\partial v_y}{\partial z} + \frac{\partial v_z}{\partial y})] + \\
&\quad \frac{\partial}{\partial z}[2\mu\frac{\partial v_z}{\partial z} + \lambda div\mathbf{v}] + S_{Mz}
\end{aligned}$$

Rearranging the viscous stress terms is possible as follows. In x momentum equation:

$$\frac{\partial}{\partial x}[2\mu\frac{\partial v_x}{\partial x} + \lambda div\mathbf{v}] + \frac{\partial}{\partial y}[\mu(\frac{\partial v_y}{\partial x} + \frac{\partial v_x}{\partial y})] + \frac{\partial}{\partial z}[\mu(\frac{\partial v_x}{\partial z} + \frac{\partial v_z}{\partial x})] =$$

$$[\frac{\partial}{\partial x}(\mu\frac{\partial v_x}{\partial x}) + \frac{\partial}{\partial y}(\mu\frac{\partial v_x}{\partial y}) + \frac{\partial}{\partial z}(\mu\frac{\partial v_x}{\partial z})] +$$

$$[\frac{\partial}{\partial x}(\mu\frac{\partial v_x}{\partial x}) + \frac{\partial}{\partial x}(\mu\frac{\partial v_y}{\partial y}) + \frac{\partial}{\partial x}(\mu\frac{\partial v_z}{\partial z})] + \frac{\partial}{\partial x}(\lambda div\mathbf{v}) =$$

$$div(\mu grad v_x) + \frac{\partial}{\partial x}(\mu div\mathbf{v}) + \frac{\partial}{\partial x}(\lambda div\mathbf{v}) = div(\mu grad v_x) + \frac{\partial}{\partial x}(\mu + \lambda) div\mathbf{v}$$

The same procedures is possible for momentum equations in y and z directions. The final form of momentum equations are:

$$\frac{\partial(\rho v_x)}{\partial t} + div(\rho v_x \mathbf{v}) = -\frac{\partial}{\partial x}[p - (\mu + \lambda) div\mathbf{v}] + div(\mu grad v_x) + S_{Mx}$$

$$\frac{\partial(\rho v_y)}{\partial t} + div(\rho v_y \mathbf{v}) = -\frac{\partial}{\partial y}[p - (\mu + \lambda) div \mathbf{v}] + div(\mu grad v_y) + S_{My} \tag{6.6}$$

$$\frac{\partial(\rho v_z)}{\partial t} + div(\rho v_z \mathbf{v}) = -\frac{\partial}{\partial z}[p - (\mu + \lambda) div \mathbf{v}] + div(\mu grad v_z) + S_{Mz}$$

By neglecting the convection terms at low Reynolds number flow, the steady state form of the above equations is:

$$\begin{aligned} -\frac{\partial}{\partial x}[p - (\mu + \lambda) div \mathbf{v}] + div(\mu grad v_x) + S_{Mx} = 0 \\ -\frac{\partial}{\partial y}[p - (\mu + \lambda) div \mathbf{v}] + div(\mu grad v_y) + S_{My} = 0 \\ -\frac{\partial}{\partial z}[p - (\mu + \lambda) div \mathbf{v}] + div(\mu grad v_z) + S_{Mz} = 0 \end{aligned} \tag{6.7}$$

6.1.3 Fluid continuity equation

Derivation of the mass conservation equation is based on the mass balance for the fluid element."Rate of increase of mass in fluid element" should be equal to "Net rate of flow of mass into fluid element".

Mathematically. the above expression can be written as:

$$\frac{\partial \rho}{\partial t} + div(\rho \mathbf{v}) = 0 \tag{6.8}$$

6.1.4 A pressure displacement formulation for solid stress analysis

The conventional form of the momentum equations for solids in the steady state situation from the principle of static equilibrium are:

$$\begin{aligned} \frac{\partial \sigma_{xx}}{\partial x} + \frac{\partial \sigma_{yx}}{\partial y} + \frac{\partial \sigma_{zx}}{\partial z} + S_{Mx} = 0 \\ \frac{\partial \sigma_{xy}}{\partial x} + \frac{\partial \sigma_{yy}}{\partial y} + \frac{\partial \sigma_{zy}}{\partial z} + S_{My} = 0 \end{aligned} \tag{6.9}$$

$$\frac{\partial \sigma_{xz}}{\partial x} + \frac{\partial \sigma_{yz}}{\partial y} + \frac{\partial \sigma_{zz}}{\partial z} + S_{Mz} = 0$$

Where typically S_{Mx} is the source term which includes component of the body force in the x direction. Based on the linear termo-elasticity theory, stress can be related to the deformation by use of Hook's law as:

$$\sigma_{xx} = \frac{E(1-\nu)}{(1+\nu)(1-2\nu)}\{\frac{\partial u_x}{\partial x} - \alpha(T-T_r) + \frac{\nu}{1-\nu}[\frac{\partial u_y}{\partial y} - \alpha(T-T_r)] + \frac{\nu}{1-\nu}[\frac{\partial u_z}{\partial z} - \alpha(T-T_r)]\}$$

$$\sigma_{yy} = \frac{E(1-\nu)}{(1+\nu)(1-2\nu)}\{\frac{\nu}{1-\nu}[\frac{\partial u_x}{\partial x} - \alpha(T-T_r)] + \frac{\partial u_y}{\partial y} - \alpha(T-T_r) + \frac{\nu}{1-\nu}[\frac{\partial u_z}{\partial z} - \alpha(T-T_r)]\}$$

$$\sigma_{zz} = \frac{E(1-\nu)}{(1+\nu)(1-2\nu)}\{\frac{\nu}{1-\nu}[\frac{\partial u_x}{\partial x} - \alpha(T-T_r)] + \frac{\nu}{1-\nu}[\frac{\partial u_y}{\partial y} - \alpha(T-T_r)] + \frac{\partial u_z}{\partial z} - \alpha(T-T_r)\} \tag{6.10}$$

$$\sigma_{xy} = \sigma_{yx} = G(\frac{\partial u_x}{\partial y} + \frac{\partial u_y}{\partial x})$$

$$\sigma_{xz} = \sigma_{zx} = G(\frac{\partial u_x}{\partial z} + \frac{\partial u_z}{\partial x})$$

$$\sigma_{yz} = \sigma_{zy} = G(\frac{\partial u_y}{\partial z} + \frac{\partial u_z}{\partial y})$$

Where:

ν is Poisson's ratio.

G is shear modulus.

α is thermal expansion coefficient.

T is temperature.

T_r is reference temperature.

The normal stresses σ_{xx},σ_{yy} and σ_{zz} can be rearranged as:

$$\sigma_{xx} = \sigma_{av} + 2G\frac{\partial u_x}{\partial x} - \frac{2G}{3}div\mathbf{u}$$

$$\sigma_{yy} = \sigma_{av} + 2G\frac{\partial u_y}{\partial y} - \frac{2G}{3}div\mathbf{u} \tag{6.11}$$

$$\sigma_{zz} = \sigma_{av} + 2G\frac{\partial u_z}{\partial z} - \frac{2G}{3}div\mathbf{u}$$

Where σ_{av} is the mean value of the normal stresses:

$$\sigma_{av} = \frac{\sigma_{xx} + \sigma_{yy} + \sigma_{zz}}{3} = \frac{E}{3(1-2\nu)}[div\mathbf{u} - 3\alpha(T-T_r)] \tag{6.12}$$

Physically σ_{av} can be interpreted as a pressure quantity, but because of different positive sign convention for stress quantity and pressure quantity, we have:

$$p_s = -\sigma_{av} = -\frac{E}{3(1-2\nu)}[div\mathbf{u} - 3\alpha(T - T_r)] \tag{6.13}$$

Substitution of this pressure quantity into Hook's law gives:

$$\begin{aligned}
\sigma_{xx} &= -p_s + 2G\frac{\partial u_x}{\partial x} - \frac{2G}{3}div\mathbf{u} \\
\sigma_{yy} &= -p_s + 2G\frac{\partial u_y}{\partial y} - \frac{2G}{3}div\mathbf{u} \\
\sigma_{zz} &= -p_s + 2G\frac{\partial u_z}{\partial z} - \frac{2G}{3}div\mathbf{u} \\
\sigma_{xy} &= \sigma_{yx} = G(\frac{\partial u_x}{\partial y} + \frac{\partial u_y}{\partial x}) \\
\sigma_{xz} &= \sigma_{zx} = G(\frac{\partial u_x}{\partial z} + \frac{\partial u_z}{\partial x}) \\
\sigma_{yz} &= \sigma_{zy} = G(\frac{\partial u_y}{\partial z} + \frac{\partial u_z}{\partial y})
\end{aligned} \tag{6.14}$$

Finally by substituting the (6.14) into the equilibrium equations (6.9) we have:

$$\begin{aligned}
-\frac{\partial}{\partial x}(p_s - \frac{G}{3}div\mathbf{u}) + div(Ggradu_x) + S_{Mx} = 0 \\
-\frac{\partial}{\partial y}(p_s - \frac{G}{3}div\mathbf{u}) + div(Ggradu_y) + S_{My} = 0 \\
-\frac{\partial}{\partial z}(p_s - \frac{G}{3}div\mathbf{u}) + div(Ggradu_z) + S_{Mz} = 0
\end{aligned} \tag{6.15}$$

The comparison of equations (6.15) and (6.7) is instructive because it provides a key tool for the analysis of multiphysics problems where fluids and solids interact. The comparison indicates that μ corresponds to G and velocity vector $\mathbf{v}$ corresponds to displacement vector $\mathbf{u}$. By choosing the value of $\lambda = -\frac{2}{3}\mu$, in equation (6.7), the two sets of equation have completely the same form.

In the case of a termo-elastic solid, solution of the continuity equation may be avoided since the variation of density is negligible [31]. Therefore, it is reasonable

to expect to achieve the solid deformation field by solving equations (6.7), when accompanied with equation (6.13) instead of the continuity equation, which defines the relation between displacement vector $\mathbf{u}$ and pressure quantity of p_s.

Adopting the CFD software for this type of application should be done carefully, because in some CFD packages like PHYSICA, the term $(\mu + \lambda)div\mathbf{v}$ in equation (6.7) is considered to be zero. As a result of this assumption the relationship between pressure in fluid equation, (6.7) and p_s in solid equilibrium equation, (6.15) is:

$$p = p_s - \frac{G}{3} div\mathbf{u} \tag{6.16}$$

By substituting equation (6.13) into the above equation we have:

$$p = -G[\frac{1}{1-2\nu} div\mathbf{u} - \frac{2(1+\nu)}{1-2\nu}\alpha(T - T_r)] \tag{6.17}$$

Or:

$$div\mathbf{u} + \frac{1-2\nu}{G} p - 2\alpha(1+\nu)(T - T_r) = 0 \tag{6.18}$$

Now the above equations can be used with the momentum equations of (6.7) for solid stress analysis in a CFD framework.

6.2 PHYSICA

PHYSICA [33] has the capability to solve problems that involve coupled physical phenomena in three spatial dimensions and time. It may be used for computational fluid dynamics and computational solid mechanics and interactions between the two. Apart from stress calculations, which uses cell vertex finite volume method, it uses the cell centre finite volume technique over a structured or unstructured mesh domain to solve flow, heat transfer problems. PHYSICA has links with pre/post processors like FEMGEN/FEMVIEW [75] and PATRAN [76]. The work presented in this chapter used PHYSICA's environment for including the solid equations in

a CFD framework. Therefore, it will be convenient to present the discretization techniques and solution procedures of PHYSICA in the following sections.

6.2.1 Discretization used in PHYSICA

Because equations (6.7) and (6.15) are special forms of the general CFD equation, the following discussion details the differencing schemes and methods of interpolation for the general CFD equations used in PHYSICA.

If we introduce a general variable, ϕ, the conservative form of all fluid flow equations including equations for scalar quantities such as temperature can usefully be written in the following form [73]:

$$\frac{\partial(\rho\phi)}{\partial t} + div(\rho \mathbf{v}\phi) = div(\Gamma_\phi grad\phi) + S_\phi \tag{6.19}$$

Suitable approximations can be made to each term in equation (6.19) which allows it to be expressed as a linear matrix equation with the form of:

$$\mathbf{A}\boldsymbol{\phi} = \mathbf{b} \tag{6.20}$$

Where $\boldsymbol{\phi}$ is a vector of the value of ϕ at a finite number of computational points, such that the solution of equation (6.20) gives as close an approximation as possible to the solution of (6.19).

The techniques used to discretize the various conservation equations are based on the cell centred finite volume formulation. As mentioned in chapter 3, in this method the domain over which the equation is to be solved is divided into a set of non-overlapping polyhedral control volumes. The dependant variables which are the averaged value over the CV are stored at the centre of CV. The FV method involves integrating the conservation equation (6.19) over each control volume and over time. Assumptions are made for the variations of the quantities involved in the equation between the centre of the control volumes. For each control volume this leads to a

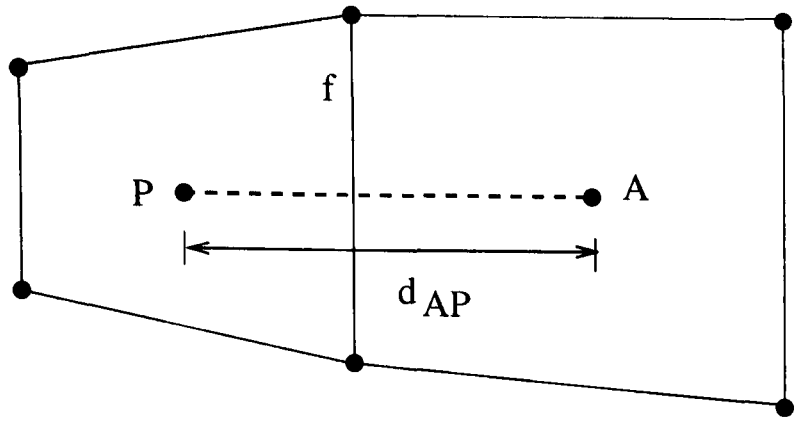

Figure 6.1: Adjacent control volumes

linear equation involving the unknown values of the scalar quantity at the centre of the control volume and the centre of its neighbouring control volumes. Considering all such linear equations together produces a matrix equation of the form (6.20). The final discretized form of the conservation equation is [39]:

$$a_P \phi_P = \sum_{nb} a_{nb} \phi_{nb} + b_P \tag{6.21}$$

Where the summation is over all elements which share a face with element P. The coefficients in equation (6.21) are calculated from the formulae:

$$a_{nb} = D_f A(\mid P_f \mid) + max(-F_f, 0.0)$$

$$a_P = \sum_{nb} a_{nb} + \frac{V_P^o \rho_P^o}{\Delta t} + S_P V_p$$

$$b_P = S_C V_P + \frac{V_P^o \rho_P^o}{\Delta t} \phi_P^o$$

Where the S_C and S_P are the components of the linearised form of the source term as:

$$S_\phi = S_C - S_P \phi \tag{6.22}$$

the superscript "o" indicates previous time step values, V is the volume of element P, Δt is the time step size, D_f and F_f are the strengths of the diffusion and convection respectively, P_f is the Peclet number and are given by:

$$F_f = A_f \rho_f (\mathbf{v} \cdot \mathbf{n})_f$$

$$D_f = \frac{A_f(\Gamma_\phi)_f}{d_{AP}}$$

$$P_f = \frac{F_f}{D_f} = \frac{\rho_f(\mathbf{v}\cdot\mathbf{n})_f}{(\Gamma_\phi)_f}$$

A_f is area of face f.

d_{AP} is the distance between the centroids of elements A and P, see Figure 6.1, and the differencing scheme functions, $A(|\ P_f\ |)$, are listed in the table (6.1):

Scheme	Formulae for A(|P|)
Central Differencing	1-0.5|P|
Upwind	1
Hybrid	max(0 , 1-0.5|P|)
Power Low	max(0 , $(1-0.1\|P\|)^5$)
Exponential	|P|/exp(|P|)-1

Table 6.1: Definition of differencing schemes

6.2.2 Rhie-Chow interpolation method

The solution procedure for the transport of a general property ϕ developed in the previous section will, of course, be enlisted to solve the momentum equations. Matters are, however, not completely straight forward since there are problems associated with the pressure source terms of the momentum equations that need special treatment. If the velocities and the scalar variable of pressure are both defined at the centre of an ordinary control volume a highly non-uniform pressure field can act like a uniform field in the discretized momentum equations [73]. This can be demonstrated with the simple two dimensional situation shown in Figure 6.2, where a uniform grid is used for simplicity. If the pressure at face "e" and face "w" ob-

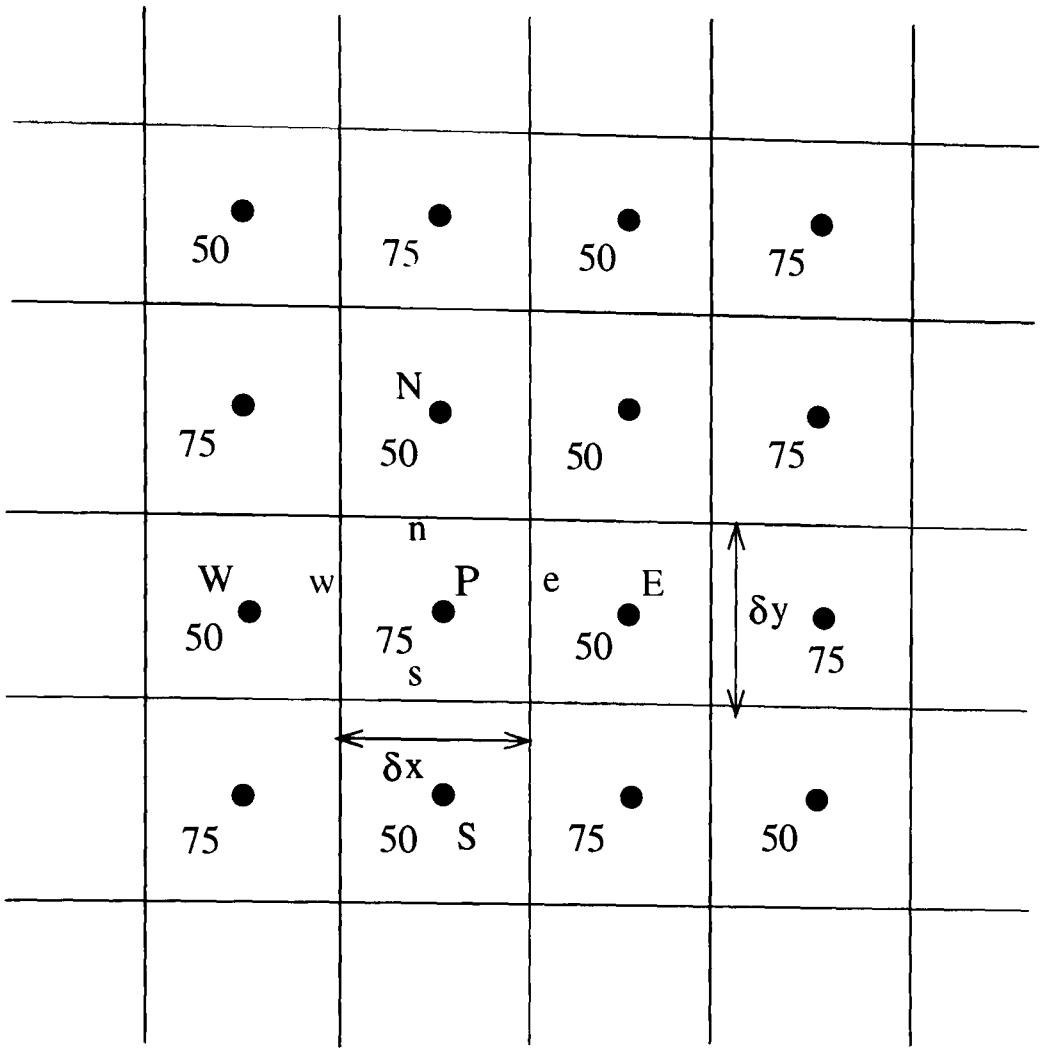

Figure 6.2: A checkboard pressure field

tained by linear interpolation, the pressure gradient term $\frac{\partial P}{\partial x}$ in the v_x-momentum equation is given by:

$$\frac{\partial p}{\partial x} = \frac{p_e - p_w}{\delta x} = \frac{(\frac{p_E + p_P}{2}) - (\frac{p_P + p_W}{2})}{\delta x} = \frac{p_E - p_W}{2\delta x} \tag{6.23}$$

Similarly, the pressure gradient $\frac{\partial P}{\partial y}$ for the v- momentum equation is evaluated as:

$$\frac{\partial p}{\partial y} = \frac{p_N - p_S}{2\delta y} \tag{6.24}$$

Substituting the appropriate values from the "checker-board" pressure field from Figure 6.2 into formulae (6.23) and (6.24) we find that all the discretized gradients are zero at all the nodal points even though the pressure field exhibits spatial oscillations in both directions. This behaviour is obviously nonphysical.

The standard approach for overcoming the above problem is the use of a staggered grid for the velocity components which was first suggested by Harlow and Welch [77]

and forms the basis for the SIMPLE procedure [78] and for the SIVA procedure [79]. The idea is to evaluate scalar variables such as pressure, density, temperature etc at the centre of each CV but to calculate velocity components on staggered grids centred around the cell faces. Based on this idea the v_x velocity is calculated at the faces of the control volume which their normals are in the x coordinate direction. Similarly the v_y and v_z velocities are calculated at the faces of the control volume with normals in the y and z directions respectively. This type of calculation for the the velocity components on different places is of huge benefit on structured meshes but the method does not extend easily to unstructured meshes.

In the approach presented here all dependant variables are stored at the cell centre, i.e. collocated variable arrangement is used. In contrast to the staggering approach which uses four sets of control volume in three dimensional analysis, this arrangement requires only one set of control volumes. The face values of the velocity components have to be calculated from the element based values. This requires an alternative interpolation method to those described earlier in this section which does not suffer from the checker board effect. The Rhie-Chow interpolation method [40] offers one approach which satisfies these requirements.

The x-momentum equation:

$$\frac{\partial(\rho v_x)}{\partial t} + div(\rho v_x \mathbf{v}) = -\frac{\partial p}{\partial x} + div(\mu grad v_x) + S_{Mx} \tag{6.25}$$

where $(\lambda + \mu) div\mathbf{v}$ in equation (6.7) is considered as zero. This equation can be discretized by using the techniques described earlier in this chapter over the control volume about a node P to produce an equation which can be written in the form:

$$a_P v_{(x)P} + (\nabla_x p)_P = (\sum a_{nb} v_{(x)nb})_P + S_P \tag{6.26}$$

Where $\nabla_x p$ is the discretized contribution from the pressure gradient term. Similarly for the adjacent node A:

$$a_A v_{(x)A} + (\nabla_x p)_A = (\sum a_{nb} v_{(x)nb})_A + S_A \tag{6.27}$$

From the conservation principle of the control volume formulation the v_x velocity at a point on the face between the nodes must also have a discretized momentum equation of the form:

$$a_f v_{(x)f} + (\nabla_x p)_f = (\sum a_{nb} v_{(x)nb})_f + S_f \tag{6.28}$$

The Rhie-Chow interpolation method uses the equations (6.26), (6.27) to approximate a solution for equation (6.28). It is assumed that the right hand side of equation (6.28) may be approximated by using a weighted linear interpolation of the corresponding terms in equations (6.26) and (6.27).Thus

$$a_f v_{(x)f} + (\nabla_x p)_f = \overline{(\sum a_{nb} v_{(x)nb})_f + S_f} = \overline{a_f v_{(x)f}} + \overline{(\nabla_x p)_f} \tag{6.29}$$

Where the overline in the above equation indicates a weighted linear interpolation of the variable. Assuming that $a_f = \overline{a_f}$ then:

$$v_{(x)f} = \overline{v_{(x)f}} + \overline{d_f}(\overline{\nabla_x p_f} - \nabla_x p_f) \tag{6.30}$$

Where if β as the weighting factor is used, we have:

$$\overline{v_{(x)f}} = \beta v_{(x)P} + (1-\beta) v_{(x)A}$$

$$\overline{\nabla_x p_f} = \beta \nabla_x p_P + (1-\beta) \nabla_x p_A$$

$$\nabla_x p_f = A_f n_x (p_A - p_P)$$

$$a_f = a_P + (1-\beta) a_A$$

$$\overline{d_f} = a_f^{-1}$$

The weighting factor, β, is set at 0.5 otherwise unrealistic solutions may be achieved with the distance weighted interpolation which has been reported [39].

6.2.3 Momentum-Pressure coupling

One common approach to the evaluation of the velocity field and pressure field is the iterative method. Given a pressure field p, discretized momentum equations can

be solved to obtain the velocity fields. If the pressure field is correct the resulting velocity field will satisfy continuity. As the pressure field is unknown, we need a method for calculating the pressure.

6.2.4 SIMPLE algorithm

The acronym SIMPLE stands for Semi-Implicit Method for Pressure-Linked Equations [73]. The algorithm was originally put forward by Patankar and Spalding [78] and is essentially a predictor-corrector procedure for the calculation of pressure field. By discretizing the continuity equation:

$$\frac{\rho_P V_P - \rho_P^o V_P^o}{\Delta t} + \sum_f A_f(\rho \mathbf{v} \cdot \mathbf{n})_f = 0 \tag{6.31}$$

Where the superscript "o" indicates the previous time step value, Δt is the time step. The summation is over all faces of the control volume signified by the subscript P. The Rhie-Chow interpolation gives the equation for a face velocity component as:

$$v_{(x)f} = \overline{v_{(x)f}} + \frac{1}{a_f}(\overline{\nabla_x p_f} - \nabla_x p_f) \tag{6.32}$$

where the overline indicates linear interpolation of the relevant quantity between the element centre values on either side of face f. In equation (6.32) the $\nabla_x p_f$ term is approximated by $A_f n_x(p_A - p_P)$ where the subscripts P and A represent the current and adjacent elements respectively. At any solution stage, given estimated element centre values for pressure, p^* and velocity v_x^*, the face value of the v_x component of velocity is given by:

$$v^*_{(x)f} = \overline{v^*_{(x)f}} + \frac{1}{a_f}(\overline{\nabla_x p^*_f} - \nabla_x p^*_f) \tag{6.33}$$

The aim is to improve the guessed pressure p^* in order that the starred velocity components get progressively closer to satisfying the continuity equation . If p is the correct pressure then:

$$p = p^* + p' \tag{6.34}$$

Where p' is the pressure correction. Similarly the starred velocities are related to their correct values by:

$$v_x = v_x^* + v_x' \qquad v_y = v_y^* + v_y' \qquad v_z = v_z^* + v_z' \tag{6.35}$$

If equation (6.33) is subtracted from equation (6.32) then following equation is obtained:

$$v'_{(x)f} = \overline{v'_{(x)f}} + \frac{1}{a_f}(\overline{\nabla_x p'_f} - \nabla_x p'_f) \tag{6.36}$$

The use of all terms in equation (6.36) would produce an equation in which the pressure correction in an element is directly dependent on corrections in both neighbouring elements and elements adjacent to these neighbours. This would lead to the need to solve a linear matrix with a much larger number of non zero elements per row than any of the matrices constructed in the solution of the other solved variables. In order to simplify the resulting pressure correction equation, the first two terms on RHS of equation (6.36) are dropped. At convergence the terms which have been ignored would be zero so this assumption does not affect the final answer, only the way in which the final answer is approached. Hence:

$$v'_{(x)f} = -\frac{1}{a_f}(\nabla_x p'_f) = \frac{1}{a_f} A_f n_x (p'_P - p'_A) \tag{6.37}$$

Finally substituting equation (6.35) in the discretized continuity equation (6.31) and using equation (6.37) for the correction term, gives:

$$\sum_f \rho_f A_f^2 \frac{(\mathbf{n}\cdot\mathbf{n})_f}{a_f}(p'_P - p'_A)_f = \frac{\rho_P V_P - \rho_P^o V_P^o}{\Delta t} - \sum_f A_f \rho_f (\mathbf{v}^*\cdot\mathbf{n})_f \tag{6.38}$$

The above equation can be written in the form:

$$a_P p'_P = \sum_{nb} a_{nb} p'_{nb} + b_P \tag{6.39}$$

Where the summation in equation (6.39) is over all elements sharing a face with element P and :

$$a_{nb} = \rho_f A_f^2 \frac{(\mathbf{n}\cdot\mathbf{n})_f}{a_f}$$

$$a_P = \sum_{nb} a_{nb} \tag{6.40}$$

$$b_P = \frac{\rho_P V_P - \rho_P^o V_P^o}{\Delta t} - \sum_f A_f \rho_f (\mathbf{v}^* \cdot \mathbf{n})_f$$

A set of linear equations can be set up by using equation (6.39) which has weak diagonal dominance. The diagonal being at least as large as the sum of absolute values the off diagonal elements. Boundary conditions or a fixed reference pressure point, will guarantee diagonal dominance on some rows.

By solving equation (6.39) the pressure correction is obtained and the pressure field can be updated by use of equation (6.34). Pressure corrections based on this procedure are frequently over-estimated so they need to be relaxed as:

$$p = p^* + \gamma p' \tag{6.41}$$

Where γ is between 0.0 and 1.0.

Equation (6.37) gives an equation to calculate the face velocity corrections but what is needed is the velocity corrections for the CV centre value rather than these face values. If the discretized form of the momentum equation is considered:

$$a_P v_{(x)P} = \sum_{nb} a_{nb} v_{(x)nb} + b - \nabla_x p_P \tag{6.42}$$

then at any stage given a guessed pressure field,p^*, an estimated velocity field v^* can be calculated:

$$a_P v^*_{(x)P} = \sum_{nb} a_{nb} v^*_{(x)nb} + b - \nabla_x p^*_P \tag{6.43}$$

Subtracting equation (6.43) from equation (6.42) and using equations (6.34) and (6.35) an equation is obtained expressing the velocity correction in the element as a function of neighbouring velocity corrections and the integrated gradient of the pressure correction in the element:

$$a_P v'_{(x)P} = \sum_{nb} a_{nb} v'_{(x)nb} - \nabla_x p'_P \tag{6.44}$$

At this stage an approximation is introduced by dropping the summation terms to simplify equation (6.44). This leads to the following formula for the velocity

correction:

$$v'_{(x)P} = -\frac{1}{a_P} \nabla_x p'_P = -\frac{1}{a_P} \sum_f A_f n_x p'_f \tag{6.45}$$

Expanding the right hand side gives the following equation for the velocity correction in terms of pressure corrections in the element and all its neighbours.

$$v'_{(x)P} = -\frac{1}{a_P} \sum_{nb} A_f n_x (\alpha_f p'_P + (1-\alpha_f) p'_A) \tag{6.46}$$

6.2.5 Modification to the solution procedure of PHYSICA for solid mechanics problems

Modifications to the previous solution procedure are required for solving solid mechanics problems. Equation (6.18) for solid problems should be used instead of the continuity equation. For an incompressible fluid the continuity equation is expressed as:

$$div\mathbf{v} = 0 \tag{6.47}$$

Which is equivalent to equation (6.39) at the discretized level and can be applied instead.

The solid material can be considered virtually as an incompressible fluid. As pointed out before, the velocity vector in a fluid equation corresponds to the displacement vector in the solid equation. As a result, the first term of equation (6.18), $div\mathbf{u}$, is substituted by equation (6.39). Using this substitution and using equation (6.34) the discretized form of equation (6.18) will be:

$$a_P p'_P - \sum_{nb} a_{nb} p'_{nb} - b_P + \frac{1-2\nu}{G}(p'_P + p^*_P)V_P - 2\alpha(1+\nu)(T_P - T_r)V_P = 0 \tag{6.48}$$

or

$$a^{mod}_P p'_P = \sum_{nb} a_{nb} p'_{nb} + b^{mod}_P \tag{6.49}$$

Where by using equation (6.40) and dropping the transient term:

$$a_{nb} = \rho_f A_f^2 \frac{(\mathbf{n}\cdot\mathbf{n})_f}{a_f}$$

$$a_P^{mod} = \sum_{nb} a_{nb} + \frac{1-2\nu}{G} V_P \tag{6.50}$$

$$b_P^{mod} = -\sum_f A_f \rho_f (\mathbf{u}^* \cdot \mathbf{n})_f - \frac{1-2\nu}{G} p_P^* V_P + 2\alpha(1+\nu)(T_P - T_r)V_P$$

Taking advantage of the similarities between the fluid and solid momentum equations and using pressure correction, equation (6.49), in the SIMPLE algorithm, solid problems can be modelled in the CFD framework and solved by CFD solution procedures. These modifications can be applied in PHYSICA by user-routine environment.

6.3 Thermally coupled stress-flow problem modelling in PHYSICA

As mentioned already in chapter 1, in the analysis of these problems we have a coupled problem which involves stress, flow and heat transfer phenomena. Stress in solid region is governed by the thermal load. Demirdzic *et al.* [31] studied this type of coupled problem. In his approach he used the cell centred finite volume displacement based formulation for the solid region and standard CFD analysis for fluid region. Fluid effects on interfaces are considered as a surface tension load on the solid faces, which are in contact with the fluids. Governing equations of fluid and solid are solved turn by turn until an equilibrium state is achieved. Spalding [32] also developed a method which is the basis of the work presented here. Applying PHYSICA to the multiphysics problems in standard manner is illustrated in Figure 6.3. As mentioned in this figure the solution procedures consist of two different steps. In the first step, temperature and velocity distributions are calculated in the whole model by using the CFD solution procedure and thereafter the stress distribution is calculated by solving the classic stress equations. This 2-solver approach solves the problem in a decoupled manner and has the following disadvantages:

- 2-solver approach will try to solve flow equations in solid region and to solve

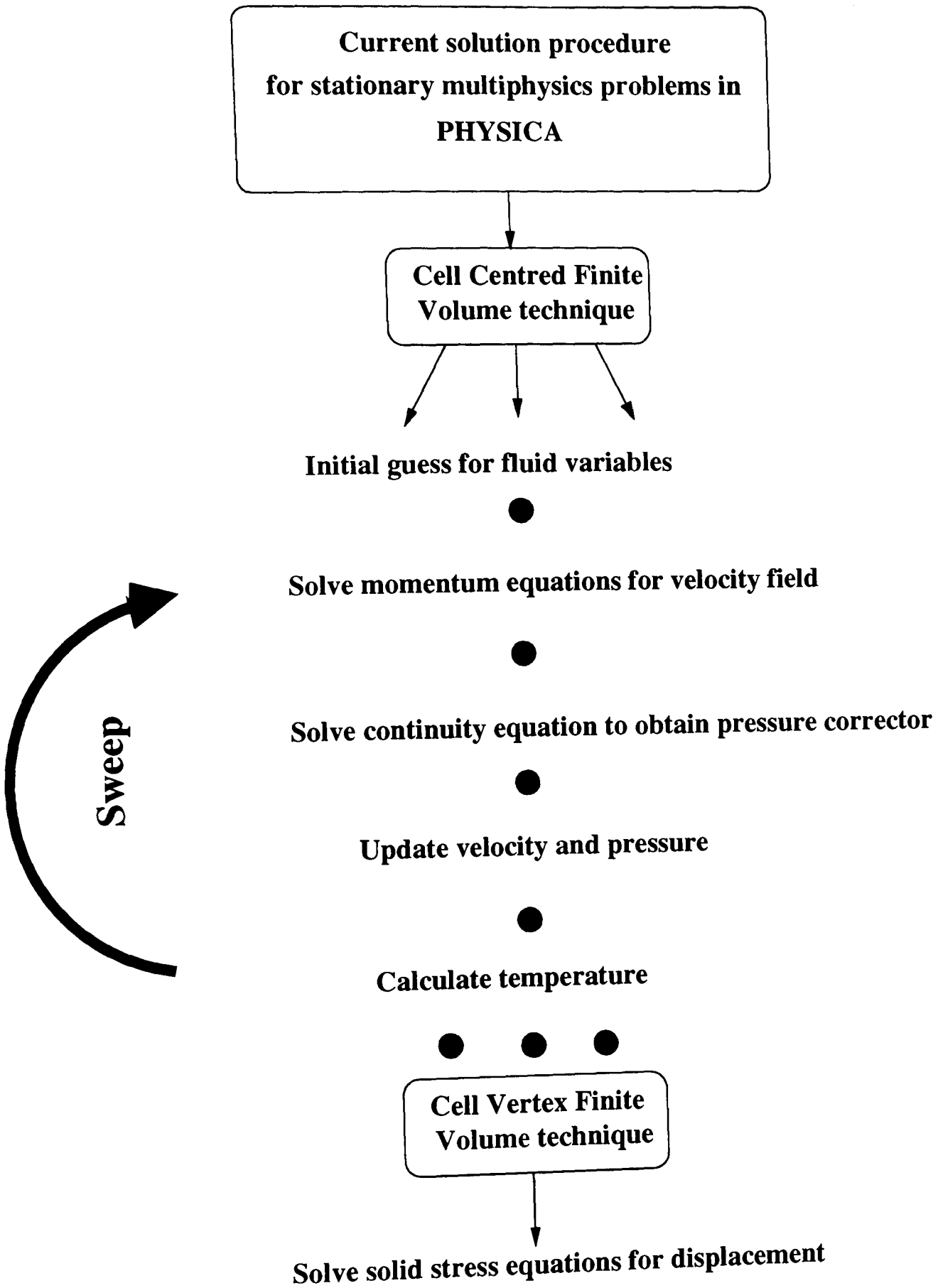

Figure 6.3: Current solution procedure (2-solver approach) for multiphysics problems in PHYSICA.

stress equations in flow region in the first and the second steps respectively.

- Extrapolation errors can occur by using different discretization techniques in two steps of the solution.

In the 2-solver approach the following assumptions have been used in this work:

- Solid deformation does not affect the geometry of the flow region.
- stress on solid interfaces is neglected.

By applying the above assumptions and using the method developed in the previous section, the solution procedures can be simplified to using a single CFD solver for the whole field. In this manner a complete set of CFD solvers are used for the calculation of velocity field and displacement field, where they are calculated simultaneously, see Figure 6.4. Treating the problem in this manner contains a consistent solution strategy and also benefits in terms of solution speed and especially in memory usage.

6.4 Validation test cases

In this section a set of test cases present the capability of the above modified formulation for solid mechanics and multiphysics analysis. The first test involves a one dimensional bar subject to an axial load. The second is a confined bar with the free ends, where at the one end displacement imposed to the bar and the resulting displacement inside the bar is calculated and compared with the FE results and cell vertex finite volume method results. The third test case shows the capability of the method for a two dimensional problem involving heat transfer and displacement calculations. In the fourth test case the capability of the formulation will be shown for the analysis of a multiphysics case which involves a contribution of heat transfer and fluid flow effects.

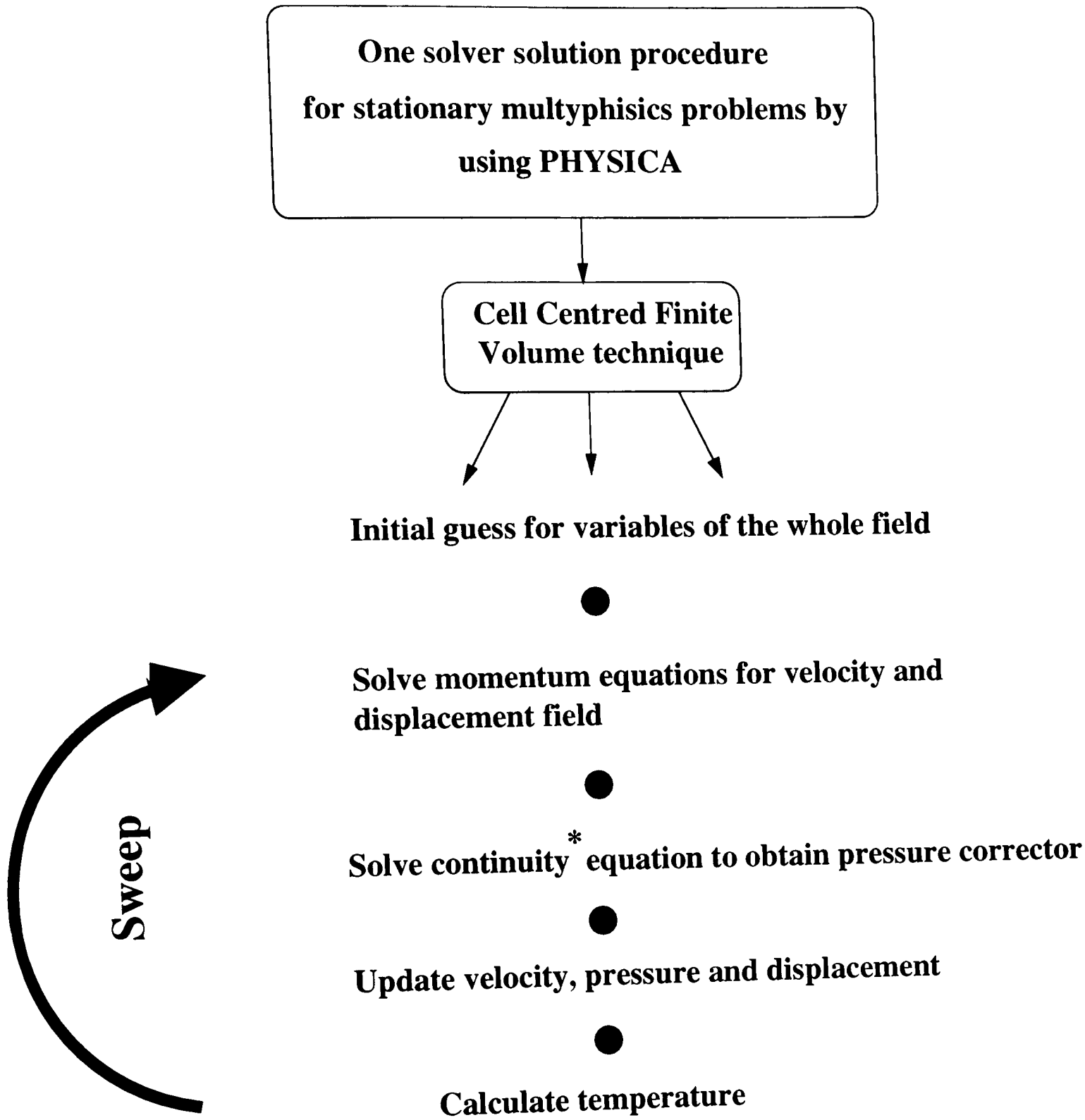

* For solid region pressure-displacement equation instead

Figure 6.4: One-solver solution procedure for multiphysics problems by using PHYSICA.

6.4.1 Test case-1

For presenting the capability of the modified fluid flow formulation for pure solid application an axial tensioned bar was analysed, Figure 6.5. For this one dimensional

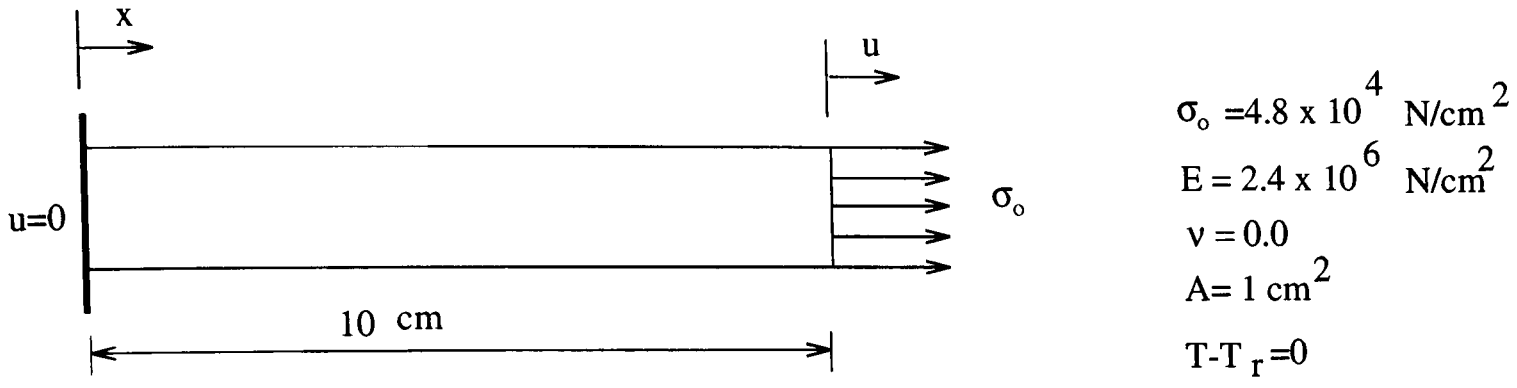

Figure 6.5: Axial loaded bar

case the general momentum equations (6.15) reduce to:

$$-\frac{\partial p}{\partial x} + \frac{\partial^2 u}{\partial x^2} + S_{Mx} = 0$$

Using equation (6.18) gives:

$$p = -G\frac{\partial u}{\partial x}$$

Where Poisson's ratio, ν, corresponding to this one dimensional analysis is zero.

At the loaded end we have:

$$\frac{\partial u}{\partial x} = \frac{\sigma_o}{E}$$

Therefore:

$$p = -G\frac{\sigma_o}{E} = -\frac{\sigma_o}{2}$$

So the boundary condition on the loaded end can be considered as $p = -\frac{\sigma_o}{2} = -2.4 \times 10^4 \frac{N}{cm^2}$ and on the fixed end the boundary condition can also be considered as $u = 0$.

PHYSICA was used for the analysis. One 4-noded quadrilateral element was used. Fluid flow module(i.e., Flow module) was switched on for the analysis. Necessary arrangements in the flow module for this analysis are:

- Activating the Flow module for momentum calculations just in the x direction.
- Calculation of pressure variable.
- Accommodating the equation (6.49) in the solution procedure by adding convenient source term in the pressure correction equation.

With these arrangements PHYSICA predicts $0.2cm$ elongation which is the same as the theory result.

6.4.2 Test case-2

In this test a bar with square cross section and length of $10cm$ is prevented from deforming laterally, is subjected to an uniform displacement of $0.25cm$ at the left end in the z direction, see Figure 6.6. The right end of the bar is stress free. To

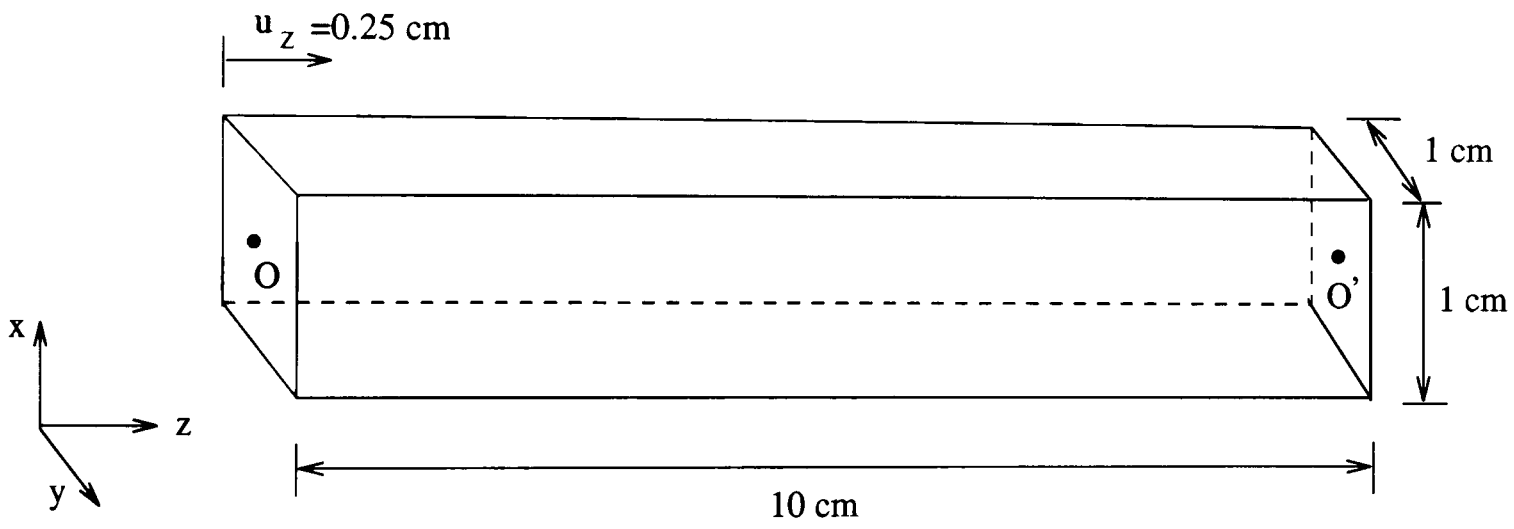

Figure 6.6: Solid bar under the left end forced displacement

attempt to accurately model the formation of the displacement profile a fine mesh was used near the induced displacement boundary and gradually becomes coarser towards the free end. This problem was analysed as a three dimensional case and

8-noded Brick element was used for discretization. The sides of cross section in x and y directions are divided to equal divisions where length in the z direction is divided in nonequal divisions as mentioned above. The z component of displacement along the line OO_1 was selected for comparison of modified CFD formulation results and the classic FE results and the results of FV method solving the classic stress equations. Flow module of PHYSICA was used and momentum calculations were switched on in the three directions, x, y and z. Also pressure calculation has taken place and equation (6.49) was considered in the solution procedure. Figure 6.7 shows the boundary conditions. Figure 6.8-2 shows PHYSICA result and Figure

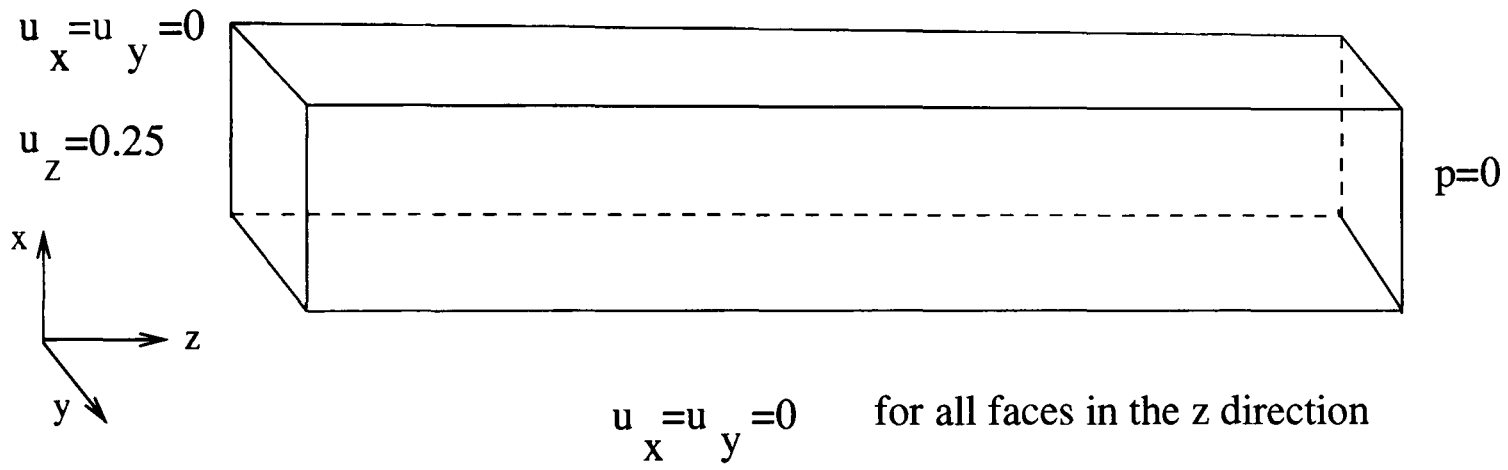

Figure 6.7: Boundary conditions for the solid bar

6.8-3 shows FE result corresponding to 20 divisions on each side. Figures 6.9 and 6.10 show the convergence in FE results and CFD approach results by refining the mesh. In Figure 6.11 the result of CFD approach is compared with FE method. In Figure 6.12 the result of three methods are compared together. In PHYSICA for control volume with face on the boundary, the nodal value is calculated based on the control volume centroid value apart from boundary values. So in Figure 6.8-2 the graph does not start from correct quantity of boundary displacement value, $0.25cm$. Apart from this quantity, the result of three methods are very close.

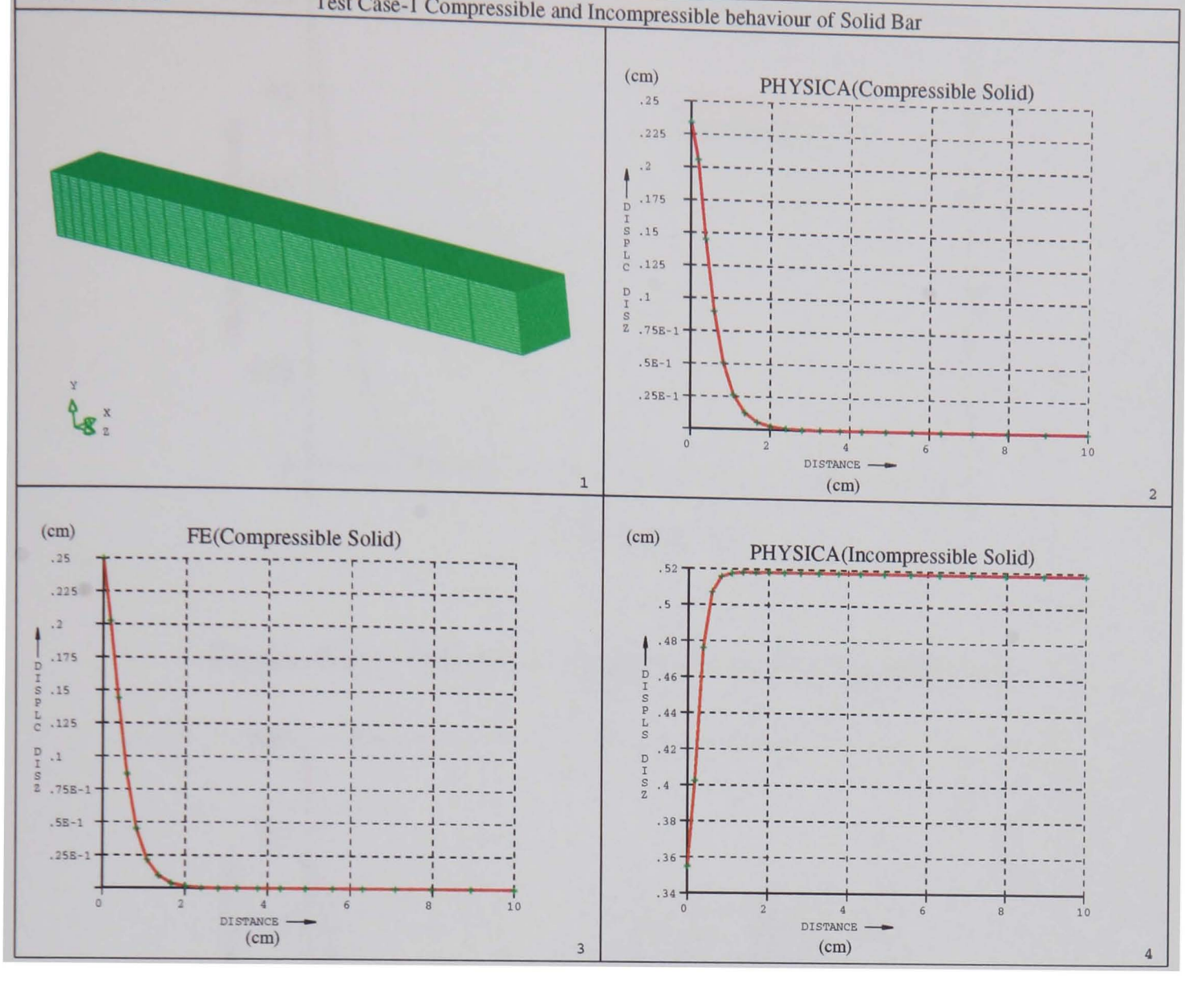

Figure 6.8: z Component of displacement of central line of bar

For presenting the capability of PHYSICA for analysis of incompressible solids the Poisson's ratio of the material was changed to 0.5. As Figure 6.8-4 shows, for maintaining the volume of the bar at the constant initial quantity the solid deforms at the right end in the z direction. As can be seen the incompressibility condition changes the solid behaviour totally different to what has been seen in Figure 6.8-2 or Figure 6.8-3. Note that the usual displacement based formulation of FE or FV method will not be able to solve this problem when $\nu = 0.5$.

It will be instructive presenting the z component of velocity profile of an incom-

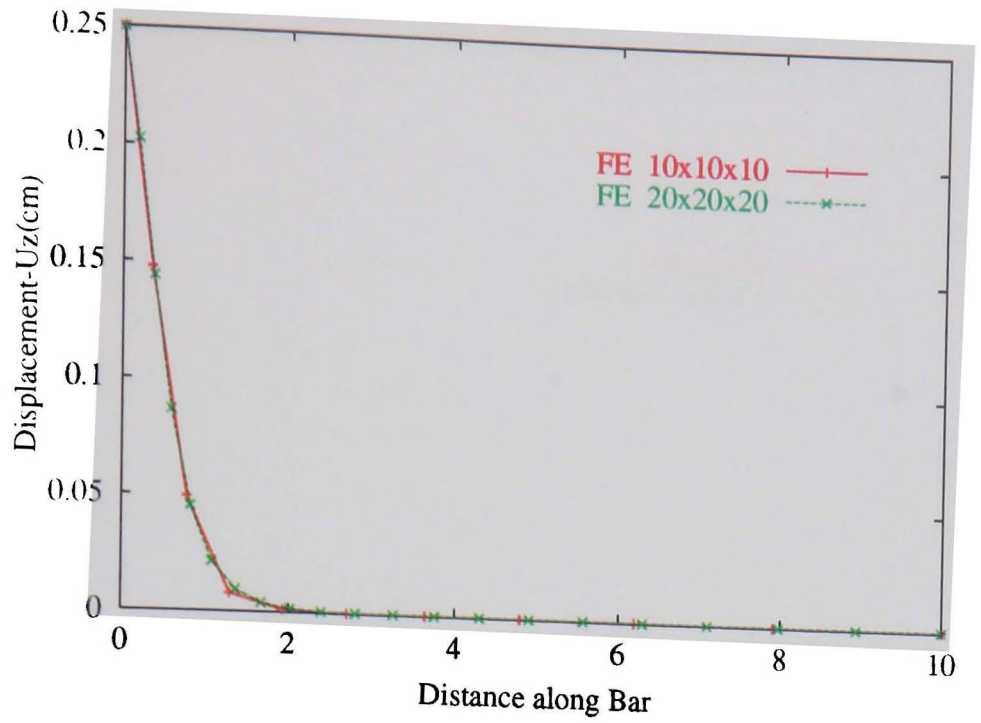

Figure 6.9: z Component of displacement of central line of bar

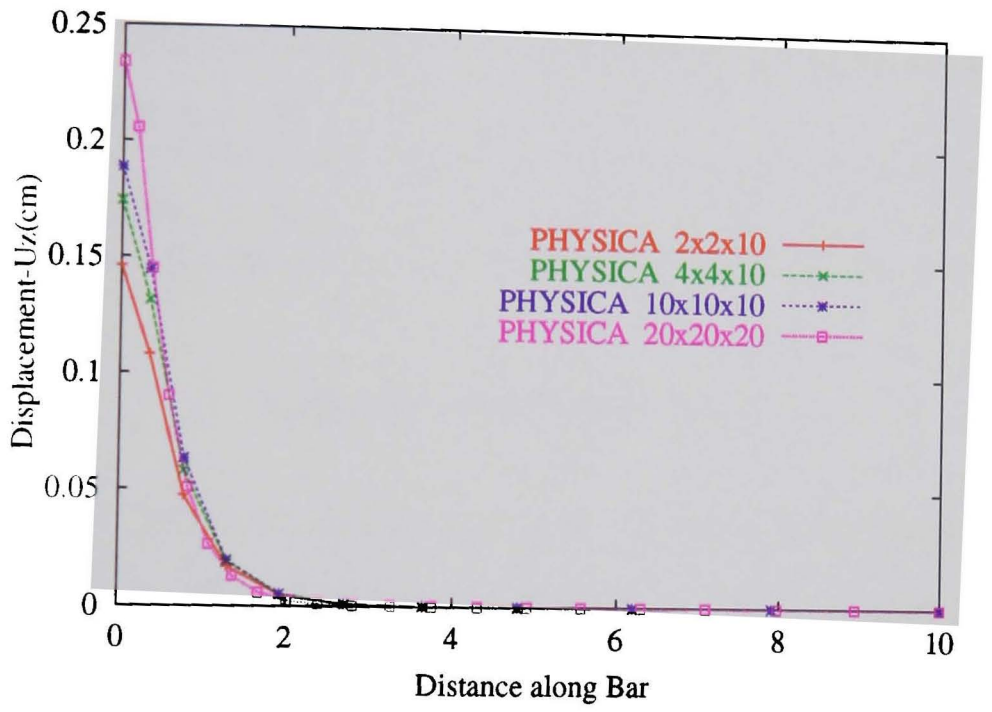

Figure 6.10: z Component of displacement of central line of bar

pressible flow of a fluid in a duct with the same geometry. Figure 6.13 shows such behaviour for an incompressible flow. The lateral boundary conditions is the same as the solid bar boundary conditions and at the inlet fluid enters to the duct with $v_z = 0.25cm/sec$ and at the outlet zero pressure boundary condition is assumed and the dynamic viscosity of the fluid is considered equal to the shear modulus of the

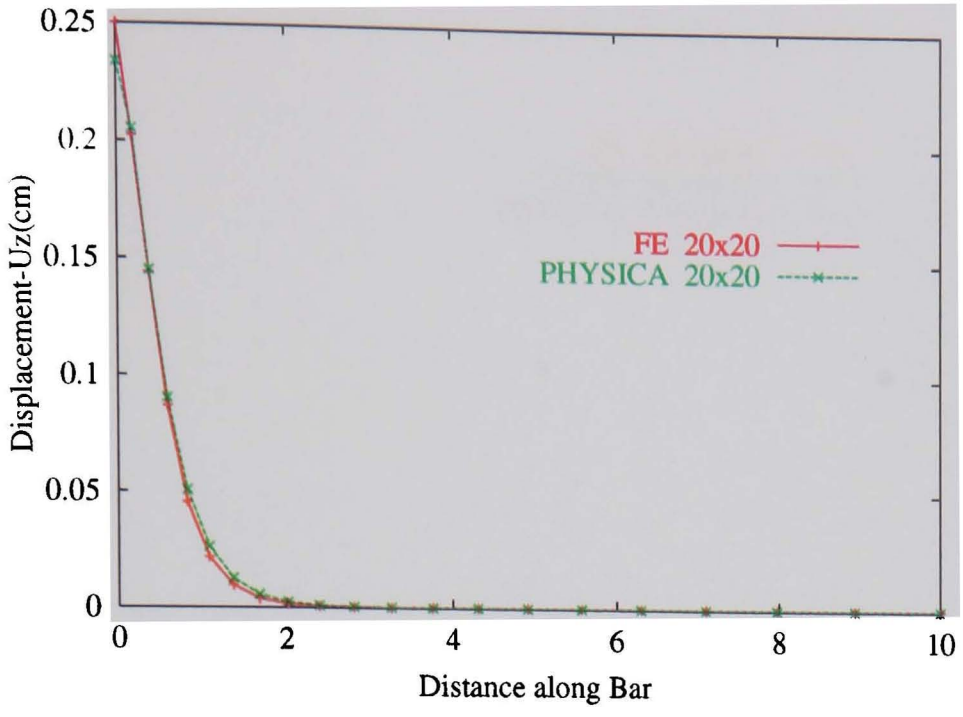

Figure 6.11: z Component of displacement of central line of bar

Discretisation Method		FE	CV-FV	PHYSICA
CPU Time (Sec)	3-Dimen.	37	216	17
	2-Dimen.	2	3	13

Table 6.2: Total CPU time

solid bar(i.e., 0.96×10^6). As can be seen the velocity of the incompressible fluid is equal to the displacement of incompressible solid. This is expected, because for an incompressible solid, without thermal load, equation (6.49) has the same form as fluid continuity equation. This coincidence completes the similarities of fluid and solid equations.

Table (6.2) shows the total CPU times spent for the solution procedures using the different methods. The tests were carried out on a SUN SPARC20 work station. Ten divisions on each side were considered. For more comparisons the test was also analysed as a two dimensional plain strain case which is discretized by BLQ ele-

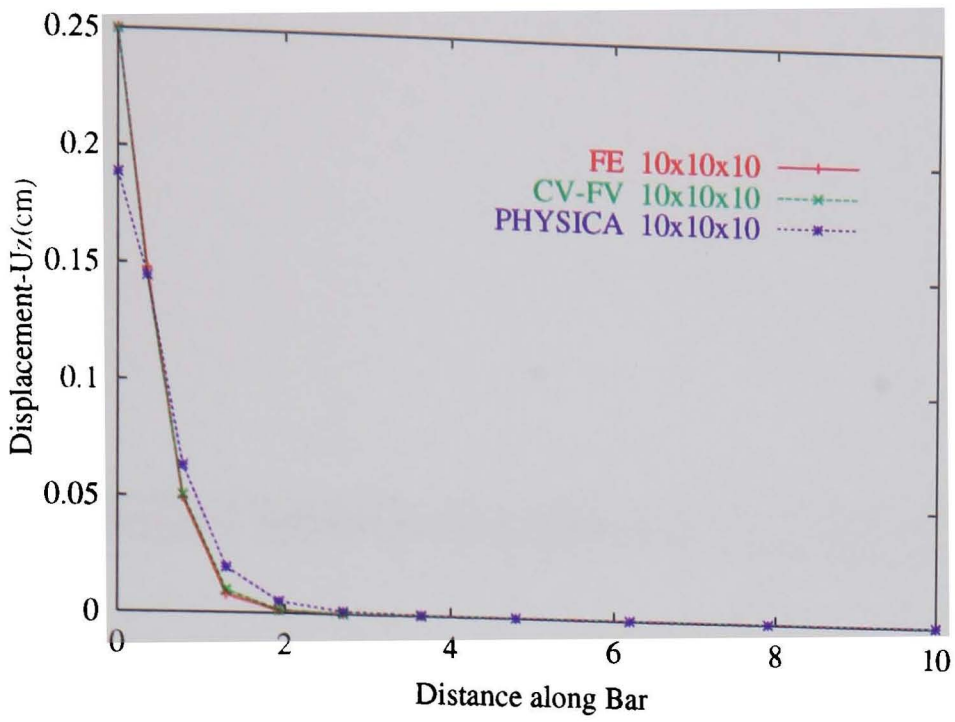

Figure 6.12: z Component of displacement of central line of bar

ments. With nearly the same accuracy, the total CPU time of the CFD procedure for 8-noded brick elements is less than the CPU time spent in FE procedure and CV-FV procedure but reversely in the two dimensional analysis the CFD procedure needs more CPU time than the two other methods.

6.4.3 Test case-3

In this test a rectangular plate with the specified boundary conditions, shown in Figure 6.14-1, was analysed. Four noded quadrilateral elements were used for discretization with 80 uniform divisions in x direction and 40 nonuniform divisions in y direction. The present one-solver approach and the traditional 2-solver approach were used in the analysis. In one solver approach the Flow and Heat transfer modules of PHYSICA were switched on and in 2-solver approach the Flow, Heat transfer and EVP(i.e., elastic visco plastic module) modules were used. Figure 6.14-3 shows temperature contours and in Figure 6.14-2 and (6.14-4) the displacement along the line BA are presented.

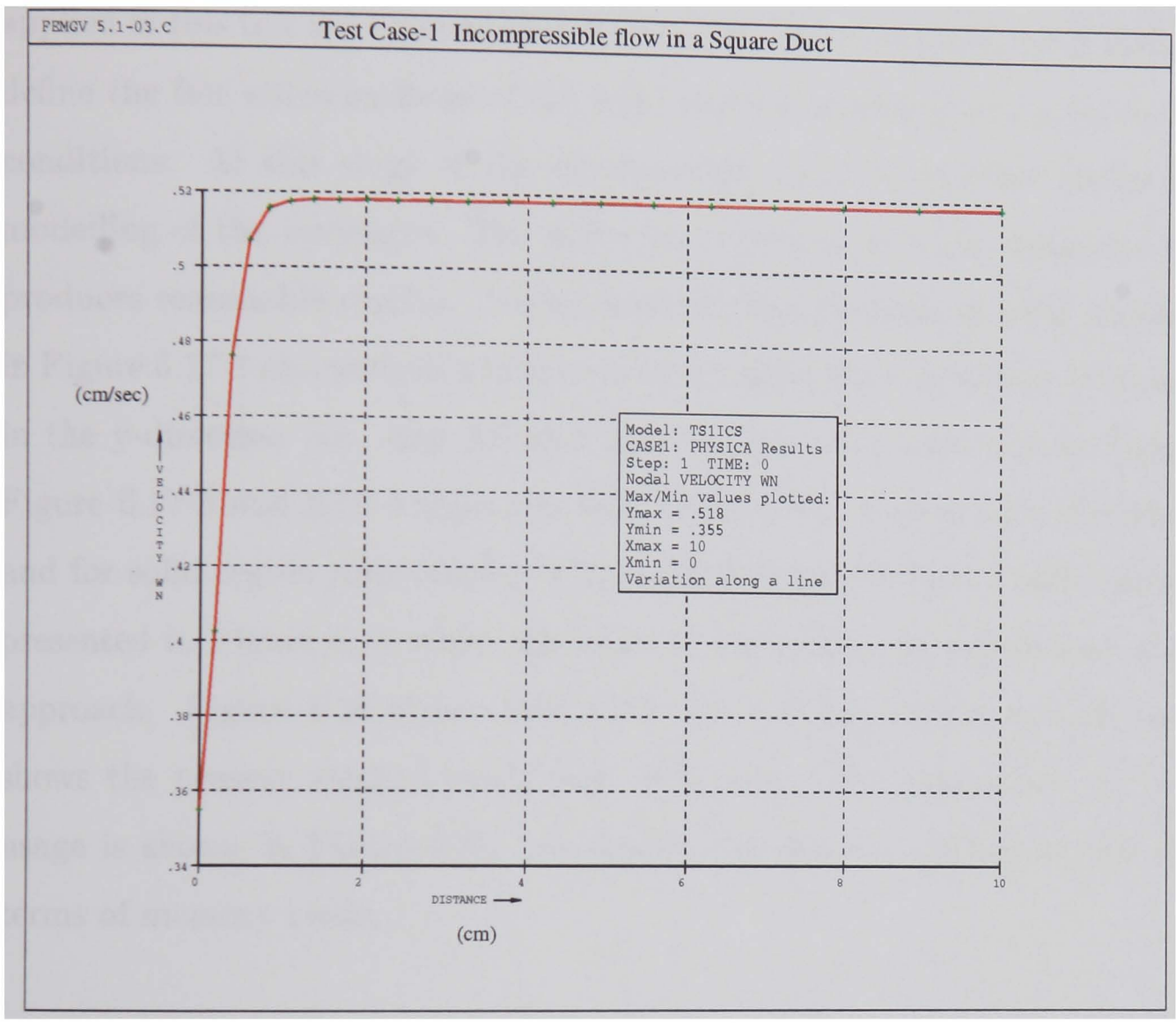

Figure 6.13: z Component of velocity of incompressible fluid on central line of a square duct

6.4.4 Test case-4

In this test a 2-dimensional solid block with a heat source which is being cooled by the flowing ambient cold air was analysed, see Figure 6.15. The importance of this test is, it demonstrates the modified CFD procedure solve the solid stress, heat transfer and fluid flow equations simultaneously by using the CFD solvers. Four-noded quadrilateral elements were used for discretization. The boundary conditions applied in this test are illustrated in Figure 6.16. Attempts have been made to try to define the free stress surfaces of the solid part by assuming zero pressure boundary conditions. At this stage of the development, there is no other choice for better modelling of the interfaces. The following results show these boundary conditions produces reasonable results. Nodal resultant displacement of solid region is shown in Figure 6.17-1 and variation of this quantity along the central line of the solid block in the y-direction (i.e. line AB in Figure 6.15) is also presented in Figure 6.17-2. Figure 6.17-3 and 6.17-4 show the heat distribution contours for the whole model and for solid region respectively. The equivalent results from 1-solver approach are presented in Figure 6.18 which are close to the results presented from the 2-solver approach. Figure 6.19 shows total CPU time corresponding to each method. It shows the present method needs less CPU time. The comparison of the memory usage is shown in Figure 6.20. As shown, the present method is also efficient in terms of memory needs.

6.5 Closure

A Novel method based on the CFD solution procedure has been presented for solid mechanics problems and those involve different physics which affect each others. The method uses the CFD solution procedure to calculate the unknown displacements in solid problems. For solid problems where the Poisson's ratio is close to 0.5 the usual displacement approach fails in predicting the accurate results but the present method can handle the situation properly. The reason for this capability is,

we take out the mean value of the normal stresses from the stress tensor as an unknown variable. The novel feature of the present method can be seen in the coupled problems involving fluid and solid materials. Instead of using two different solvers for predicting of unknowns(i.e., velocity, pressure, temperature, displacement) the method uses CFD solution procedures for predicting the velocity components in fluid region and displacement components in solid region. The results of test cases show that the method is efficient in terms of both CPU time and memory usage. The Flow module of PHYSICA was developed for the fluid type problems, inevitably the boundary conditions considered in this module are limited to the fluid problems. To apply this module to the solid mechanics problems, developing convenient type of boundary conditions for solid problems is necessary.

Figure 6.14: Test case-3; 1)Geometry and boundary conditions; 2)Temperature profile; 3)Displacement along line BA(one-solver approach); 4)Displacement along line BA (2-solver approach)

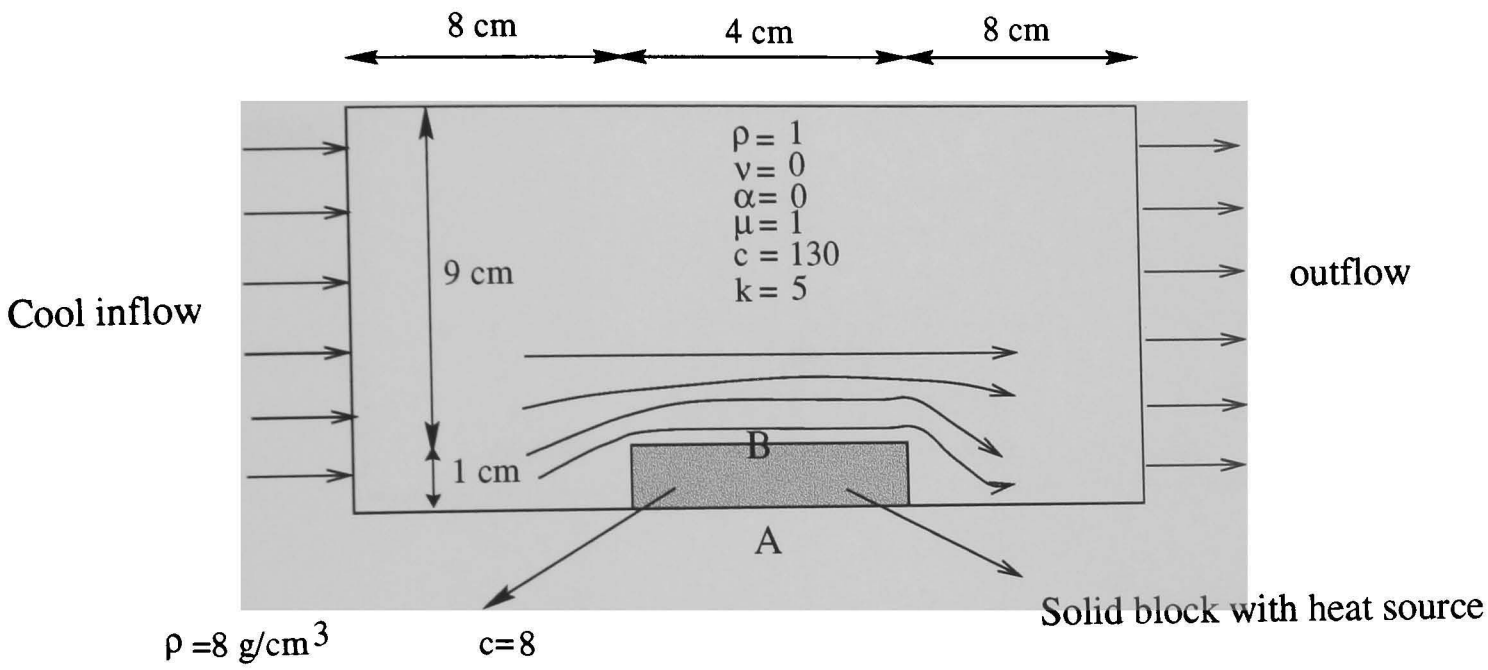

Figure 6.15: Heated solid block with cooling fluid

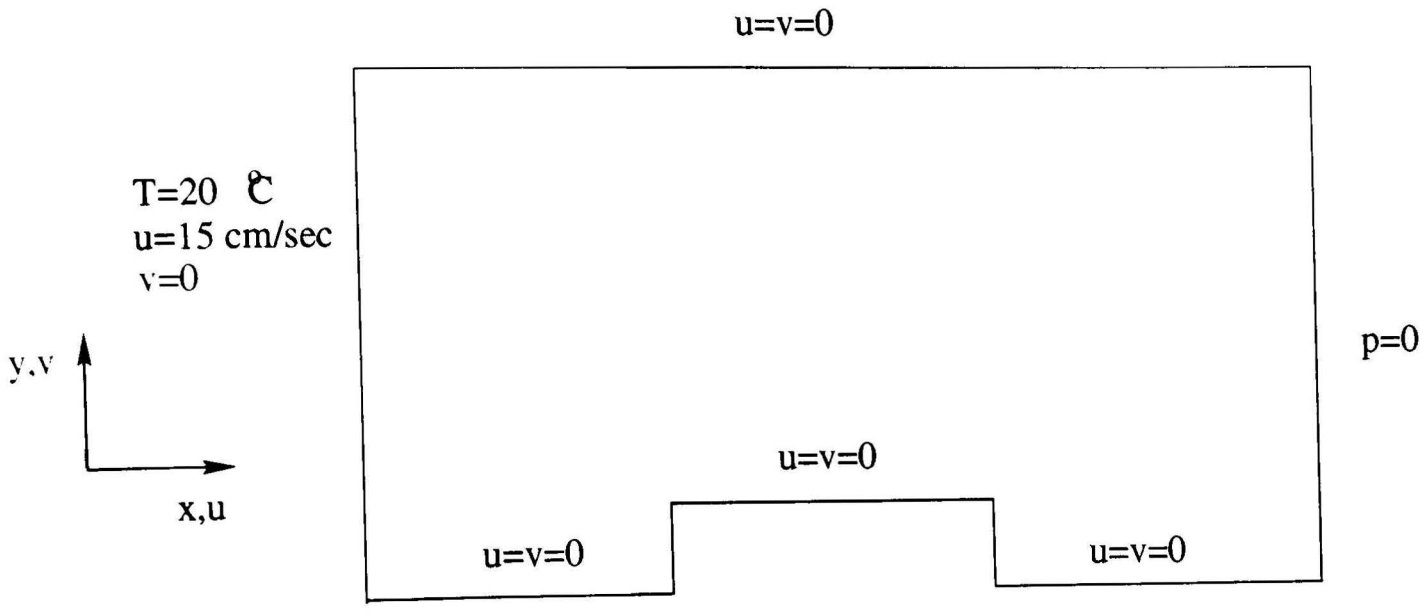

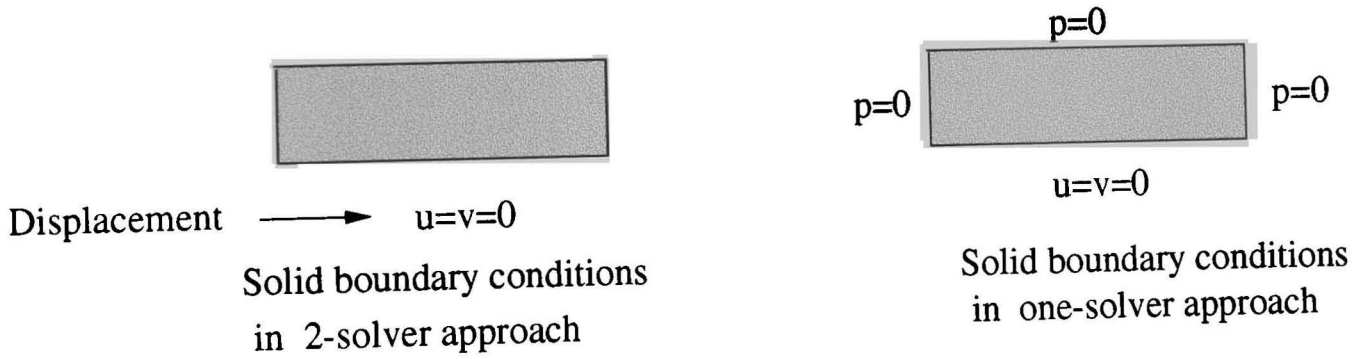

Figure 6.16: Boundary conditions for the fluid and solid regions

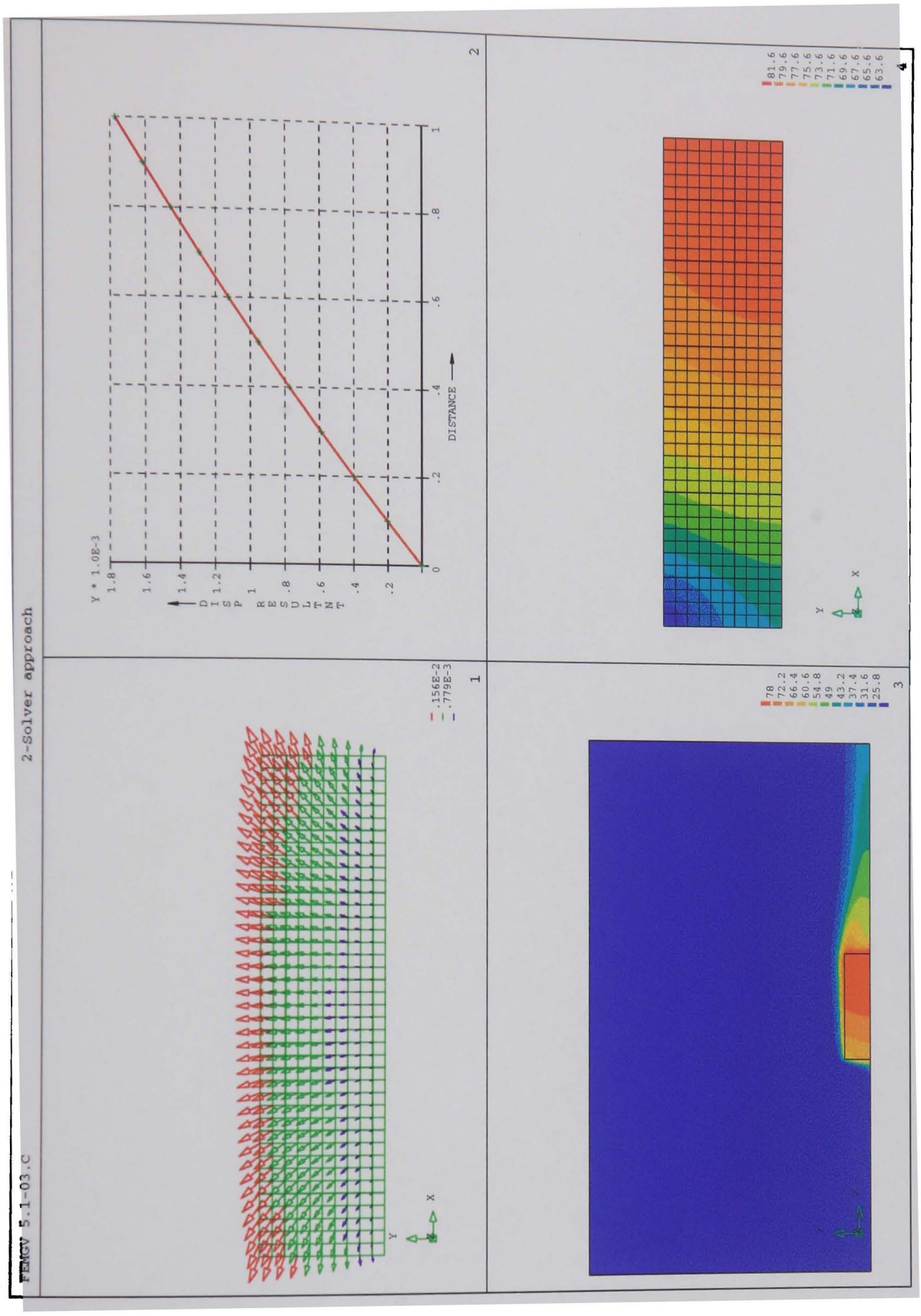

Figure 6.17: Heated solid block with cooling flow, 2-solver approach. (1)solid resultant displacement field, (2)solid resultant displacement along central line AB, (3)temperature field, (4)temperature in solid region

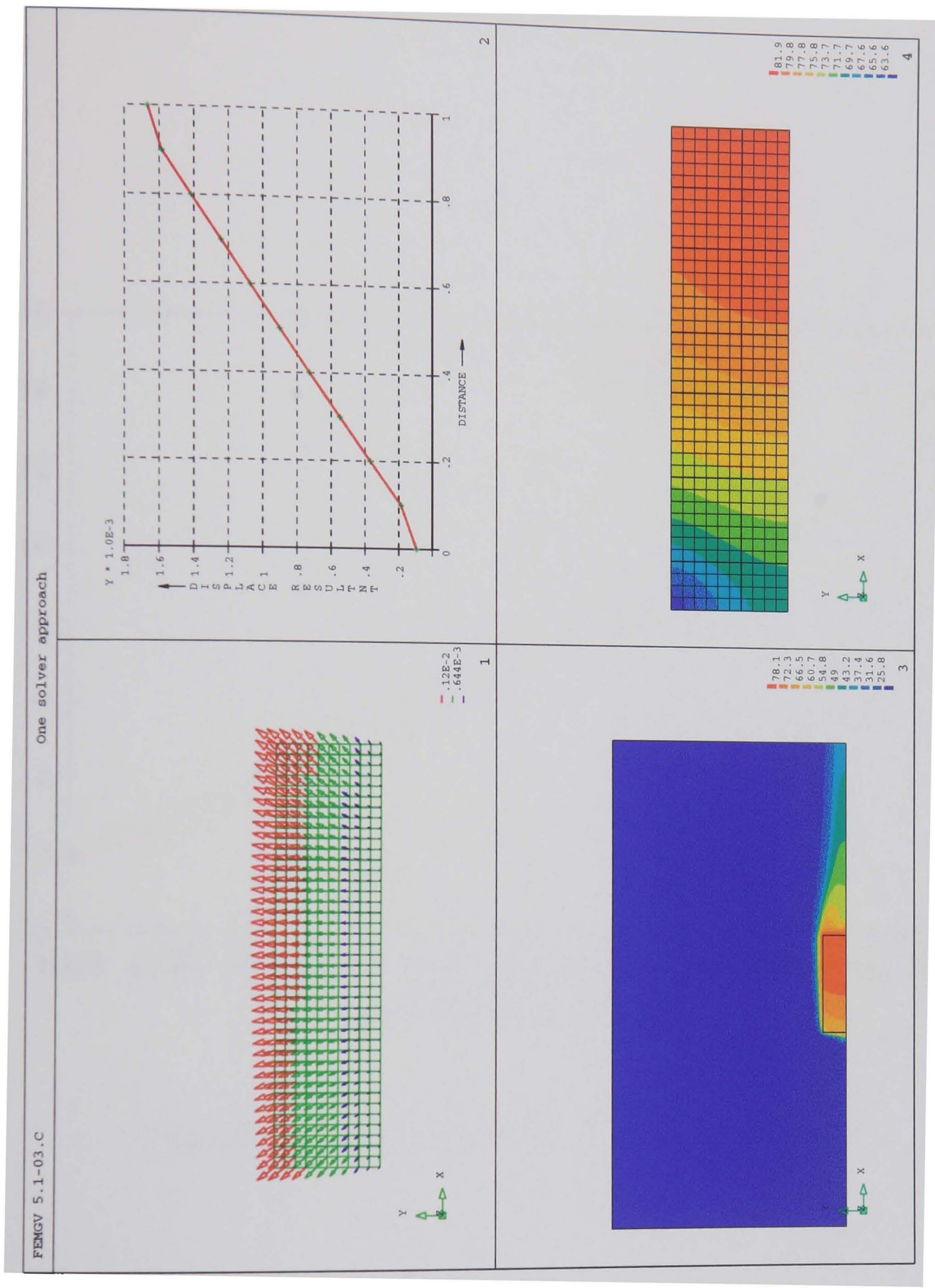

Figure 6.18: Heated solid block with cooling flow, one solver approach. (1)solid resultant displacement field, (2)solid resultant displacement along central line AB, (3)temperature field, (4)temperature in solid region

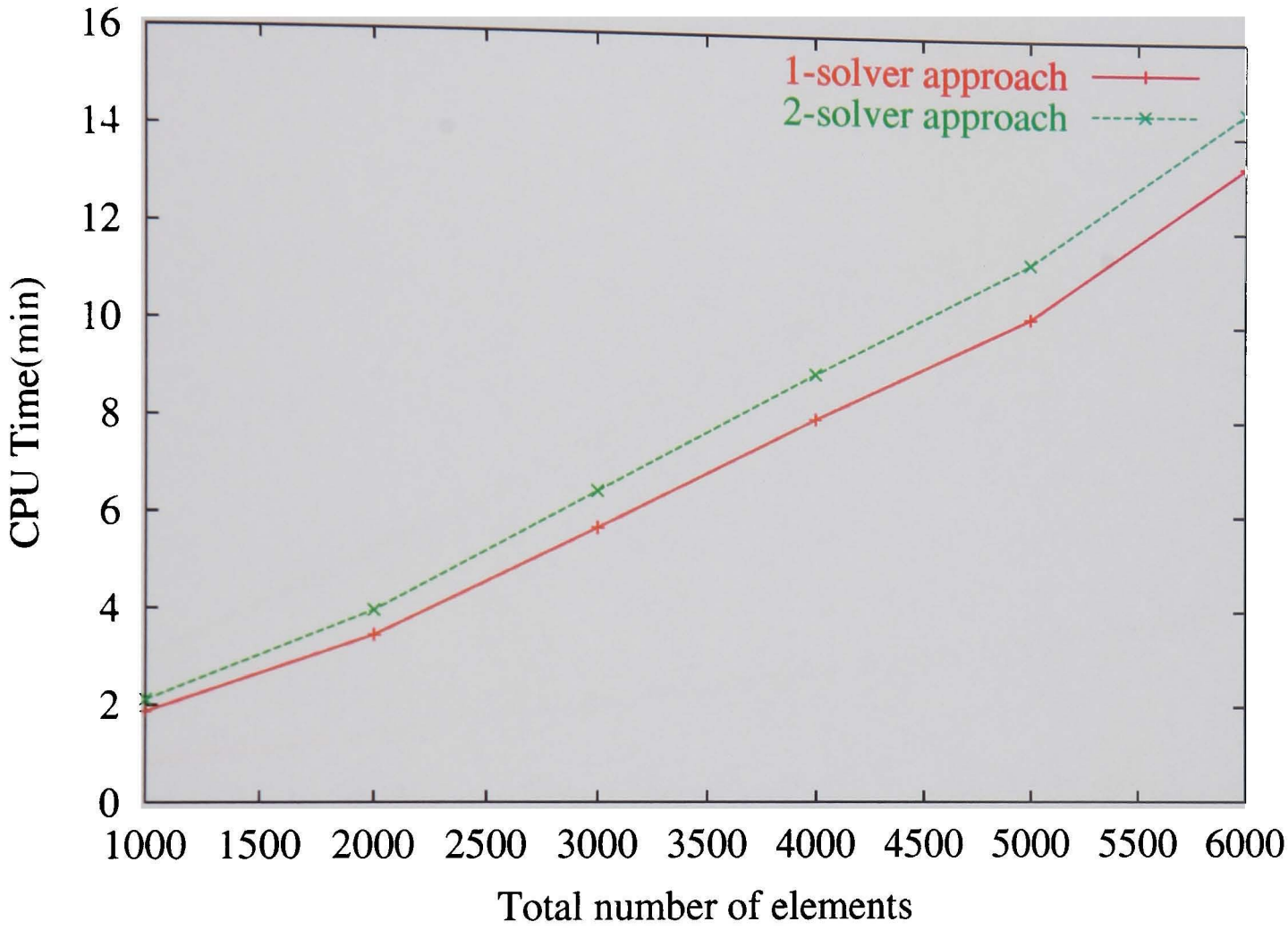

Figure 6.19: Total CPU time spent in different approaches

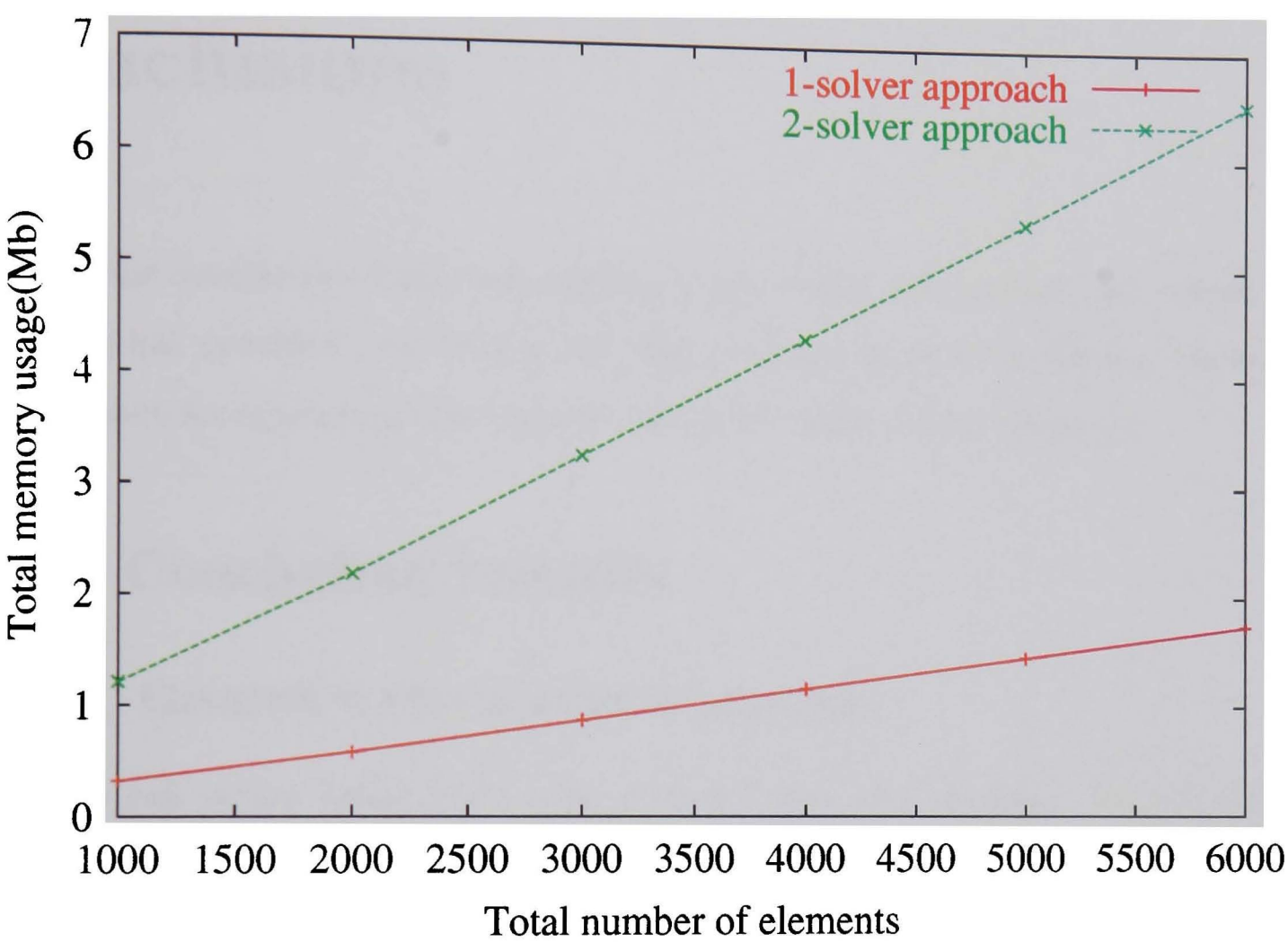

Figure 6.20: Total memory usage in different approaches

Chapter 7

Conclusions

Firstly the conclusions from each chapter of this thesis will be discussed, where the research has provided new data to the field of computational mechanics. Secondly the options for extending this research as further work will be discussed.

7.1 Concluding remarks

7.1.1 Geometrically nonlinear analysis

A novel cell vertex based finite volume formulation was developed for the elastic geometrically nonlinear problems and was compared with the Bubnov-Galerkin finite element formulation(FE). The numerical results, presented in chapter 4, have shown the capability of the cell-vertex based finite volume(CV-FV) approach for the geometrically nonlinear(GNL) analysis. Results show that the FE approach results in a symmetric stiffness matrix while the CV-FV procedure provides a stiffness matrix that is potentially asymmetric. The discretization based on the constant strain triangular(CST) element results in a symmetric stiffness matrix, but the bilinear quadrilateral(BLQ) element results in asymmetric stiffness matrix. For the CST element both FE and CV-FV result in the same stiffness matrix and this equivalence has been proven theoretically and numerically in chapter 4. This observation

has been already reported for the linear elements for problems involving material nonlinearity in small deformation analysis[57].

While the BLQ elements provide more accurate results in GNL analysis the CST elements are not able to do. For BLQ elements with general form, the CV-FV requires solvers like Bi-Conjugate Gradient(BiCG) for the assembled nonsymmetric equations, where the assembled symmetric equations by the FEM can take advantage of standard solvers like the Conjugate Gradient(CG) method. For the GNL analysis, Jacobi pre-conditioning is applied for the both solvers and the computational expense of the BiCG solver is higher than the CG solver. It should be noted that a number of pre-conditionings could be applied that may reduce the computational cost, such as incomplete Cholesky.

7.1.2 Plate analysis

The CV-FV method was also developed for plate bending analysis based on the Reissner/Mindlin plate theory. Although the main goal of this research was the development of a finite volume formulation for the stress analysis, in parallel, a finite element code was also developed which provided a comparisons for the finite volume assessments. The results of chapter 5 show that the cell vertex based finite volume method has interesting features in representing the behaviour of thick and thin plates. The FE approach with BLQ elements suffers from locking problem for moderate thick and thin plates. The CV-FV has the capability to avoid locking for thin plate analysis.

7.1.3 CFD framework for the solid mechanics analysis

Analysis of problems involving the simultaneous effects of fluid flow, temperature and solid stress (multiphysics), requires the use of two distinct software packages or, two different solvers in one software package. Another goal of this research project

was the development of a technique in the PHYSICA user environment which performs both tasks at the same time by using a flow solver to predict solid displacement without making major changes inside the PHYSICA package. The work relies on the existence of similarities of the equations, governing velocity field in fluids to those governing displacements in solids. The flow module in the PHYSICA code is based on the cell centred finite volume discretization technique, so this work in addition to providing multiphysics analysis also provides a potential cell centred finite volume(CC-FV) based technique for solid mechanics problems. Another interesting aspect of this work is that, it has the potential capability for the incompressible material analysis. This is due to taking out the hydro-static pressure term from the stress tensor. The results of this work is very promising and future work can reveal more advantages of this approach. Test cases presented in chapter 6 show that, this approach can save not only memory usage but also CPU time.

7.2 Future research

This section details further work that can be undertaken to extend the capabilities of the research already presented.

7.2.1 Material nonlinearity

The work presented for GNL analysis is currently limited to linear elastic material. Linking this work to previous research for small strain visco-plastic material analysis[57], will combine material and large strain nonlinearities, which results in a CV-FV package for analysis of industrial processes like forging. When deformation gets larger and larger the deformed body should be remeshed for predicting accurate results. So remeshing could be another part of the future developments.

7.2.2 Shell structure analysis

The CV-FV based plate formulation can be developed for the shell structure analysis. Although the current work has the capability for thick and thin plate analysis, it would be useful to consider the in-plain(membrane) action and hence the capability can be enhanced for shell analysis.

7.2.3 Cell centred finite volume framework for the solid mechanics problems

We can conclude that the cell vertex based finite volume method take longer to converge and may require more memory compared to the finite element method. The results in chapter 6 show that the cell centred finite volume has the advantages of a segregated approach and considering less degrees of freedom which can save both memory usage and CPU time. Experience with PHYSICA shows that, it is possible to use the flow module for stress analysis based on the CC-FV technique. The work can be advanced in the following way:

- For the small strain compressible solid problems the solid momentum equations can be introduced to the PHYSICA in the flow module as a pure diffusion case. Also further developments are:
  - Adding new sort of boundary conditions for proper handling of the solid boundary.
  - Proper time integration techniques for transient analysis, where for solid, we need to discretize the second time derivatives of the displacement vector.
  - Introducing extra terms of solid momentum equations to the PHYSICA by using the user environment.
- For small strain incompressible solid problems, the pressure displacement formulation (also known as the mixed formulation) of momentum equations can

be used.

It is notable, the current capability of flow module for compressible and incompressible solid problems analysis is limited to problems with boundary conditions which are similar to the fluid boundary conditions.

7.2.4 Multiphysics analysis

At the current stage, the one solver approach is limited to the steady state situation, further work can be done for including the contributions of transient terms of solid momentum equations in solution procedures. The solid material is assumed as elastic material. further work can be performed to consider the non-linear material behaviours. Including the solid type boundary conditions in Flow module of PHYSICA can improve the capability of one solver approach for more accurate analysis of multiphysics problems.

Bibliography

[1] R. T. Fenner. *Engineering Elasticity: Application of Numerical and Analytical Techniques.* Ellis Horwood Ltd., Chichester, UK, 1986.

[2] Y. D. Fryer. A control volume unstructured grid approach to the solution of the elastic stress-strain equations. PhD thesis, The University of Greenwich,1993.

[3] S. V. Patankar. *Numerical Heat Transfer and Fluid Flow.* Hemispher, Washington DC. 1989.

[4] C. Hirsch. *Numerical Computation of Internal and External Flow*, volume 1. John Wiley & Sons,New York, 1989.

[5] I. Demirdzic, D. Martinovic, and A. Ivankovic. Numerical simulation of thermo-mechanical deformation processes in a welded work-piece. *Zavarivanje*, 31:209–219, 1988. (in Croatian).

[6] I. Demirdzic and D. Martinovic. Finite volume method for thermo-elasto-plastic stress analysis. *Computer methods in applied mechanics and engineering*, 109:331–349, 1993.

[7] I. Demirdzic and S. Muzaferija. Finite volume method for stress analysis in complex domains. *Int. J. Numer. Methods Eng.*, 37:3751–3766, 1994.

[8] A. Ivankovic, I. Demirdzic, J. G. Williams, and P. S. Leevers. Application of finite volume method to the analysis of dynamic fracture problems. *Int. J. Fracture*, 66(4):357–371, 1994.

[9] K. J. Bathe and M. Ozdemir. Eelastic-plastic large deformation static and dynamic analysis. *Compt. Struct.*, 6(2):81–92, Apr. 1976.

[10] J. T. Oden and T. Sato. ,'Finite strains and displacements of elastic membranes by the finite element method'. *Int. J. Solids Structures*, 3:471–488, 1967.

[11] J. T. Oden. .'Finite plain strain of incompressible elastic solids by the finite element method'. *The aeronautical quarterly*, pages 254–264, 1968.

[12] K. Maneeratana and A. Ivankovic. Finite volume method for geometrically non-linear stress analysis application. *Proc. ACME'99,The Seventh Annual Conference of the Association for Computational Mechanics in Engineering,Durham,UK*, pages 117–120, 1999.

[13] P. Wenke and M. A. Wheel. Large deformation finite volume method for hyperelastic materials. *Proc. ACME'99,The Seventh Annual Conference of the Association for Computational Mechanics in Engineering,Durham,UK*, pages 113–116. 1999.

[14] N. A. Fallah, C. Bailey, and M. Cross. Finite volume method for stress analysis. *Proc. ACME'99,The seventh annual conference of the association for computational mechanics in engineering,Durham,UK*, pages 135–138, 1999.

[15] N. A. Fallah, C. Bailey, M. Cross, and G. A. Taylor. Comparison of finite element and finite volume methods application in geometrically nonlinear stress analysis. *Applied Mathematical Modelling*, 24:439–455, 2000.

[16] O. C. Zienkiewicz and R. L. Taylor. *The Finite Element Method*, volume 2. McGraw-Hill, UK, 4th edition, 1991.

[17] E. Reissner. The effect of transverse shear deformation on the bending of elastic plates. *J. Appl. Mech.*, 12:69–76, 1945.

[18] R. D. Mindlin. Influence of rotatory inertia and shear in flexural motions of isotropic elastic plates. *J. Appl. Mech.*, 18:31–38, 1951.

[19] R. H. Gallagher. Analysis of plate and shell structures. *Proceedings, Symposium on the application of finite element methods in civil engineering, Vanderbilt University. Nashville , TN*, pages 155–205, 1969.

[20] O. C. Zienkiewicz and Y. K. Cheung. The finite element method for analysis of elastic isotropic and orthotropic slabs. *Proc. Inst. Civ. Eng.*, 28:471–488, 1964.

[21] G. Dhatt and S. Venkatasubbu. Finite element analysis of containment vessels. *Proc. First. Int. Conf. on Struct. Mech. in Reactor Tech., Berlin, Germany,*, 5, Sept. 1971. PAPER J. 3/6.

[22] R. D. Wood. A shape function routine for the constant moment triangular plate bending element. *Eng. Computations*, 1:189–198, 1984.

[23] K. J. Bathe and E. N. Dvorkin. Short communication, a four-node plate bending element based on mindlin/reissner plate theory and a mixed interpolation. *Int. J. Numer. Methods Engrg*, 21:367–383, 1985.

[24] Z. Xu. A simple and efficient triangular finite element for plate bending. *Acta Mechanica Sinica*, 2:185–192, 1986.

[25] O. C. Zienkiewicz and D. Lefebvre. A rubost triangular plate bending elementof the reissner-mindlin type. *Int. J. Num. Meth. Eng.*, 26:1169–1184, 1988.

[26] J. L. Batoz and P. Lardeur. A discrete shear triangular nine d.o.f. element for the analysis of thick to very thin plates. *Int. J. Num. Meth. Eng.*, 28:533–560, 1989.

[27] I. Demirdzic, S. Muzaferija, and M. Peric. Benchmark solutions of some structural analysis problems using finite-volume method and multigrid acceleration. *Int. J. Numer. Methods Eng.*, 40:1893–1908, 1997.

[28] M. A. Wheel. A finite volume method for analysing the bending deformation of thick and thin plates. *Computer methods in applied mechanics and engineering*, 147:199–208, 1997.

[29] O. C. Zienkiewicz. Coupled problems and their numerical solution. In R. W. Lewis, P. Bettess, and E. Hinton, editors, *Numerical Methods in Coupled Systems*, pages 35–68. Wiley, Chichester, 1984.

[30] A. K. Slone, K. Pericleous, C. Bailey, and M. Cross. Dynamic fluid-structure interactions using finite volume unstructured mesh procedures. *International forum on aeroelasticity and structural dynamics*, Rome, Italy, June 1997.

[31] I. Demirdzic and S. Muzaferija. Numerical method for coupled fluid flow, heat transfer and stress analysis using unstructured moving meshes with cells of arbitrary topology. *Computer methods in applied mechanics and engineering*, 125:235–255, 1995.

[32] D. B. Spalding. Simultaneous fluid-flow, heat-transfer and solid-stress computation in a single computer code. In *4th international colloquium on process simulation, Helsinki University of Technology*, pages 5–21. 1997.

[33] University of Greenwich, Greenwich, London, SE10 9LS, PHYSICA-A software environment for the modelling of multi-physics phenomena, http://www.physica.co.uk.

[34] L. E. Malvern. *Introduction to the Mechanics of a Continuous Medium.* Prentice-Hall, 1969.

[35] S. S. Rao. *The finite element method in engineering.* Robert Maxwell, M. C., 1982.

[36] G. E. Mase. *Theory and problems of continuum Mechanics. Shaum's outline series in engineering.* McGraw-Hill, 1970.

[37] NAFEMS. *Introduction to nonlinear finite element analysis.* 1992. editor: E. Hinton.

[38] C. A. J. Fletcher. *Computational techniques for fluid dynamics: foundamental and general techniques*, volume 1. Springer-verlag, Berlin, 1978.

[39] T. N. Croft. Unstructured mesh-finite volume algorithms for swirling turbulent reacting flows. PhD thesis, The University of Greenwich,1998.

[40] C. M. Rhie and W. L. Chow. Numerical study of the turbulent flow past an airfoil with trailing edge separation. *AIAA Journal*, 21(11):1525–1532, 1983.

[41] I. Demirdzic, S. Muzaferija, and M. Peric. Advances in computation of heat transfer. fluid flow and solid body deformation using finite volume approaches. In W. J. Minkowycz and E. M. Sparrow, editors, *Advances in Numerical Heat Transfer*. volume 1, chapter 2, pages 59–96. Taylor & Francis, 1997.

[42] A. Ivankovic, S. Muzaferija, and I. Demirdzic. Finite volume method and multigrid acceleration in modelling of rapid crack propagation in full-scale pipe test. *Computational mechanics-International journal then research journal*, 20(1/2):p.46, 1997.

[43] A. Ivankovic. Finite volume analysis of dynamic fracture problems. In S. N. Atluri and P. E. O' Donoghue, editors, *Modelling and Simulation Based Engineering*, volume 1. pages 180–187. Tech Science Press, 1998.

[44] A. Ivankovic and G. P. Venizelos. Rapid crack propagation in plastic pipe: predicting full-scale critical pressure from s4 test results. *Engineering fracture mechanics*, 59(15):p.607, 1998.

[45] M. A. Wheel. A geometrically versatile finite volume formulation for plane elastostatic stress analysis. *J. of Strain Analysis*, 31(2, 1996.

[46] M. A. Wheel. Applying the finite volume approach to structural analysis. In S. N. Atluri and P. E. O' Donoghue, editors, *Modelling and Simulation Based Engineering*, volume 1, pages 229–234. Tech Science Press, 1998.

[47] M. A. Wheel. A mixed finite volume formulation for determining the small strain deformation of incompressible materials. *Int. J. Numer. Methods Eng.*, 44, 1999.

[48] E. Onate, M. Cervera, and O. C. Zienkiewicz. A finite volume format for structural mechanics. *Int. J. Numer. Methods Eng.*, 37:181–201, 1994.

[49] V. Selmin and L. Formaggia. Unified construction of finite element and finite volume discretisations for compressible flows. *Int. J. Numer. Methods Eng.*, 39:1–32. 1996.

[50] A. M. Winslow. Numerical simulation of the quasilinear poisson equation in a nonuniform triangle mesh. *Journal of computational physics*, 29:149–171, 1966.

[51] B. R. Baliga and S. V. Patankar. A new finite element formulation for convection-diffusion problems. *Numerical Heat Transfer*, 3:393–409, 1980.

[52] A. Jameson, T. J. Baker, and N. P. Weatherill. Calculation of inviscid transonic flow over a complete aircraft. *AIAA, Paper AIAA-86-0103*, 1986.

[53] P. Chow and M. Cross. An enthalpy control volume unstructured mesh(cv-um) algorithm for solidification by conduction only. *Int. J. Numer. Methods Eng.*, 35(9):1849–1870, 1992.

[54] Y. D. Fryer, C. Bailey, M. Cross, and C. H. Lai. A'control volume procedure for solving the elastic stress -strain equations on an unstructured mesh. *Appl. Math. Modelling*, 15:639–645, 1991.

[55] C. Bailey and M. Cross. A finite volume procedure to solve elastic solid mechanics problems in three dimensions on an unstructured mesh. *Int. J. numer. methods in eng.*, 38:1757–1776, 1995.

[56] K. J. Bathe. *Finite element procedures.* Prentice-Hall, 1996.

[57] G. A. Taylor. A vertex based discretisation scheme applied to material nonlinearity within a multi-physics finite volume framework. PhD thesis, The University of Greenwich,1996.

[58] V. Selim. A node centred finite volume approach: bridge between finite differences and finite elements. *Comput. Methods Appl. Mech. Eng.*, 102:107–138, 1993.

[59] B. A. Finlayson. *The method of weighted residuals and variational principles.* Academic press, New York, 1972.

[60] M. A. Crisfield. *Non-linear Finite Element Analysis of Solids and Structures,* volume 1. John Wiley & Sons, UK, 1994.

[61] R. D. Wood and O. C. Zienkiewicz. Geometrically nonlinear finite element analysis of beams, frames arches and axisymmetric shells. *Int. J. Numer. Methods Eng.*, 7:725–735, 1977.

[62] E. Kreyszig. *Advanced engineering mathematics.* John Wiley,New York, 5th edition, 1983.

[63] J. M. Gere and S. Timoshenko. *Mechanics of materials.* Chapman & Hall, third SI Edition.

[64] G. Adotte. Second order theory in orthotropic plates. *Proceedings, Journal of the Structural Division, ASCE*, 93(ST5,Proc. Paper 5520), Oct 1967.

[65] *ANSYS Release 5.3.*

[66] G. A. Taylor, C. Bailey, and M. Cross. ,'Solution of the elastic/visco-plastic constitutive equations a finite volume approach'. *Appl. Math. Modelling*, 19:743–760, 1995.

[67] E. Hinton and D. R. J. Owen. *Finite element software for plate and shells.* Pineridge Press Limited, 1984.

[68] S. P. Timoshenko and S. Woinowsky-Krieger. *Theory of plates and shells.* McGraw Hill, Singapore,1970.

[69] O. C. Zienkiewicz, R. L. Taylor, and J. M. Too. Reduced integration in general analysis of plates and shells. *Int. J. numer. methods in eng.*, 3:275–290, 1971.

[70] T. J. R. Hughes, M. Cohen, and M. Haroun. Reduced and selective integration techniques in the finite element analysis of plates. *Nuclear engineering and design*, 46:203–222, 1978.

[71] V. L. Salerno and M. A.Goldberg. Effect of shear deformations on the bending of rectangular plates. *J. Appl. Mech.*, 27:54–58, 1960.

[72] N. A. Fallah, C. Bailey, and M. Cross. CFD approach for solid mechanics analysis. *European congress on computational methods in applied sciences and engineering, ECCOMAS*, Barcelona, Sept. 2000.

[73] H. K. Versteeg and W. Malalasekera. *An introduction to computational fluid dynamics, the finite volume method.* Longman Scientific & technical,1995.

[74] H. Schlichting. *Boundary-layer theory.* 7th ed, McGraw Hill, New York,1979.

[75] FEMVIEW Limited, 1 St. Albans Road, Leicester LE2 1GF, England, FEMGEN/FEMVIEW, 1991.

[76] Macneal-Schwendler Corporation, Los Angeles, USA, PATRAN, 5.0 edition, March 1996.

[77] F. H. Harlow and J. E. Welch. Numerical calculation of time-dependent viscous incompressible flow of fluid with free surface. *The Physics of Fluids*, 8(12):2182–2189, 1965.

[78] S. V. Patankar and D. B. Spalding. A calculation procedure for heat, mass and momentum transfer in three dimensional parabolic flows. *Int. j. of heat and mass transfer*, 15:1787–1806, 1972.

[79] L. S. Caretto, R. M. Curr, and D. B. Spalding. Two numerical methods for three dimensional boundary layers. *Comput. Methods Appl. Mech. Eng.*, 1:39–59. 1972.